Photochemical Reactivity of Dissolved Organic Matter: Implications for the Environmental Fate and Engineered Removal of Saxitoxins

Kari Elena Norris
B.S. Chemistry, Bethel University, 2020

A thesis submitted to the Faculty of the Graduate School of the University of Colorado in partial fulfillment of the requirements for the degree of Doctor of Philosophy Department of Civil, Environmental, and Architectural Engineering
2025

Committee Members:
Fernando Rosario-Ortiz—Chair
Diane McKnight
Karl Linden
Teng Zeng
Elisabeth Janssen

ABSTRACT

Norris, Kari (PhD, Environmental Engineering)

Photochemical Reactivity of Dissolved Organic Matter: Implications in the Environmental Fate and Engineered Removal of Saxitoxins

Thesis directed by Professor Fernando Rosario-Ortiz

Dissolved organic matter (DOM) is a fundamental component of natural aquatic systems that influences processes such as nutrient cycling, primary productivity through the attenuation of light, indirect photochemical transformations of contaminants, and production of CO_2 through photomineralization. DOM also has a major impact on engineered water treatment systems due to its reactivity with oxidants, such as chlorine and ozone, and absorption of ultraviolet (UV) light. Despite many years of efforts to characterize DOM, its complexity and variation across aquatic systems have imposed challenges to analyzing DOM composition, chemical structure, and reactivity. Two areas of DOM research that have remained unclear are its three-dimensional (3D) structure and its photochemical production of reactive intermediates (RIs). First, the 3D structure of DOM is important to understanding intermolecular interactions within DOM, the reactivity of DOM in engineered systems, and the interactions between DOM molecules and contaminants. Second, the photochemical production of RIs from DOM is well-understood, apart from hydroxyl radicals ($^{\bullet}OH$). Due to the fast reaction rates and non-selective reactivity of $^{\bullet}OH$, it is important to understand which chemical components of DOM contribute to $^{\bullet}OH$ generation and how quickly $^{\bullet}OH$ is formed.

The RIs produced by DOM play a crucial role in the environmental fate of molecules such as saxitoxins, which do not absorb light in the solar spectrum and are resistant to microbial

degradation and hydrolysis. Saxitoxins are a class of neurotoxins produced by cyanobacteria during a harmful algal bloom (HAB). The release of saxitoxins by cyanobacteria is a concern for the health of aquatic ecosystems, may cause human intoxication through recreation in affected water bodies, and threaten drinking water quality. Since saxitoxins are resistant to degradation through several conventional water treatment methods, it is critical to develop an efficient removal option in the case that saxitoxins are present at dangerous levels in source waters.

This thesis aims to address DOM structure and mechanisms of $^{\bullet}OH$ production in order to elucidate its critical role in the photochemical degradation of emerging contaminants such as saxitoxins. Chapter 2 explores previous literature related to the 3D structure of DOM and proposes a new model to depict the simultaneous solubility of DOM molecules and their complex intermolecular interactions. In Chapter 3, the mechanism of the photochemical generation of $^{\bullet}OH$ by DOM model photosensitizers is examined. Chapters 4 and 5 evaluate the indirect photochemical degradation of saxitoxins in natural surface waters and UV-advanced oxidation processes (AOP), respectively.

ACKNOWLEDGMENTS

Completing my doctorate is an achievement that I am honored to share with the people who have supported and guided me along the way. First, I want to thank my advisor, Fernando Rosario-Ortiz, for seeing my potential and trusting me to carry out research in his lab. Coming from a small undergraduate institution with no background in environmental engineering, I felt extremely out of place entering graduate school at the University of Colorado, but Fernando has always treated me as if I have been working in the field for decades. Fernando has challenged me to grow by working through puzzling projects, provided many opportunities to present my research at conferences, connected me with many great researchers in the field, and invested in all aspects of my future career. Next, I must acknowledge my undergraduate advisors, Dr. Rollin King and Dr. Mitchell Maddox III, for their mentorship and for encouraging me to pursue this degree. Also, I want to thank each of my dissertation committee members, Dr. Diane McKnight, Dr. Karl Linden, Dr. Teng Zeng, and Dr. Elisabeth Janssen, for their investment in my graduate work.

I extend my sincere gratitude to the many other faculty members and students at the University of Colorado who have encouraged me throughout these past four years. It has been a privilege to collaborate with and learn from the members of the Rosario-Ortiz group, including Frank Leresche, Shelby Buckley, Mackenzie Bowden, Tyler Kurtz, and Blair Hanson. Other past and present graduate students, including Emma Payne, William Johnson, Nayoung Hur, Annabel Mungan, Kylie Boenisch-Oakes, Emma Wilder, Nadia Jorgenson, and Ryan McKeown have brought joy and comradery to the lab and office spaces. The Environmental Engineering lab and instrument coordinators, Dorothy Noble, Stefan Peterson, and Jennifer Jankowiak, have been indispensable to my research progress. I would also like to acknowledge the contributions of my undergraduate mentees, Julia Dykstra and Alejandro Montgomery, and high school mentees, Alyx

McCaig and Claire Brown. It was a joy to practice teaching and mentoring with these four talented researchers as well as with the General Chemistry and Water Chemistry students for which I was a teaching assistant.

Finally, I am wholly grateful for my family and friends who have supported me practically, emotionally, and spiritually. My parents and sister have always encouraged me to pursue my aspirations, and they were instrumental in guiding my decision to go to graduate school, supporting my move to Colorado, and celebrating each milestone along the way. My community in Boulder, especially my friends from City Church and All Souls Church of Boulder, has been essential to my personal growth and brought me incredible joy during these past four years. And most of all, my husband, Isaac McCarty, has been my light and constant advocate amidst all the successes and challenges.

TABLE OF CONTENTS

LIST OF FIGURES

LIST OF SCHEMES

LIST OF TABLES

LIST OF TEXT SECTIONS

1. Introduction

1.1 Motivation

Dissolved organic matter (DOM) is a complex mixture of organic molecules derived from plant, animal, and microbial matter (Perdue & Ritchie, 2003). According to isotopic analyses, DOM is composed of 50-60% carbon (%(w/w)), 3-5% hydrogen, 30-40% oxygen, and <5% nitrogen (IHSS). It has been estimated that 63% of DOM organic carbon by weight, and 47% of total DOM weight, is attached to chromophores (Buckley et al., 2024). This portion of DOM is known as chromophoric DOM (CDOM). CDOM includes several classes of compounds including aromatic quinones and ketones, carboxylic acids, phenols, and alicyclic compounds (Buckley et al., 2024). Upon the absorption of a photon, CDOM forms an excited singlet state, $^{1}CDOM^{*}$, which undergoes intersystem crossing (ISC) to form a triplet excited state, $^{3}CDOM^{*}$, with an ISC quantum yield of 0.4-11% (Grebel et al., 2011, Schmidt et al., 2017, Buckley et al., 2024). The majority of $^{1}CDOM^{*}$ is deactivated through nonradiative pathways and is not typically considered to play a notable role in aquatic photochemistry due to its short lifetime (~100 ps) and low corresponding steady-state concentration of 10^{-17} to 10^{-14} M in sunlit surface waters (McNeill & Canonica, 2016). On the other hand, $^{3}CDOM^{*}$ has a lifetime of ~2 μs and is typically found in sunlit surface waters with steady-state concentrations between 10^{-14} and 10^{-12} M (Grebel et al., 2011, Sharpless et al., 2012; Schmidt et al. 2017, McNeill & Canonica, 2016).

$^{3}CDOM^{*}$ may directly react with contaminants via energy transfer (Liu et al., 1965), reduction and oxidation reactions (McNeill & Canonica, 2016), or through the formation of reactive intermediates (RIs) including singlet oxygen ($^{1}O_2$) and hydroxyl radicals ($^{\bullet}OH$) (Zafriou et al., 1984; Blough & Zepp, 1995; Vione et al., 2014) . The formation of $^{1}O_2$ is the dominant deactivation pathway of $^{3}CDOM^{*}$, occurring through the transfer of energy from $^{3}CDOM^{*}$ (triplet

energies of 180-320 kJ mol^{-1}; Zepp et al., 1985; McNeill & Canonica, 2016) to ground state oxygen, which only requires 94 kJ mol^{-1} to be promoted to $^1O_2$ (Wilkinson et al., 1993; Bodesheim et al., 1994; Schweitzer et al., 2003). $^1O_2$ can subsequently react with contaminants through selective electrophilic addition to unsaturated compounds via 1,2-ene or Diels-Alder mechanisms, single electron transfer reactions, or addition to heteroatoms (sulfur and nitrogen) (Boreen et al, 2008; DiMascio et al., 2019; Barrios et al., 2021). Accounting for a smaller portion of $^3CDOM^*$ deactivation is the formation of $^\bullet OH$, which occurs through the oxidation of ferrous iron in the presence of H_2O_2, known as the photo-Fenton reaction (Voelker et al., 1997; Nakatani et al., 2007), the production and photolysis of H_2O_2 (Cooper & Lean, 1989; Vaughan & Blough, 1998; Page et al., 2011), or a less-understood H_2O_2-independent mechanism (Page et al., 2011; Vione et al., 2006; Sun et al., 2015). $^\bullet OH$, despite typical steady-state concentrations in surface waters of only 10^{-17}-10^{-15} M (Mopper & Zhou, 1990; Vaughan & Blough, 1998; Vione et al., 2006), reacts non-selectively with both organic and inorganic species at near diffusion-controlled rates (Buxton et al., 1988).

Indirect photochemical reactions play a crucial role in the environmental fate of many contaminants and natural toxins, especially compounds that do not absorb sunlight and are resistant to microbial degradation and hydrolysis. Saxitoxins are one such class of compounds for which indirect photochemical reactions are important. Saxitoxins are a class of neurotoxic alkaloids produced by cyanobacteria and are becoming more of a concern to water quality due to the global increase in occurrence of harmful cyanobacterial blooms (CyanoHABs). CyanoHABs are described as the proliferated growth of cyanobacteria which leads to depleted dissolved oxygen and the production and release of cyanotoxins. CyanoHABs have been attributed to many factors that are expected to increase with climate change (Paerl & Paul, 2012), including the

eutrophication of surface waters, often through agricultural runoff or industrial discharge, warmer temperatures, longer stratification events, and elevated CO_2 levels (O'Neil et al, 2012; Paerl & Paul, 2012; Gehringer & Wannicke, 2014). Because of the anticipated propagation of CyanoHABs, it is critical that the environmental and engineered fates of cyanotoxins are well-understood. Humans may be exposed to cyanotoxins in freshwater or marine environments through recreation, consumption of shellfish, or drinking water (Chorus & Welker, 2021). Consequently, understanding the chemical structure and reactivity of persistent cyanotoxins, such as saxitoxins, will guide removal strategies from drinking water and address their threat to public health.

1.2 Research Objectives

This dissertation aims to elucidate the properties and reactivity of DOM as well as analyze the persistence of saxitoxins in both natural and engineered systems. First, a new structural model for DOM is proposed based on multiple sources of evidence with the goal of unifying past contradictory models. This unified framework for DOM structure will promote further research on DOM structure and how it impacts processes such as water treatment, sorption of organic compounds to DOM, and photochemical reactions. Next, this work intends to decipher pathways of hydroxyl radical production by DOM, which will contribute to understanding the fate of contaminants in natural aquatic systems and the mechanisms of DOM photomineralization. Finally, this thesis evaluates the rates and mechanisms of the photochemical degradation of saxitoxins in both natural surface waters and through UV- and Far-UVC-advanced oxidation processes. This work estimates the lifetime of saxitoxins in the environment and provides guidance for an emerging targeted removal method for saxitoxins from drinking water.

1.3 Thesis Organization

This thesis is comprised of four chapters representing four stand-alone publications, all of which contribute to the objectives outlined in Chapter 1.2.

Chapter 2, Recent Developments on the Three-Dimensional Structure of Dissolved Organic Matter: Towards a Unified Description, explores the 3D conformation of aquatic DOM by combining past models and solubility principles to lay a unified framework for DOM structure. This framework, introduced as the *mixed dynamic assembly model* (MDAM), represents the mutual existence of freely dissolved molecules with small intermolecular assemblies held together through a variety of interactions.

In Chapter 3, Examining the Mechanisms of Hydroxyl Radicals Generation by Dissolved Organic Matter, the mechanistic pathways of $^{\bullet}OH$ production by DOM are assessed using model quinones and hydroxybenzoic acids. This chapter shows that the pathway to the formation of free $^{\bullet}OH$ is possible from the transfer of electrons from triplet excited state quinones to phenolic compounds in DOM (H_2O_2-dependent). However, the dominant deactivation pathway for triplet quinones results in the formation of a lower-energy water-quinone exciplex, rather than $^{\bullet}OH$, under environmentally relevant concentrations. Hydroxybenzoic acids produce $^{\bullet}OH$ through a mechanism likely initiated by the generation of hydrated electrons (e_{aq}^{-}), with approximately 35% of $^{\bullet}OH$ formed through an H_2O_2-dependent pathway.

The indirect photochemical degradation of saxitoxins is evaluated in Chapter 4, titled Photochemical Degradation of Saxitoxins in Surface Waters. This chapter reveals that saxitoxins have a lifetime of ~1-10 hours in sunlit surface waters, attributed mostly to an electron transfer reaction with $^{3}DOM^{*}$. Three transformation products were identified during saxitoxin photolysis, elucidating the potential reaction for the electron transfer and subsequent degradation mechanism.

Chapter 5, Enhanced Degradation of Saxitoxins by Far-UVC Advanced Oxidation Processes, demonstrates that UV irradiation combined with hydrogen peroxide (UV/H_2O_2) leads to the reduction of saxitoxin concentrations by 27-74% in ultrapure water, with significant inhibition in the presence of DOM. It was also shown that saxitoxin degradation occurred 2.1-5.9 times faster in a $KrCl^*$ excimer system (emitting light at 222 nm) compared to a low-pressure UV system (emitting light at 254 nm) due to the efficient generation of $^{\bullet}OH$ at 222 nm. These results promote UV/H_2O_2, specifically Far-UVC/ H_2O_2 as a promising targeted removal option for saxitoxins in drinking water, though further optimization would be necessary for waters with high TOC or other background matrices with high absorbance and $^{\bullet}OH$ scavenging.

2. Recent Developments on the Three-Dimensional Structure of Dissolved Organic Matter: Towards a Unified Description

This chapter has been published as: **Norris, K. E.**; Pignatello, J. J.; Vialykh, E. A.; Sander, M.; McNeill, K.; Rosario-Ortiz, F. L. Recent Developments on the Three-Dimensional Structure of Dissolved Organic Matter: Toward a Unified Description. *Environ. Sci. Technol.* **2025**. https://doi.org/10.1021/acs.est.4c09627.

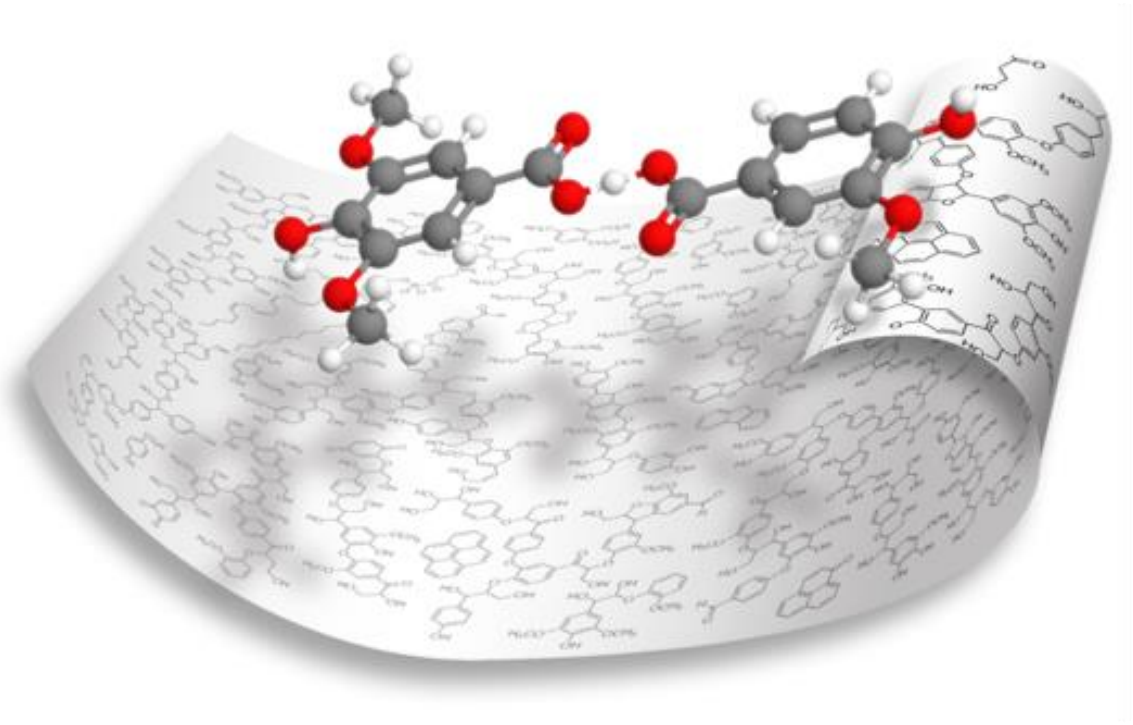

Figure 2.1 Graphical abstract for Recent Developments on the Three-Dimensional Structure of Dissolved Organic Matter: Toward a Unified Description.

2.1 Abstract

Advancing a common understanding about the chemical composition, size, and three-dimensional (3D) structure of dissolved organic matter (DOM) is paramount to deciphering its impact on and involvement in environmental processes such as the fate and transport of contaminants and carbon cycling. Traditionally, DOM has been described as a collection of solvent-separated molecules or macromolecules. More recently, DOM has been depicted as a "supramolecular assembly", a collection of individual molecules and associations of molecules

held together by noncovalent interactions. The supramolecular assembly model has been broadly invoked to rationalize certain behaviors and properties of DOM, yet the complexity of DOM has made it difficult to fully unravel the nature and contributions of its intermolecular interactions. Discussed in this perspective is evidence regarding thermodynamic drivers of intermolecular associations, DOM molecular size, sorption of organic contaminants to DOM, and optical properties of DOM. While single observations may be rationalized by former structural models, such as the supramolecular assembly model, combined evidence shows that the 3D structure of DOM is best described by a *mixed dynamic assembly model (MDAM)*. The MDAM depicts DOM as a collection of solvent-separated molecules and small, tightly knit assemblies (<10 kDa) held together by strong hydrogen bonds, which may form large assemblies (>10 kDa) through weak intermolecular interactions *only* at specific pH values, high ionic strength, or high DOM concentration.

2.2 Synopsis

Combined experimental evidence shows that the three-dimensional structure of DOM is best described by a mixed dynamic assembly model (MDAM), consisting of both solvent-separated molecules and supramolecular assemblies.

2.3 Introduction

Ever since dissolved organic matter (DOM) in surface waters—initially termed 'humic substances'—was first described in the 1800s (Stevenson, 1994), scientists have been fascinated with its composition and three-dimensional (3D) structure. Characterization of DOM structure has led to a better understanding and prediction of its impact on both natural and engineered processes, including the global carbon cycle, contaminant fate and transport, membrane fouling, and the formation of disinfection byproducts (Thurman, 1985; Perdue & Ritchie, 2003). The literature is

replete with attempts to create 3D models that rationalize observed behaviors of DOM, beginning with the "macromolecular" (sometimes called "polymer") paradigm, in which single, solvent-separated large molecules form linear or folded structures depending on solution chemistry (Stevenson, 1994). Added later was the micellar concept which posed segregation of relatively hydrophilic and relatively hydrophobic segments to the aqueous interfacial and interior regions of DOM, respectively (Wershaw, 1993; Engebretson & von Wandruszka, 1994; Piccolo et al., 1996). The concept of a supramolecular assembly was first introduced by Piccolo (2001) to explain aggregational phenomena observed through size-exclusion chromatography (SEC), and has since been broadly applied to rationalize observations regarding DOM molecular size, particle size, sorption processes, and optical properties. The supramolecular concept is derived from the field of supramolecular chemistry, which defines a supramolecular assembly as *a noncovalent association between two or more molecular species that exhibits properties as well defined as an individual molecule* (Lehn, 1988). Recently, a two-tiered supramolecular architecture[9] has been proposed by which strong hydrogen bonds between molecules form smaller, stable primary aggregates ("metachemical hydrogels" or "tightly-knit particles") and weak interactions between primary aggregates or individual molecules make up larger aggregates ("physical hydrogels" or "loosely-knit aggregates") (Wells & Stretz, 2019; Baigorri et al., 2007; Wang et al., 2024). Considering multiple lines of evidence regarding DOM structure, however, a complete and accurate description of DOM requires a combination of previous models. We propose a unified description of DOM as a collection of solvent-separated molecules and supramolecular assemblies, termed a *mixed dynamic assembly model (MDAM)*. This model can be visualized by computational models of DOM-like molecules, such as in Figure 2.2, which shows molecular dynamics (MD) simulations of model humic and fulvic acids in water or in a vacuum. Figure 2.2 (b) and (d) depict how, in

aqueous solution, DOM exists as both solvent-separated molecules and supramolecular assemblies. Figure 2.2 (a) and (c) highlight the tendency for DOM molecules to interact at extremely high concentration, forming more and larger supramolecules assemblies.

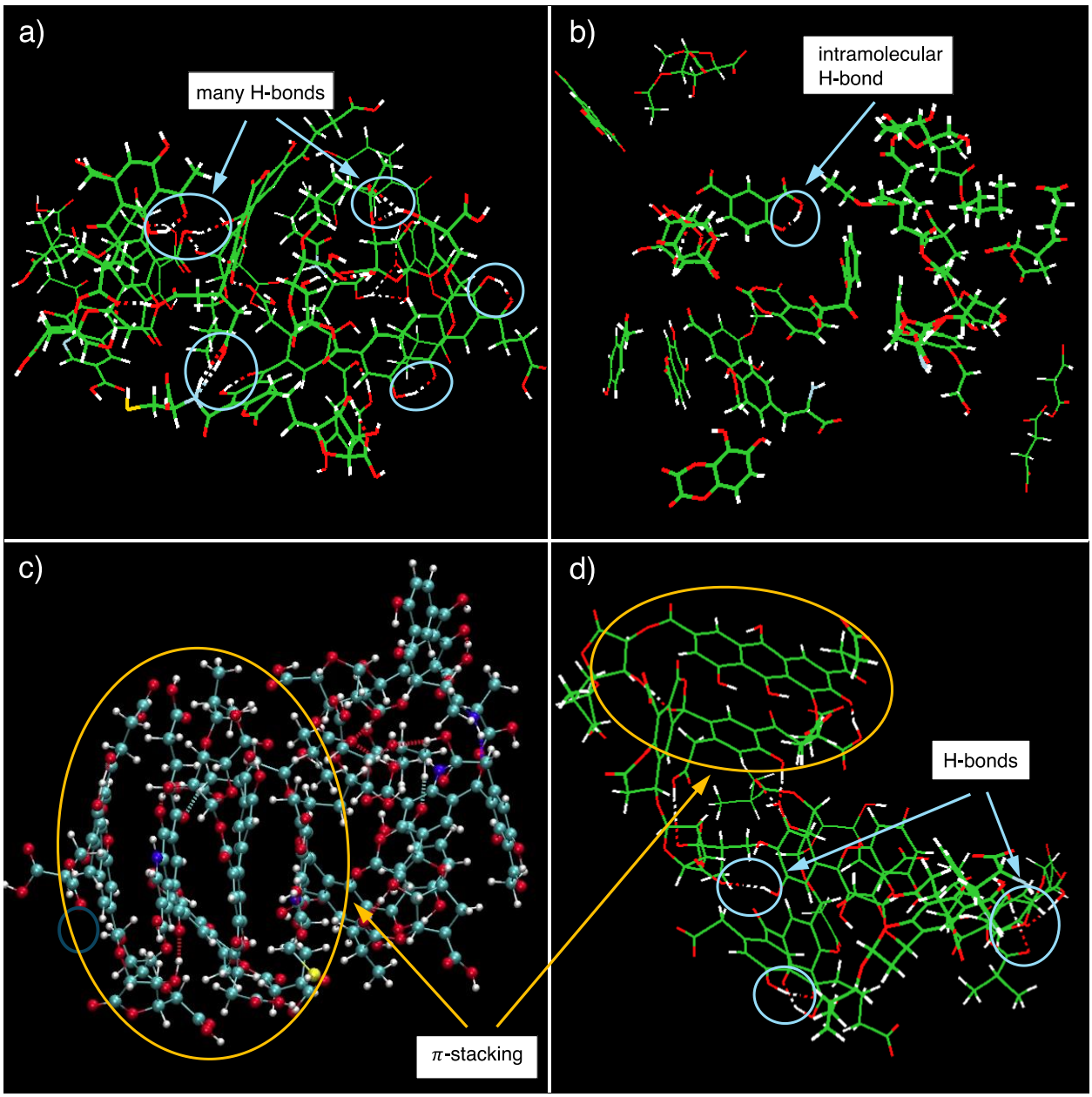

Figure 2.2 Snapshots of molecular dynamics (MD) simulations of model dissolved organic matter (DOM) including a) Suwanee River fulvic acid (SRFA) in a vacuum, b) SRFA in water, c) Suwanee River humic acid (SRHA) in a vacuum, and d) SRHA in water. The models were based on SRFA and SRHA chemical characteristics presented by Leenheer et al. (2001) using principles proposed by Vialykh et al. (2019) and Vialykh et al. (2020). Selected molecules were modeled with deprotonated carboxylic groups and protonated hydroxyl groups, allowing the pH of the systems to be considered ~5−6 (Kalinichev & Kirkpatrick, 2007). The systems were packed using Packmol software (Martinez et al., 2009) with periodic boundary conditions. The ReaxFF protein force field (Monti et al., 2013; Zhang & van Duin, 2018) was used to perform MD simulations and energy minimizations of the models.

DOM naturally coexists with inorganic molecules and ions, soil colloids, particulate organic matter, and microbes. However, the use of DOM isolates as representatives of organic matter in the natural environment remains an essential approach to studying its composition and reactivity across diverse sources and applications (Chin et al., 2023; MacCarthy, 1976; Thurman & Malcom, 1981). DOM is operationally defined as the fraction of natural organic matter in a water sample that passes through a sub-micron cutoff filter, typically between 0.2-0.7 mm (Thurman & Malcom, 1981; Perdue & Ritchie, 2003). The components of DOM discussed herein thus include operationally defined humic acids (HAs; insoluble at pH 1) and fulvic acids (FAs; soluble at pH 1) (Thurman & Malcom, 1981). The HA and FA fractions that make up the majority of aquatic DOM are studied frequently due to their water solubility (Perdue & Ritchie, 2003), commercial availability of reference materials (International Humic Substances Society, 2024), and their well-established isolation methods including solid-phase extraction (SPE) (Thurman & Malcom, 1981) and reverse osmosis (RO)-electrodialysis (Koprivnjak et al., 2006). Natural organic matter (NOM) is a broader term that includes substances extracted from solids such as soil and sediment and isolated through a variety of methods (Thurman & Malcom, 1981; Perdue & Ritchie, 2003; International Humic Substances Society, 2024). While there has been a parallel decades-long effort to understand the structure and nature of soil organic matter (SOM; organic matter isolated from soil and re-dissolved in water) (Swift, 2018; Hayes & Swift, 2020), this perspective focuses on DOM observed in, or isolated from, aquatic environments. This is not to say that SOM research has not provided valuable insight to the structure and behavior of DOM, but the differences between SOM and DOM composition, mineral content, and environmentally relevant concentrations warrant their unique structural models.

Recent advances in analytical methodologies have provided more detailed descriptions of the chemical composition of DOM. High resolution mass spectrometry (HRMS) and nuclear magnetic resonance (NMR) spectroscopy have revealed that DOM contains a variety of functional units including aromatic rings, alkenes, paraffinic, carboxylic acid, ester, amide, ether, alcohol, phenolic, carbonyl, carbohydrate, amine, heterocyclic amine and furan, and small amounts of peptides and condensed aromatic structures (Mopper et al., 2007; Hertkorn et al., 2008; Sleighter & Hatcher, 2007; Mitschke et al., 2023). Other techniques, such as size-exclusion chromatography (SEC), UV-visible spectrophotometry, and fluorescence spectroscopy have provided complementary information on the molecular size and optical properties of DOM (Mao et al., 2017; Del Vecchio & Blough, 2004; McKay, 2020; Reemtsma et al., 2008). Despite these analytical advances, the exact individual chemical structures of DOM are neither well-defined nor identical across DOM sources, making it challenging to converge on a 3D model that represents the observed behaviors and properties of chemically diverse DOM. The chemical composition of DOM, while important for understanding DOM structure, is not discussed herein given that it was thoroughly addressed in a recent perspective (Buckley et al., 2024). Rather, this article reviews fundamental principles that drive interactions between DOM molecules and evaluates evidence regarding DOM structure. We aim to clarify the MDAM as a framework for DOM structure and initiate further exploration of the influence of DOM structure on its behavior in both natural and engineered systems.

2.4 Thermodynamic considerations

Association of molecules in aqueous solution requires a thermodynamic driver favoring assembly over solvation of individual molecules. Consider a single molecule (M) in equilibrium

with another molecule or assembly of molecules (M_n), associating to form a larger assembly (M_{n+1}) (Equation 2.1):

$$M + M_n \rightleftharpoons M_{n+1} \qquad \left(K_{eq} = \frac{[M_{n+1}]}{[M_n][M]}\right) \tag{2.1}$$

$$\Delta G_{solv,asbl} = RT\ln(K_{eq}) = \Delta H - T\Delta S \tag{2.2}$$

The hydrophobic effect, or the tendency for water molecules to interact more with themselves than with larger and less polar solutes, can explain the association of molecules through the free energy cost of solvating individual molecules. Associations will be favorable if the free energy of solvation of an assembly ($\Delta G_{solv,asbl}$) is lower than the sum of $\Delta G_{solv,M}$ for its individual molecules (Equation 2.2) (Chandler, 2005; Schwarzenbach et al., 2002). For a solute with a surface area (SA) less than 1 nm^2, individual solvation will be favorable because the hydration shell around the solute maintains its H-bonding structure, minimizing the change in enthalpy (ΔH, Equation 2.2) (Chandler, 2005; Schwarzenbach et al., 2002). Consequently, $\Delta G_{solv,M}$ for small molecules is dominated by entropy ($T\Delta S$ term, Equation 2.2). For a solute with a SA above 1 nm^2, $\Delta G_{solv,M}$ will be dominated by the enthalpic cost of breaking H-bonds between water molecules to form an interface around the solute. If an individual solute of this size can compensate for the ΔH cost by forming new interactions, i.e. H-bonds with water, $\Delta G_{solv,M}$ may be favorable. However, if a large apolar solute can form intermolecular associations with other solutes or water to sufficiently minimize ΔH, $\Delta G_{solv,asbl}$ will be lower than $\Delta G_{solv,M}$, and the formation of assemblies will be favorable.

In the case of DOM, consider a spherical DOM molecule 1 nm in diameter and 1.0-1.4 g/cm^3 in density, corresponding to a MW of only ~300-400 Da (NanoCompsix, 2024). There is agreement across techniques that the average MW of DOM is between 0.5-1.2 kDa (Aiken & Malcom, 1987; Chin et al., 1994; Leenheer et al., 2001; Perdue & Ritchie, 2003; Stenson et al.,

2003; Peuravuori et al., 2007; McAdams et al., 2018). Therefore, most DOM molecules would fit into the enthalpy-driven category of hydration, for which associations may be thermodynamically favorable, especially for more hydrophobic (apolar) DOM molecules. Generally, increasing concentration should favor the formation of more and/or larger assemblies (Equation 2.1). At a high enough concentration, however, the SA of an assembly may reach a limit at which the assembly is no longer fully solvated and precipitates out of solution. It is worth noting that not all components of DOM have the same aqueous solubility, and it is possible that only the larger and more hydrophobic (apolar) molecules form associations while smaller hydrophilic (polar) molecules remain dissolved.

2.5 Evidence of DOM behavior and properties

2.5.1 DOM molecular size and weight

2.5.1.1 Comparison of techniques

One of the original arguments favoring the supramolecular assembly model was the seeming discrepancy of DOM molecular weight determined through SEC as compared to vapor pressure osmometry (VPO) and mass spectrometry (MS). While most techniques are in agreement that the number average MW (M_n) of DOM is between 0.50-1.2 kDa (Aiken & Malcom, 1987; Chin et al., 1994; Leenheer et al., 2001; Perdue & Ritchie, 2003; Stenson et al., 2003; Peuravuori et al., 2007; McAdams et al., 2018), some earlier work using SEC coupled to either UV or total organic carbon (TOC) detection reported M_n values between 1-10 kDa (Piccolo et al., 1996; Conte & Piccolo, 1999; Perminova et al., 1998). It was suggested based on some of these studies that the observed high AMW of DOM was due to the ability of SEC to detect supramolecular assemblies, which are dissociated during MS ionization. However, there are a few nuances regarding SEC

methodology that may explain the large discrepancy between SEC and MS. First, inadequate AMW standards such as polydextranes and globular proteins have been shown to overestimate AMW by up to a factor of five (Chin et al., 1994; Perminova et al., 1998; McAdams et al., 2018) whereas poly(styrenesulfonate) (PSS) and poly(propylene glycol) (PPG) standards yield M_n in line with M_n or MW ranges determined through MS, VPO, and diffusion-ordered NMR spectroscopy (DOSY-NMR) (Aiken & Malcom, 1987; Chin et al., 1994; Leenheer et al., 2001; Perdue & Ritchie, 2003; Stenson et al., 2003; Peuravuori et al., 2007; Lam & Simpson, 2009; McAdams et al., 2018). Second, SEC paired with UV detection has been shown to yield higher AMW compared to SEC-MS (These & Reemtsma, 2003; Peuravuori et al., 2007; Hawkes et al., 2019) which is likely due to the bias of UV toward chromophoric DOM and the preferential ionization of lower MW compounds. However, despite the diverse molecular formulae detected using electrospray ionization (ESI), atmospheric pressure chemical ionization (APCI), and atmospheric pressure photoionization (APPI), in either positive and negative mode, the majority of AMWs detected in Suwannee River fulvic acid (SRFA) are below 1 kDa (These & Reemtsma, 2003; Rostad & Leenheer, 2004; Peuravuori et al., 2007; Mopper et al., 2007; Hertkorn et al., 2008). Last, one could imagine that ionization may cause fragmentation of macromolecules, resulting in lower AMW. Yet, the aforementioned ionization techniques are all considered “soft”, meaning they should not break covalent bonds (Mopper et al., 2007). Because recent advances in SEC methodology and their application to DOM have proved that the MW discrepancy between measurements is much narrower than previously thought, there is no direct support of the supramolecular assembly model based on a MW discrepancy.

Despite the challenges in measuring accurate MW, SEC has nonetheless been helpful to understand noncovalent interactions between DOM molecules. In two separate SEC-HRMS

studies using different aquatic DOM sources, many identical molecular formulae of DOM were identified across several SEC size fractions of DOM (These & Reemtsma, 2003; Peuravuori et al., 2007; Reemtsma et al., 2008). Similarly, Peuravuori et al. (2005) discovered overlapping molecular structures across SEC and ultrafiltration (UF) size fractions using ^{1}H and ^{13}C NMR spectroscopy. There are two possible explanations for this observation: (1) high MW (HMW) DOM is composed of assemblies of low MW (LMW) DOM molecules that dissociate during ionization, or (2) HMW DOM is made of macromolecules of LMW DOM molecules held together by covalent bonds which, despite using a soft-ionization technique, fragment at weak points due to the high cone voltage applied to ionize heavy molecules (These & Reemtsma, 2003). Wang et al. (2024) using high-performance SEC (HPSEC) with UV detection, found that the molecular weight distribution (MWD) curve of Suwannee River HA (SRHA; 115 mg/L) shifted to higher AMW with an increase in pH (5 to 6) or ionic strength (IS; 100 to 400 mM, adjusted with NaCl). The former observation appears to be in accord with the macromolecular model if it is assumed that increasing pH induces swelling by charge repulsion among the increased number of negative charges. The latter observation, however, contradicts the macromolecular model since charged macromolecules will shrink with increased IS due to solvent exclusion and mitigation of charge repulsion because of charge-screening. It is more probable that increasing IS causes a shift to higher AMW due to the "salting out" effect (Schwarzenbach et al., 2002), which lowers individual solute solubility and thereby promotes supramolecular assembly.

2.5.1.2 Concentration effects on AMW

The observation that there is a lack of concentration dependence on AMW in some VPO and SEC experiments (Reuter & Perdue, 1981; Pavlik & Perdue, 2015; Wang et al., 2024) remains puzzling. Such a result seems inconsistent with the supramolecular model: if molecular

associations occur in DOM, increasing the number of DOM molecules should result in the formation of more and/or larger assemblies (Equation 2.1). One could expect that concentration and osmotic pressure (measured through VPO) would have a nonlinear relationship for DOM since an assembly of *n* molecules has 1/*n* the molality of *n* solvent-separated molecules. The deviation from linearity would become greater at high concentrations if there are increased molecular associations. Two studies (Reuter & Perdue, 1981; Pavlik & Perdue, 2015) reported a linear relationship between osmotic pressure and DOM concentration (6 -20 g/L at pH ~2), seem to contradict the supramolecular model. However, the measurements were taken at unrealistically high concentration and low pH compared to environmental systems, bringing into question whether the VPO studies accurately represent associational behavior of DOM. Using HPSEC with UV detection, Wang et al. (2024) reported that the normalized HPSEC-derived MWD curves of SRHA at environmentally relevant concentrations (14-143 mg/L) and pH (6) essentially overlapped, regardless of detection wavelength (254-320 nm). These observations imply that either DOM exists as non-interacting individual molecules or the formation of associations between DOM molecules is concentration independent.

To rationalize the concentration-independence of potential DOM associations, we must consider the strength of interactions between DOM molecules and the concentration range used in experiments. If assembly were simply driven by the hydrophobic effect, assemblies would continue to grow as the concentration of DOM increased. If the size of the assembly was limited, an increase in concentration would result in more assemblies, not larger ones. Transmission electron microscopy (TEM) images reveal particles much larger in size (up to >1 μm) (Baalousha et al., 2006; Baigorri et al., 2007; Wang et al., 2024) than are possible by molecular entities of < 5 kDa. TEM, however, is performed in a vacuum, reflecting conditions of extremely high

concentrations. The particle sizes observed by TEM suggest that extremely high DOM concentrations can drive the formation of assemblies large enough to precipitate out of solution, bringing into question whether the VPO studies (6 -20 g/L at pH ~2) accurately represent associational behavior of DOM. These large particles observed by TEM, possibly precipitates, analogous to the loosely-knit aggregates formed through weak associations of smaller, tightly-knit aggregates (Wang et al., 2024) similar the two-tier model for DOM 3D structure proposed by Wells & Stretz (2019). While these small, tightly-knit assemblies appear to be stable at low, environmentally-relevant concentrations, the large, loosely-knit assemblies seem to only form under unrealistically high concentrations, driven by their solubility thermodynamics.

The intermolecular forces holding together the tightly-knit assemblies have been proposed to be exceptionally strong H-bonds between weak acid functional groups known as charge-assisted H-bonds, (–)CAHB (Wang et al., 2024). (–)CAHB can form when the interacting groups have similar pK_a values (e.g., between carboxyl groups) and are far stronger than ordinary H-bonds by a factor of 2-10, with a bond strength of up to 35 kcal mol^{-1} (Gilli & Gilli, 2007; Gilli et al., 2009). This exceptional strength is due to the close sharing of the proton, conferring some covalent character on the bond. The (–)CAHB between carboxyl groups on DOM may be written ⦚-$CO_2^-\cdots H^+\cdots {}^-O_2C$-⦚. While it could be argued that tightly-knit assemblies are formed as a result of metal bridging between DOM and metals such as iron (Wrobel et al., 2003), which will be quite relevant in natural environments, the role of metals should be negligible in isolated DOM that has undergone ion-exchange (International Humic Substances Society, 2024). Wang et al. (2024) showed that cation-exchange pretreatment of SRFA had no effect on its MWD, despite removing a further 80% of Ca and Mg, 30% Al, and 0-16% Fe. Additionally, several authors (Piccolo et al., 1996; Conte & Piccolo, 1999; Piccolo & Spiteller, 2003; Wang et al., 2024) have shown that

addition of weak acids, including simple carboxylates and phosphate ion that are capable of forming (–)CAHB cause shifts to a lower MWD, shifts in the zeta potential-pH curve, and changes in pH, all consistent with disruption of (–)CAHB between DOM molecules. Consistently, the addition of polar solutes incapable of forming (–)CAHB had no effects. In summary, while there is not a seeming MW discrepancy between SEC, MS, and VPO, evidence from SEC-UV (Wang et al., 2024) and SEC-HRMS (These & Reemtsma 2003; Peuravuori et al., 2007) suggest that HMW DOM contains both genuinely HMW macromolecules *and* assemblies of LMW carboxylates of DOM which interact through (–)CAHB.

2.5.2 DOM particle size

Arguments favoring the supramolecular assembly model have often been supported by DOM "particle" size and diffusivity measurements, where "particle" describes an assembly of DOM molecules, as described in the literature. TEM and proton correlated spectroscopy (PCS) have revealed DOM particles from <10 nm to > 1 μm in diameter (Baalousha et al., 2006; Baigorri et al., 2007; Wang et al., 2024). The upper end of particle diameters detected by TEM correspond with molecular weights >100 kDa and, based on the definition of DOM, fall into the particulate phase (>0.2 μm). The observation of these particles supports the concept of "loosely-knit" supramolecular assemblies that form at high concentration due to solubility limits. Despite using DOC concentrations much greater than usually found in the environment (45-800 mg L^{-1}), the TEM and PCS measurements have given insight into the mechanisms forming associations between DOM molecules. For instance, increasing IS causes an increase in particle diameter[10,55] and decrease in diffusivity (measured by DOSY-NMR) (Šmejkalová & Piccolo, 2008; Lam & Simpson, 2009), attributed to the "salting out" effect (Schwarzenbach et al., 2002) and consistent with SEC observations (Wang et al., 2024). Also, the addition of acetate causes a shift to lower

particle size (Baigorri et al., 2007) and greater diffusivity (Šmejkalová & Piccolo, 2008), supporting the contribution of (–)CAHB to DOM supramolecular assemblies. Interestingly, through DOSY-NMR, Lam & Simpson (2009) found little formation of assemblies (diffusion rates indicative of individual molecules between 100-1000 Da) at concentrations <500 ppm, but aggregation increased with concentrations >500 ppm. This evidence suggests that DOM exists mostly as individual molecules and "tightly-knit" aggregates at environmentally-relevant concentrations, but "loosely-knit" supramolecular assemblies form at high concentration and IS.

2.5.3 Sorption of organic compounds to DOM

Many anthropogenic organic compounds associate with (i.e., sorb to) DOM in solution (Pan et al., 2007; Pan et al., 2008; Iglesias et al., 2009; Maoz & Chefetz, 2010; Ding et al., 2013; Rizzuto et al., 2021). These associations can be attributed to the lowered free energy of associated compounds compared to freely dissolved molecules. This concept constitutes indirect support for the supramolecular model because, if an added solute can associate with DOM, then individual DOM molecules can potentially associate with each other as well. Studies of the association of compounds with DOM have shown there is a degree of specificity in these interactions as manifested by isotherm nonlinearity and/or competitive effects (Iglesias et al., 2009; Rizzuto et al., 2021), even for apolar compounds such as polyaromatic hydrocarbons (Pan et al., 2007). Specific interactions may include H-bonding, electrostatic interactions, and π-stacking. While it is evident that DOM association can provide a 3D partitioning phase, it is also possible that the coiling of individual macromolecules in response to intramolecular forces or solution chemistry (e.g., pH or IS) can create microscopic 3D phases into which solutes can partition (Latch & McNeill, 2006; Pan et al., 2007; Pan et al, 2008; Grandbois et al., 2008). However, if individual

macromolecules are responsible for this behavior, they would have to be sufficiently large to coil in such a way as to create micro partition domains.

2.5.4 DOM optical properties

Investigating the optical properties of DOM has not only increased our understanding of DOM phototransformations, CO_2 production, and indirect photodegradation of contaminants, but has elucidated the composition and structure of DOM. A multitude of evidence has supported the influence of closely-interacting chromophores on the absorbance and fluorescence of DOM: the contribution of charge-transfer (C-T) interactions in the long-wavelength UV-visible absorbance of DOM (Del Vecchio & Blough, 2004), the solvent inaccessibility of a portion of chromophores thought to be buried in hydrophobic "pockets" of DOM, the correlation of ultra-fast fluorophore excitation energy transfer (EET) with the tightness of aromatic species packing (Yakimov et al., 2021), and the detection of higher reactive intermediate concentrations by hydrophobic compared to hydrophilic probe compounds (Latch & McNeill, 2006; Hassett, 2006; Grandbois et al., 2008; Yan et al., 2021). First, it is evident that chromophoric moieties interact with one another, but whether these interactions or hydrophobic "pockets" of DOM are *inter*-molecular (within a supramolecular assembly) or *intra*-molecular (within a macromolecule) is uncertain (Del Vecchio & Blough, 2004). Second, recent evidence has suggested that these chromophore interactions contribute minimally to the optical properties of DOM. This work includes computational models demonstrating that the absorption spectra of DOM can be explained almost entirely by the superposition of the properties of individual molecules (McKay et al., 2018; Vialykh et al., 2020; McKay, 2020; Leresche et al., 2022), computational models showing that 10-19% of model SRFA carbon atoms are buried in solvent-inaccessible pockets (Vialykh et al., 2020), and fluorescence quenching experiments showing between 10-50% of DOM fluorophores (constituting only ~30%

of chromophores) (McKay et al., 2018) are inaccessible to aqueous solvent (Li & McKay, 2023). This evidence suggests that interactions between chromophores, whether they are *inter*-molecular or *intra*-molecular, involve less than 20% of carbon atoms in DOM. Last, the higher concentrations of singlet oxygen and hydroxyl radicals when measured using hydrophobic (apolar) probe compounds has two possible explanations. One hypothesis is that the apolarity of a probe molecule allows it to enter a "hydrophobic microenvironment" within a DOM assembly where there are higher concentrations of photosensitizers, explaining the enhanced production of RIs (Latch & McNeill, 2006; Hassett, 2006; Grandbois et al., 2008; Yan et al., 2021). An alternative hypothesis is that the addition of a probe compound triggers association of hydrophobic molecules around the probe, many of which are photosensitizers. The second hypothesis, if true, may also apply to the sorption of organic compounds to DOM: in other words, supramolecular association of DOM molecules is a dynamic process that can be induced by the addition of small hydrophobic molecules. In summary, DOM optical properties alone do not provide sufficient evidence to distinguish *inter*- and *intra*-molecular interactions, but nonetheless support a model for DOM structure that involves a mixture of solvent-separated molecules and closely-interacting molecules.

2.5.5 Computational modeling of representative DOM molecules

Molecular dynamics simulations and density functional theory (DFT) calculations offer insight into DOM 3D structure (Trout & Kubicki, 2006; Aquino et al., 2011; Petrov et al., 2017; Vialykh et al., 2019; Vialykh et al., 2020; Escalona et al., 2023). These methods are usually applied to evaluate interactions among a few model units with molecular size of the molecular fragment/building block ~100-1000 Da selected to represent DOM molecules. While model DOM molecules readily form associations in the absence of solvent (computationally, in a vacuum) (Vialykh et al., 2019), the addition of water causes separation of assemblies due to the disruption

of some, but not all, intermolecular hydrogen bonds by water molecules (Trout & Kubicki, 2006; Aquino et al., 2011; Petrov et al., 2017; Vialykh et al., 2019; Escalona et al., 2023). MD simulations have also revealed that the predominant forces between model FA molecules are H-bonds, while "hydrophobic" and π-stacking interactions are predominant between the larger, more aromatic model HA molecules (Figure 2.2). As depicted in Figure 2.2 b) and d), model SRFA and SRHA in water exist as a mixture of solvent-separated molecules and supramolecular assemblies, best described by the MDAM. Nonetheless, computational models are subject to the molecules chosen to represent DOM, thus a greater portion of *intra*-molecular interactions may be observed if larger molecules are selected, or an absence of *inter*-molecular interactions if only small, polar molecules are chosen.

2.5 Recommendations for future work

Recent applications of diverse analytical and computational methods to the characterization of DOM have greatly expanded our understanding of DOM chemical composition, size, and reactivity. Evidence from single observations and techniques are insufficient to draw conclusions about DOM structure. For example, DOM optical properties, sorption of small organic molecules to DOM, and computational models of DOM could be plausibly explained by either the macromolecular or supramolecular models (Table 2.1). However, several techniques agree that most individual DOM molecules have an AMW lower than 2000 Da, which is inconsistent with a macromolecular framework. The preponderance of evidence from multiple studies and techniques supports the MDAM for DOM structure, described as a collection of solvent-separated molecules and molecular assemblies.

Table 2.1 Summary of major findings of DOM molecular properties and behaviors that have been used as evidence to support the supramolecular assembly model. Alternative hypotheses for the observations suggest the need for a new model (MDAM) to capture the full picture of DOM as both solvent-separated molecules and supramolecular assemblies.

Property or behavior	Analytical method(s)	Evidence supporting the supramolecular assembly model	Alternative hypotheses for the evidence	Reference
Molecular size and weight	VPO, HRMS, SEC, NMR	Multiple techniques agree on an average MW of 0.5-2 kDa, implying that assembly is thermodynamically favorable for many DOM molecules. Shifts to high AMW are seen with increasing IS and pH; shifts to low AMW occur with the addition of small carboxylic acids.	Concentration independence of AMW suggests DOM is comprised of solvent-separated molecules and/or stable assemblies.	Reuter & Perdue, 1981; Aiken & Malcom, 1987; Chin et al., 1994; Piccolo et al., 1996; Leenheer et al., 2001; Stenson et al., 2003; Perdue & Ritchie, 2003; Peuravuori et al., 2005; Peuravuori et al., 2007; Wang et al., 2024
Particle size	PCS, SEC, DOSY-NMR, TEM	DOM particle sizes range from <10 nm to >1 μm in diameter. Particle sizes generally increase with IS or pH.	Particle size measurements are performed at unrealistically high concentrations, suggesting large assemblies do not form in environmentally relevant conditions.	Morris et al., 1999; Baalousha et al., 2006; Baigorri et al., 2007; Šmejkalová & Piccolo, 2008; Lam & Simpson, 2009; Wang et al., 2024
Sorption of organic molecules	SEC, TEM	Organic molecules associate with DOM through site-specific interactions within a 3D, "hydrophobic pocket" of a DOM molecular assembly.	Associations of organic molecules may occur within a "hydrophobic pocket" of a coiled DOM macromolecule.	Pan et al., 2007; Pan et al., 2008; Iglesias et al., 2009; Maoz & Chefetz, 2010; Ding et al., 2013; Ni & Pignatello, 2018; Rizzuto et al., 2021; Wang et al., 2024
Optical properties	UV-vis absorb-ance, fluoresce-ence	A small portion of DOM chromophores are solvent-inaccessible, and RI production is higher when measured with hydrophobic probe compounds, suggesting the existence of "hydrophobic pockets" within a DOM assembly.	Solvent inaccessibility may occur within a hydrophobic pocket of a coiled macromolecule. Enhanced RI production could be due to associations *induced* by the presence of hydrophobic probe molecules.	Latch & McNeill, 2006; Hassett, 2006; Grandbois et al., 2008; Vialykh et al., 2020; Yan et al., 2021; Yakimov et al., 2021; Leresche et al., 2022; Li & McKay, 2023;
Computational modeling	MD, DFT	Model DOM molecules form assemblies in water and in a vacuum through H-bonding and other non-covalent interactions.	Computational models are biased toward the molecules chosen to represent DOM. A varied selection of model compounds may support a different structural model.	Trout & Kubicki, 2006; Aquino et al., 2011; Petrov et al., 2017; Vialykh et al., 2019; Vialykh et al., 2020; Escalona et al., 2023

VPO = vapor pressure osmometry; MS = mass spectrometry; SEC = size-exclusion chromatography; PCS = proton correlated spectroscopy; DOSY-NMR = diffusion-ordered nuclear magnetic resonance spectroscopy; TEM = transmission electron microscopy; IS = ionic strength; MD = molecular dynamics; DFT = density functional theory.

Moving forward, research objectives should focus on characterizing DOM assemblies and explaining the conflicting observations. Specifically, future work is needed to help rationalize the apparent lack of a concentration dependence of DOM associations across large concentration ranges as observed by Wang et al. (2024) (14-143 mg/L) and Reuter & Perdue (1981) and Pavlik & Perdue (2015) (6-20 g/L). The stability of tightly knit assemblies by (–)CAHB and possible precipitation of assemblies as such high concentrations likely explain some of the observed behavior, but concentration effects should be further explored across various water chemistries and DOM sources. Furthermore, research should aim to estimate the fractions of DOM molecules that form assemblies versus freely dissolve, further explore the contributions of (-)CAHB and weaker intermolecular forces, and evaluate the changes in DOM conformation with solution changes or the addition of organic contaminants. Understanding how DOM molecules of diverse sources interact with each other and their respective water matrices will help us better predict the environmental fate of contaminants, assess DOM biodegradation and phototransformations, and improve water treatment processes.

2.6 Acknowledgements

The authors acknowledge the conversations they had with members of the DOM scientific community that contributed to the inspiration and development of this perspective. These members include Patrick Hatcher, Garrett McKay, Michael Perdue, Irina Perminova, Robert Spencer, and Michael Thurman.

3. Unraveling the Mechanisms of Hydroxyl Radical Generation by Dissolved Organic Matter

This chapter is in progress and will be submitted as: Norris, K.E; Leresche, F.L.; Vialykh, E.; Mezyk, S.; Rosario-Ortiz, F.L. Unraveling the Mechanisms of Hydroxyl Radical Generation by Dissolved Organic Matter. **Expected Summer 2025.**

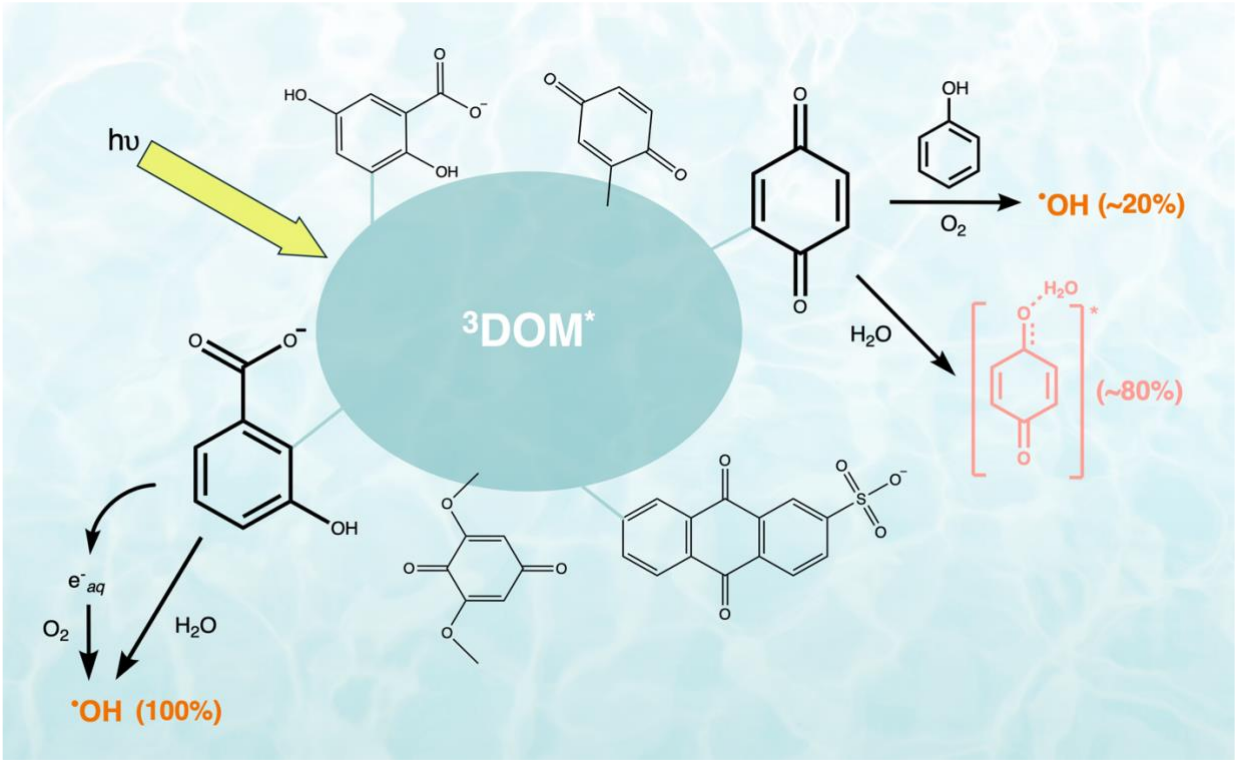

Figure 3.1 Graphical abstract for Unraveling the Mechanisms of Hydroxyl Radical Generation by Dissolved Organic Matter.

3.1 Abstract

Hydroxyl radicals (•OH) are a species of interest in the environmental fate of contaminants due to their fast and nonselective reactions with both organic and inorganic compounds. Sources of •OH in surface waters include the photolysis of nitrate and nitrite, the oxidation of ferrous iron in the presence of hydrogen peroxide (H_2O_2; the Fenton reaction), and the photolysis of dissolved organic matter (DOM). The production of •OH by DOM is known to occur through two pathways: 1) the generation of H_2O_2 by DOM followed by H_2O_2 photolysis (known as the H_2O_2-dependent

pathway) and 2) the direct generation of •OH by DOM without involvement of H_2O_2 (the H_2O_2-independent pathway). However, the mechanisms of the H_2O_2-independent pathway have remained unclear due to unintentional reactions between •OH (or other lower-energy hydroxylating species) and probe and quencher compounds. In this work, the pathways of •OH formation by six model quinones and hydroxybenzoic acids were distingquished using methane and catalase to quench free •OH and H_2O_2, respectively. We demonstrated that the hydroxylating species produced by quinones are mainly quinone-water exciplexes, but quinones may form free •OH in the presence of an electron donor through an H_2O_2-dependent pathway. Hydroxybenzoic acids were shown to produce free •OH through both H_2O_2-dependent and -independent pathways. Based on these results, we estimate that only 10-20% of all hydroxylating species produced by DOM in natural surface waters are free •OH, implying that previous work has overestimated •OH steady-state concentrations and their contribution to contaminant fate.

3.2 Introduction

Hydroxyl radicals (•OH) are a species of interest in natural aquatic systems due to their role in the degradation of contaminants such as pesticides and pharmaceuticals. Sources of •OH include nitrate, nitrite, and dissolved organic matter (DOM) (Zhou & Mopper, 1990; Qian et al., 2001; Vaughan & Blough, 1998; Page et al., 2011; Dong & Rosario-Ortiz, 2012), with steady-state concentrations ranging between 10^{-17}-10^{-15} M in surfaces waters. While the formation mechanisms of •OH by nitrate and nitrite is well-known, the pathways by which •OH is produced through DOM light absorption have remained unclear. Pathways of •OH formation by DOM are typically differentiated based on the involvement of H_2O_2. The H_2O_2-dependent pathway leads to •OH through the production of superoxide ($O_2^{\bullet-}$) through reduction of O_2 by $^3DOM^*$ or $DOM^{\bullet-}$, subsequent $HO_2^\bullet$ dismutation leading to the formation of H_2O_2, and direct photolysis of H_2O_2 or

photo-Fenton reactions (Table S1; Cheng et al., 2025). In a recent article, the H_2O_2-dependent pathway was shown to only contributes to 10-20% of $^{\bullet}OH$ produced by DOM (Cheng et al., 2025), which is much less than previously estimated contributions of up to 50% (Vaughan & Blough, 1998; Page et al., 2011). The previous overestimates of the H_2O_2-dependent pathway are likely due to overlooked scavenging of $^{\bullet}OH$, and possibly triplet states, by catalase, an enzyme used to quench H_2O_2 (Cheng et al., 2025). The reaction between $^{\bullet}OH$ and catalase has not been thoroughly investigated, but the large (250 kDa) structure of catalase contains many aromatic amino acids and C-H bonds that may undergo $^{\bullet}OH$-addition and H-abstraction, respectively, and thus should not be ignored in the use of catalase as an H_2O_2 quencher.

The H_2O_2-independent pathway, accounting for the remaining 80-90% of $^{\bullet}OH$ produced by DOM (Cheng et al., 2025), is poorly understood. It has been proposed that $^3DOM^*$ with a high one-electron reduction potential [$E^{\circ *}(^3DOM^*/DOM^{\bullet -})$] could generate $^{\bullet}OH$ through the oxidation of water or hydroxide (Alegria et al., 1997; Sur et al., 2011; Sun et al., 2015), or alternatively, through the abstraction of H from water after photoionization of a substituted phenol (Canonica, 1995; Sun et al., 2015; Wan et al., 2024) (Table S1, Scheme 1). Nonetheless, the H_2O_2-independent pathway has remained elusive due to the limitations of $^{\bullet}OH$ probe molecules and the challenge of distinguishing $^{\bullet}OH$ from lower-energy hydroxylating species which react with similar mechanisms and rates to $^{\bullet}OH$ (Page et al., 2011; McKay & Rosario-Ortiz, 2015; Couch et al., 2022).

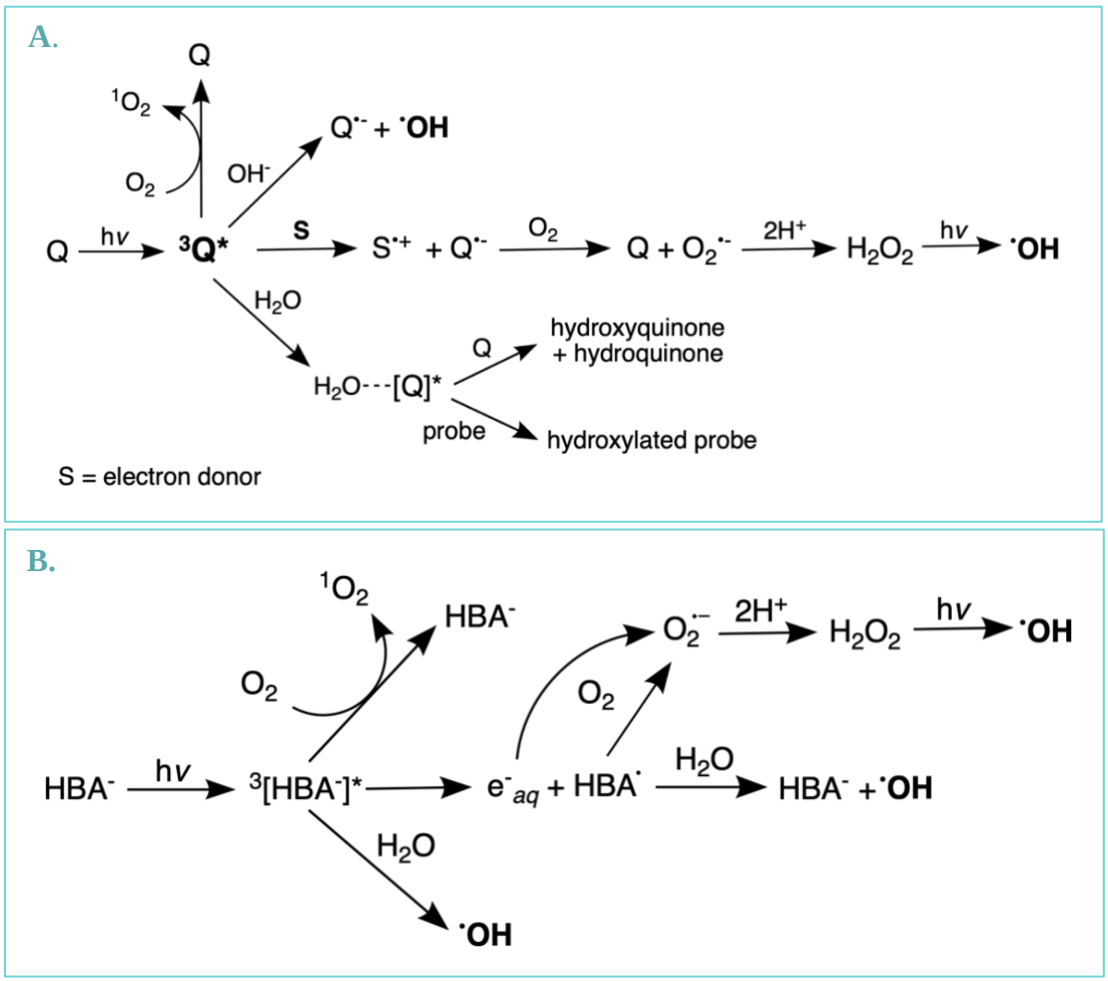

Scheme 3.1 Possible pathways for the formation of ˙OH and hydroxylation of probe compounds by quinones (A) and hydroxybenzoic acids (B).

A common method to measure hydroxylating species is through quantifying the transformation of probe compounds. In the general case of the hydroxylation of an arene, the initial step is the addition of ˙OH to the ring to yield a hydroxycyclohexadienyl radical (hydrogen abstraction is not a significant pathway (Pan et al., 1993; Aston et al., 1995). Following the formation of this radical, the next step is an oxidation to yield the hydroxylated product(s) (phenol in the case of benzene). It is expected that in most aerated solutions the oxidant is oxygen, which adds to the radical to form a peroxyl radical which will decay into the hydroxylated product(s). It should also be noted that the reaction between ˙OH and the probe compound also produces $HO_2^\bullet$,

which ultimately can lead to the formation of •OH (Table S1). This would be a catalytical cycle if the yield of $HO_2^{\bullet}/O_2^{\bullet-}$ dismutation was close to unity, but in surface waters $HO_2^{\bullet}/O_2^{\bullet-}$ also disappear by other mechanisms (Le Roux et al., 2021). The production of $HO_2^{\bullet}/O_2^{\bullet-}$ is nevertheless a limitation of •OH probes, as it can affect the amount of •OH produced in the system.

In addition to ambiguity resulting from the use of different probe compounds, the observed formation of lower-energy hydroxylating species have complicated the study of •OH formation. Previous work has shown that the production of hydroxylating species from DOM is primarily attributed to quinones ($\Phi_{\bullet OH,\ 254nm}$ = 0.017-0.047) and hydroxybenzoic acids ($\Phi_{\bullet OH,\ 254nm}$ = 0.054-0.063, $\Phi_{\bullet OH,\ 300nm}$ = 0-0.0080) (Sun et al., 2015; Couch et al., 2022). However, studies on the photochemistry of quinones, namely *p*-benzoquinone (PBQ) and methyl-benzoquione (MBQ) have suggested that these molecules do not form •OH, but that an intermediate, proposed to be a quinone-water exciplex, was responsible for the hydroxylation of the probe compounds (Pochon et al., 2002; von Sonntag et al., 2004; Gan et al., 2008; McKay & Rosario-Ortiz, 2015, Couch et al., 2022). McKay & Rosario-Ortiz showed that the hydroxylation of benzene to phenol in the presence of PBQ had no activation energy, also suggesting the involvement of an intermediate. Additionally, Page et al. found that several DOM sources did not follow the expected quenching by methane (a probe compound thought to be selective to •OH due to its high C-H bond strength), supporting the formation of lower-energy hydroxylating species by DOM (Page et al., 2011).

To study the mechanisms of formation of hydroxylating species by DOM, it is imperative to use model compounds for which the exact structures and properties are known. Model compounds are selected based on functional groups known to contribute to the composition and reactivity of DOM (Buckley et al., 2024). Although the elemental composition and chemical formulae of DOM has been well-characterized, the complexity of its many chemical constituents

makes it difficult to delineate exact chemical structures in DOM and isolate their contributions to specific mechanisms such as •OH formation. Recent work has shown that many of the photochemical properties of DOM can be mostly explained by a set of known functionalities (Leresche et al., 2022; McKay et al., 2021), thus the use of model sensitizers is a justifiable and necessary approach to understanding the specific chemical interactions that occur with DOM.

This objective of this article is to estimate the contributions of each •OH formation pathway from DOM. Methane and quenching methods were developed to distinguish the production of •OH and •OH-like species and catalase was used to distinguish the H_2O_2-independent and H_2O_2-dependent pathways. Rates of •OH formation were measured during the irradiation of a set of six model quinones and two hydroxybenzoic acids (Figure A.1). This work will ultimately lead to better accuracy in measurements of •OH steady-state concentrations ($[^{\bullet}OH]_{ss}$) in both natural and engineered systems and understanding how DOM composition influences •OH production.

3.3 Materials and Methods

3.3.1 Chemicals

All chemicals were purchased commercially and are listed in Table A.2. The model sensitizers, PBQ, MBQ, anthroquinone-2-sulfonate (AQS), 2,6-dimethoxy-*p*-benzoquinone (DPBQ), 4-hydroxybenzoic acid (HBA), and 2,4-dihydroxybenzoic acid (DHBA) were chosen based on previously reported evidence of their hydroxylating capacities (Figure A.1.; Sun et al., 2015; Couch et al., 2022). Though not fully representative of all compounds in DOM which produce •OH, the selected model quinones and hydroxybenzoic acids are expected to have the greatest contribution to overall •OH production based on their relative high quantum yields. All experimental solutions contained 25 μM of the probe compound, either terephthalic acid (TPA) or benzoic acid (BA), and 25 μM of a photosensitizer, except for the nitrite control experiments,

which contained 50 μM TPA or BA due to the fast reaction rate between nitrite and •OH. These concentrations were chosen to allow for at least 15% of •OH to react with methane during quenching experiments while keeping the probe compounds above their detection limits (Text A.2). All experiments were performed at pH 7 ($\pm$ 0.1) using 10 mM sodium phosphate buffer.

3.3.2 Photochemical experiments

The formation rates of •OH were quantified using the transformation rates of TPA at 300 nm and BA at 254 nm. These two wavelengths and probes were selected based to avoid extensive light absorption (Figure A.2) and direct photodegradation (Figure A.3) of the probe compounds and their transformation products as well as provide information about •OH production by DOM in both sunlit enironments and during UV-advanced oxidation processes (UV-AOP). Solutions were irradiated 21.5$\pm$0.5 ºC using a merry-go-round Rayonet RPR-100 (Southern New England Ultraviolet Company) with either 300 nm or 254 nm lamps (emission spectra shown in Figure A.4). Both lamps were treated as monochromatic. Experimental solutions were prepared in 9 mL cylindrical quartz tubes (diameter 1.25 cm) on a rotating carrousel and were irradiated from the side. The photon fluence rates of each lamp were measured using PNA/pyridine (300 nm) or uridine (254 nm) actinometers as outined in Text A.1.

3.3.3 Instrumentation

The transformation products of TPA (hydroxyterephthalic acid; hTPA) and BA (salicylic acid; SA) were quantified using a Agilent 1200 Series high performance liquid chromatography (HPLC) equipped with an Eclipse Plus XDB-C18 column (4.6 x 150 mm; 5 µm particle size). The HPLC methods for each analyte are described in Table A.3 along with their limits of detection (LOD) and quantitation (LOQ).

3.3.4 Methane quenching

To selectively quench free •OH, methane and oxygen were bubbled into solution for at least 20 seconds per mL in an 80:20 ratio. Maintaining at least 20% oxygen ensures that the transformation products of the probe compounds are formed at a consistent yield (Oturan & Pinson, 1995; Fang & Mark, 1996; Page et al., 2010; Page et al., 2011). The maximum dissolved methane concentration was calculated to be 1.18×10^{-4} M according to its aqueous solubility at the atmospheric pressure of Boulder, CO (Text A.2). Using an Agilent 7890A gas-chromatography instrument with flame ion detection (FID), the concentration of methane was found to be 8.43×10^{-4} M after ~10 minutes of bubbling an 80:20 CH_4:O_2 flow rate ratio into a 35 mL solution with 10 mM pH 7 phosphate buffer (Figure A.5). The GC-FID method is outlined elsewhere (Buckley et al., 2024). The direct photolysis of probe compounds in the presence of methane demonstrated a negligible impact of methane on probe transformation rates (Figure A.3).

3.3.5 Catalase quenching

To determine the contributions of the H_2O_2-dependent pathway, catalase was used to quench H_2O_2. An important consideration with the use of catalase is its potential interference as an •OH sink. To estimate the quenching of •OH by catalase under the experimental conditions, an accurate bimolecular rate constant between •OH and catalase ($k_{\bullet OH,cat}$) was needed. Previously reported values of $k_{\bullet OH,cat}$ are between $0.86\text{-}1.4 \times 10^{11}$ M^{-1} s^{-1} (Henglein et al., 1966; Gębicka & Metodiewa, 1988), however, these values were determined using activity rather than mass-based concentration. Since catalase activity per gram may vary significantly between standards (2000-5000 units/g; Millipore Sigma), $k_{\bullet OH,cat}$ was measured by mass-based concentration using the linear accelerator (LINAC) electron pulse radiolysis system at the Department of Energy Radiation Laboratory, University of Notre Dame. Details of the pulse radiolysis experiment are outlined

further in Text S3 and Figure A.7. $k_{\bullet OH,cat}$ was determined to be $5.57 \pm 0.07 \times 10^{11}$ M^{-1} s^{-1} (2229 L mg^{-1} s^{-1}), higher than previously published activity-based rate constants and slightly lower than a recently reported value of 2856 mL $units^{-1}$ s^{-1} (~5712 L mg^{-1} s^{-1}; Cheng et al., 2025). A rate constant of 5.57×10^{11} M^{-1} s^{-1} would limit the use of catalase to <5 units mL^{-1} with 25 μM probes and sensitizers to ensure <5% of •OH reacts with catalase. Since 5 units mL^{-1} may not be sufficient to quench H_2O_2 according to the definition of activity (one unit will decompose 1 μmol H_2O_2 per minute at pH 7.0 and 25°C), experiments using catalase used probe concentrations of 1 mM so that >97% of •OH reacted with BA or TPA at catalase concentrations up to 40 units mL^{-1}.

Catalase was added to experimental solutions in concentrations up to 40 units mL^{-1} from a 100 units mL^{-1} stock solution that was prepared weekly. The activity of each fresh catalase stock solution was measured using the standard enzymatic assay of catalase outlined by Millipore Sigma (2025). The rates of transformation of BA and TPA were slightly lower in the presence of 40 units mL^{-1} catalase (Figure A.3) likely due to light screening, but this was accounted for by applying a light screening factor (Text A.4). Figure A.6 shows the UV-vis absorption spectra of catalase.

3.3.6 Rates of •OH formation and quantum yield calculations

The rates of •OH formation ($r_{\bullet OH}$) were determined using the rates of formation of the transformation products of the probe compounds ($r_{form,TP}$) divided by their respective yields ($yield_{TP}$, Equation 3.1). A yield of 0.35 was applied for the formation of hTPA from TPA (Fang & Mark, 1996) and 0.204 was used for the formation of SA from BA (Cheng et al. 2025). Corrections for the direct photodegradation of hTPA and SA were made using calculations outlined elsewhere (Leresche et al., 2019). Rates of •OH formation were also corrected using a light-screening factor (Text A.4) since model sensitizers and probe compounds differ in light absorption at each wavelength. Light screening corrections were especially important for methane

quenching experiments because the use of low probe concentrations resulted in more variation in absorbance dominated by the model sensitizers, whereas the absorbance in experiments using high probe concentrations was dominated by the probe compound. For all experiments except for methane quenching, the concentration of model sensitizers was 25 μM and the concentrations of BA and TPA were 2 mM to ensure >95% of •OH reacted with the probe compounds. Due to the solubility limitation of methane, both probe compounds and sensitizers were added at concentrations of 25 μM for methane quenching experiments. At this concentration, the probe compound was neither the dominant scavenger nor a negligible sink for •OH (Text A.2).

$$r_{\bullet OH} = \frac{r_{form,TP}}{yield_{TP}} \tag{3.1}$$

Quantum yields of •OH formation ($\phi_{\bullet OH}(\lambda)$) were determined using Equation 3.2, where $r_{abs,S}$ is the rate of light absorption by the model sensitizer as defined in Equation 3.3. $E_p^0(\lambda)$ is the photon irradiance of the Rayonet reactor (M cm s^{-1}), $\varepsilon_S(\lambda)$ is the molar absorptivity of the model senstizer (M^{-1} cm^{-1}), and z is the pathlength (cm) of the quartz vial used in the irradiation experiments.

$$\phi_{\bullet OH}(\lambda) = \frac{r_{\bullet OH}}{r_{abs,S}} \tag{3.2}$$

$$r_{abs,S} = \sum E_p^0(\lambda) \frac{\varepsilon_S(\lambda)(1 - 10^{-\varepsilon_S(\lambda)[S]z})}{\varepsilon_S(\lambda)[S]z} \tag{3.3}$$

3.3.7 Methane quenching

To distinguish the amount of free •OH from lower energy hydroxylating species produced by each model sensitizer, the experimental rates of SA and hTPA formation in the presence of methane ($r_{form,TP(CH_4)}$) were compared with their predicted rates ($r_{form,TP(pred.)}$) (Text A.2). The predicted rates of TP formation in the presence of methane were determined using the

experimentally determined $r_{form,TP}$ multiplied by the change in scavenging rates with the addition of methane (Equation 3.4) where $k_{\bullet OH,PC}$, $k_{\bullet OH,S}$, and $k_{\bullet OH,CH_4}$ are the second-order rate constants between the probe compound, sensitizer, and methane, respectively. The predicted and experimentally observed quenching by methane were determined using Equations 3.5 and 3.6.

$$r_{form,TP(pred.)} = r_{form,TP} \times \frac{k_{\bullet OH,PC}[PC] + k_{\bullet OH,S}[S]}{k_{\bullet OH,PC}[PC] + k_{\bullet OH,S}[S] + k_{\bullet OH,CH_4}[CH_4]} \quad (3.4)$$

$$\%\, Q, pred. = 1 - \frac{r_{form,TP(pred.)}}{r_{form,TP}} \quad (3.5)$$

$$\%\, Q, exp. = 1 - \frac{r_{form,TP(CH_4)}}{r_{form,TP}} \quad (3.6)$$

3.4 Results

3.4.1 •OH quantum yields

Quantum yields for •OH formation ($\phi_{\bullet OH}$) were calculated based on the rates of SA and hTPA formation and rates of light absorption by each model sensitizer (Table 3.1). The $\phi_{\bullet OH}$ values reported in Table 1 assume that all hydroxylating species are free •OH. Quantum yields are all within the same order of magnitude as previously reported values for the same model sensitizers at 254 and 300 nm (Couch et al., 2022; Sun et al 2015). It is worth mentioning that the error on $\phi_{\bullet OH}$ for HBA at 300 nm is relatively high due to the low absorbance of HBA (Figure A.2) and thus low production of hydroxylating species under the experimental concentrations.

Table 3.1 Quantum yields of total hydroxylating species produced by model photosensitizers at 254 nm (measured with benzoic acid as a probe) and 300 nm (measured with terephthalic acid as a probe) calculated using Equations 3.2 and 3.3. The probe compounds were added at 2 mM and model sensitizers at 25 μM.

Model Sensitizer[a]	$\phi_{\bullet OH}(254nm)(\times 10^{-3})$	$\phi_{\bullet OH}(300nm)(\times 10^{-3})$
PBQ	16.6 (±0.7)	34.3 (±1.4)
MBQ	21.3 (±0.5)	14.7 (±1.4)
AQS	78.1 (±1.1)	35.3 (±1.0)
DPBQ	10.5 (±1.3)	2.3 (±0.3)
HBA	12.4 (±0.5)	15.2 (±5.3)
DHBA	9.6 (±0.7)	7.9 (±0.3)

[a]PBQ = p-benzoquinone, AQS = anthroquinone-2-sulfonate, MBQ = methyl-p-benzoquinone, DPBQ = dimethoxy-p-benzoquinone, HBA = 4-hydroxybenzoic acid, and DHBA = 2,4-dihydroxybenzoic acid.

[b]no significant production of hydroxylating species detected

3.4.2 Methane quenching

The impact of methane quenching on the rates of SA and hTPA formation varied in the presence of model quinones and hydroxybenzoic acid (Figure 3.2). For all model quinones at 254 nm, the addition of methane caused no significant reduction on SA formation rates (r_{SA}). At 300 nm, methane caused a slight reduction of hTPA formation rates (r_{hTPA}) in the presence of AQS and DPBQ, although the high error bars suggest that this reduction may be insignificant. Figure 3.2 also displays the expected rates of SA and hTPA formation in the presence of methane based on Equation 3.4. Since experimental r_{SA} and r_{hTPA} did not match the predicted rates, it is assumed that under the experimental conditions, quinones produce a species that does not react with methane but is capable of inducing the hydroxylation of the probe compounds.

For model hydroxybenzoic acids, a slight reduction in the rates of SA and hTPA formation was observed at 254 nm and 300 nm, respectively, except for HBA at 300 nm, for which no significant amount of hTPA was formed. At 254 nm, r_{SA} by HBA and DHBA in the presence of methane closely match the predicted rates, varying by only 5.8% and 1.1%. At 300 nm, r_{hTPA}

matches the predicted r_{hTPA} within 2.5% in the presence of DHBA. These results imply that hydroxybenzoic acids indeed form free •OH.

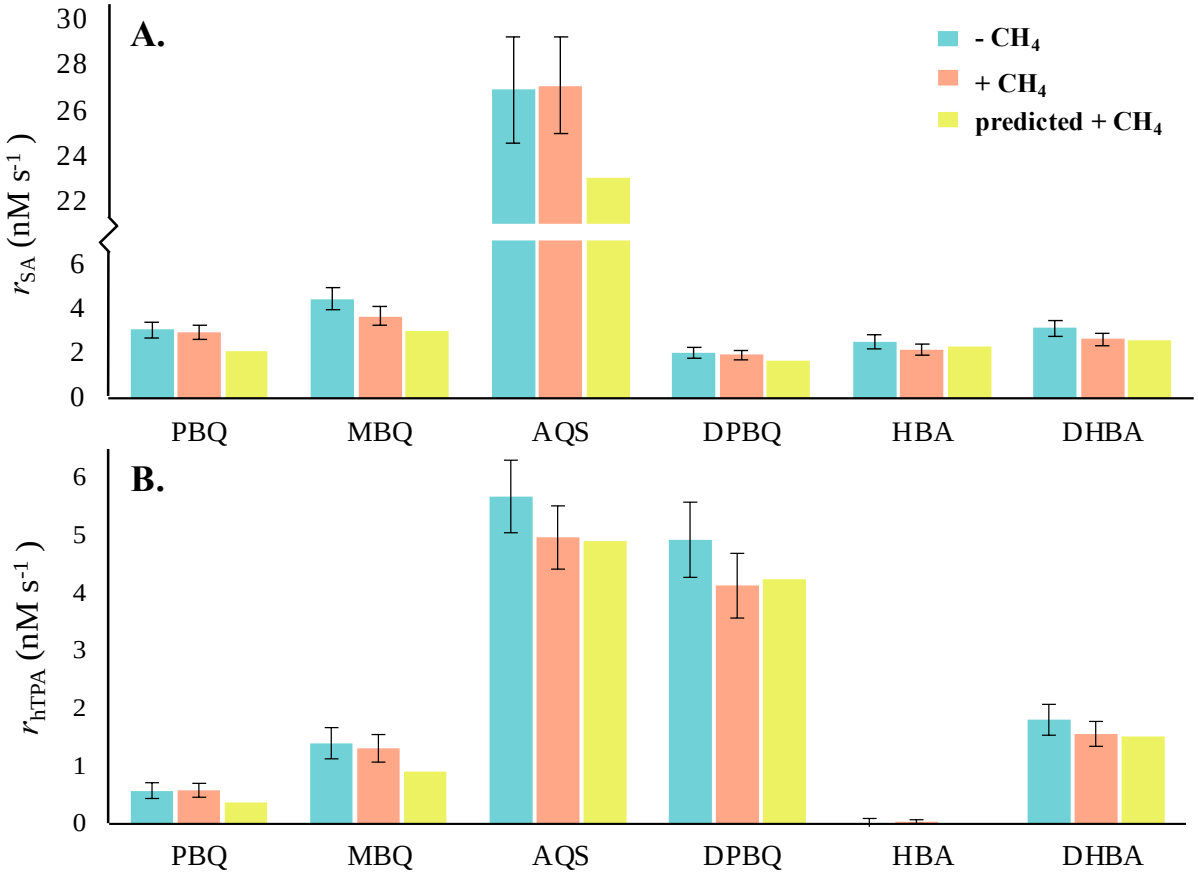

Figure 3.2 Rates of probe compound product formation in the presence of model quinones and model hydroxybenzoic acids at (a) 254 nm, showing the rate of formation of salicylic acid (r_{SA}), and (b) 300 nm, showing the formation rate of hydroxy-terephthalic acid (r_{hTPA}). Blue bars represent experiments with no methane added, pink-orange bars represent experiments in the presence of methane, and yellow-green bars represent the predicted r_{SA} for experiments in the presence of methane (Equation 3.4). Error bars represent confidence intervals at 95%. PBQ = p-benzoquinone, AQS = anthroquinone-2-sulfonate, MBQ = methyl-p-benzoquinone, DPBQ = dimethoxy-p-benzoquinone, HBA = 4-hydroxybenzoic acid, and DHBA = 2,4-dihydroxybenzoic acid. ND = no SA production detected.

3.5 Discussion

3.5.1 H_2O_2-independent pathway of •OH production by quinones

The lack of quenching of •OH production by most quinones in the presence of methane aligns with previous speculations that the hydroxylation of probe compounds in the presence of quinones is not due to •OH, but a lower-energy hydroxylating intermediate. A recent study confirmed that free •OH was not produced by PBQ or MBQ using various solvents a 5,5-dimethyl-1-pyrroline *N*-oxide (DMPO) spin trap with electron paramagnetic resonance (EPR) (Wang et al., 2024). Interestingly, Wang et al. (2024) found that the source of oxygen in the DMPO-OH adduct that has previously led researchers to believe that PBQ produces •OH (Ononye & Bolton, 1986; Alegría et al., 1997) was not PBQ, but H_2O. The findings of Wang et. al. support postulations that the identity of the intermediate hydroxylating species of PBQ and MBQ is a quinone-water exciplex ($[Q]^*\cdots H_2O$) (Pochón et al., 2002; Gan et al., 2008; Page et al., 2011; McKay & Rosario-Ortiz, 2015). A computational study (Karsili et al., 2015) suggested that a photoexcited PBQ-H_2O hydrogen-bonded complex forms locally excited $\pi\pi^*$ and $n\pi^*$ singlet states, which are coupled to charge-transfer states. The transfer of a proton from H_2O to PBQ is driven by the neutralization of the charge-transfer state (EDPT mechanism), leading to a PBQH•–•OH biradical. Karsili et al. (2015) offered that the biradical could dissociate to form free •OH, however, the energy barrier between the locally excited and charge-transfer $\pi\pi^*$ states depends on O-H bond lengths. Based on the experimental results, it appears that for most quinones, either $[Q]^*\cdots H_2O$ or a QH•–•OH biradical directly react with the probe compound rather than first dissociating to form free •OH.

The reduction in hTPA production by DPBQ and AQS in the presence of methane, though the significance is questionable, could mean that these molecules are capable of forming free •OH. Gan et al. (2008) showed that quinones substituted with electron acceptors, such as di-chloro and

tetra-chloro-1,4-benzoquinones, are capable of forming free •OH. The methoxy groups on DPBQ are electron-withdrawing in the meta position with a Hammett constant of 0.12 (Schwarzenbach, 2002) possibly favoring the dissociation of the QH•–•OH biradical through EDPT (Karsili et al., 2015). Sulfonate groups are also electron-withdrawing, with a Hammet constant estimated to be 0.38 for 2-aminobenzenesulfonic acid (Imaizumi et al., 2002), also supporting the potential dissociaton of the biradical. Another proposed mechanism for free •OH formation involves the reduction of O_2 by excited AQS (Loeff et al., 1983), but there has not been any experimental evidence for the formation of free •OH by AQS (Alegría et al., 1999; Garg et al., 2007). While it is possible that DPBQ and AQS form a small amount of free •OH, the small sulfur content (<0.60% of SRFA; Buckley et al., 2024) and lack of methoxy-containing structures found in DOM (Zark & Dittmar, 2018) imply that these compounds are only responsible for a small fraction of total hydroxylating species generated by DOM.

3.5.2 H_2O_2-dependent pathway of •OH production by quinones

Despite the observed lack of quenching by methane, quinones may produce free •OH through the H_2O_2-dependent pathway in the presence of an electron donor (Scheme 3.1a). The H_2O_2-dependent mechanism involves the transfer of an electron to a triplet state quinone ($^3Q^*$), and therefore this pathway is not feasible for isolated quinones. The antioxidant properties of DOM are well known (Aeschbacher et al., 2012, Walpen et al., 2018), mainly attributed to the phenolic moieties of DOM. Thus, in a natural system, electron transfer from a phenolic compound to $^3Q^*$ is a conceivable pathway to the formation of free •OH (Faust & Hoigne, 1987; Canonica et al., 1995; Canonica et al., 2000; Maurino et al., 2011; Garg et al., 2011; De Laurentis et al., 2013). Prior research has found that the photochemical production of H_2O_2 by DOM isolates is enhanced in the presence of phenols (Zhang et al., 2014). The authors suggested that the oxidation of phenols by

triplet state aromatic ketones leads to the formation of $HO_2^{\bullet}/O_2^{\bullet-}$ when phenoxy radical reacts with O_2, as has been demonstrated by others (Canonica et al., 1995; Canonica et al., 2000; Zhang et al., 2012; Zhang et al., 2014). Most quinones have even higher triplet state one-electron reduction potentials than aromatic ketones (McNeill & Canonica, 2016), supporting their ability to oxidize phenol. Further, the oxidation of phenol by $^3AQS^*$ has been shown to generate $HO_2^{\bullet}/O_2^{\bullet-}$ (Maurino et al. 2008)

Since there were no electron donors in the methane quenching experimental solutions, free $^{\bullet}OH$ formation through the H_2O_2-dependent pathway was not feasible for isolated quinones. However, the addition of up to 40 units mL^{-1} catalase, albeit at concentrations low enough to neglect direct $^{\bullet}OH$ quenching by catalase, caused a reduction in probe transformation for all model quinones (Figure A.8). It was hypothesized that this result is due to the multifaceted reactivity of catalase with RIs other than $^{\bullet}OH$, possibly $^3Q^*$. Previous studies have shown that electron-donating amino acids such as tryptophan, tyrosine, or methionine may quench triplet state quinones and aromatic ketones (Encinas et al., 1984; Janssen et al., 2014; Wu et al., 2023), thus it is conceivable that catalase undergoes electron transfer to $^3Q^*$. If the electron transfer path competes with the reaction between water and $^3Q^*$, any H_2O_2 produced through electron transfer from catalase is subsequently quenched by catalase, resulting in the decreased rate of transformation of the probe compound by $[Q]^{*}\cdots H_2O$ or $QH^{\bullet}-{}^{\bullet}OH$. Although it was outside the scope of this paper to evaluate the reactions between catalase and $^3Q^*$, this should be explored in future work.

To further assess the electron transfer to $^3Q^*$ which initiates $^{\bullet}OH$ formation through an H_2O_2-dependent pathway, $^{\bullet}OH$ formation from PBQ was assessed in the presence of phenol (PheOH). While maintaining a constant value of expected methane quenching (19.18%), the quenching of the rate of SA formation was assessed while the ratio of PheOH:PBQ was increased

(Figure 3.3). At all concentration ratios, the quenching of SA formation was within reasonable errror from the expected percent of methane quenching, suggesting the species responsible for the transformation of BA to SA was indeed free •OH. Also, the addition of catalase at 10 or 20 units mL^{-1} quenched the rate of SA formation to a greater extent in the solutions with greater phenol content. At 20 units mL^{-1}, the quenching of •OH directly by catalase was only 5.08% for all PheOH:PBQ ratios, which means catalase must quench a precursor to hydroxylating species, such as H_2O_2 or $^3Q^*$. Though it is possible that the higher quenching by catalase at higher PheOH:PBQ ratios is due to increased quenching of $^3Q^*$ by catalase, it is probable that mixtures with greater phenol:quinone ratios lead to greater production of H_2O_2.

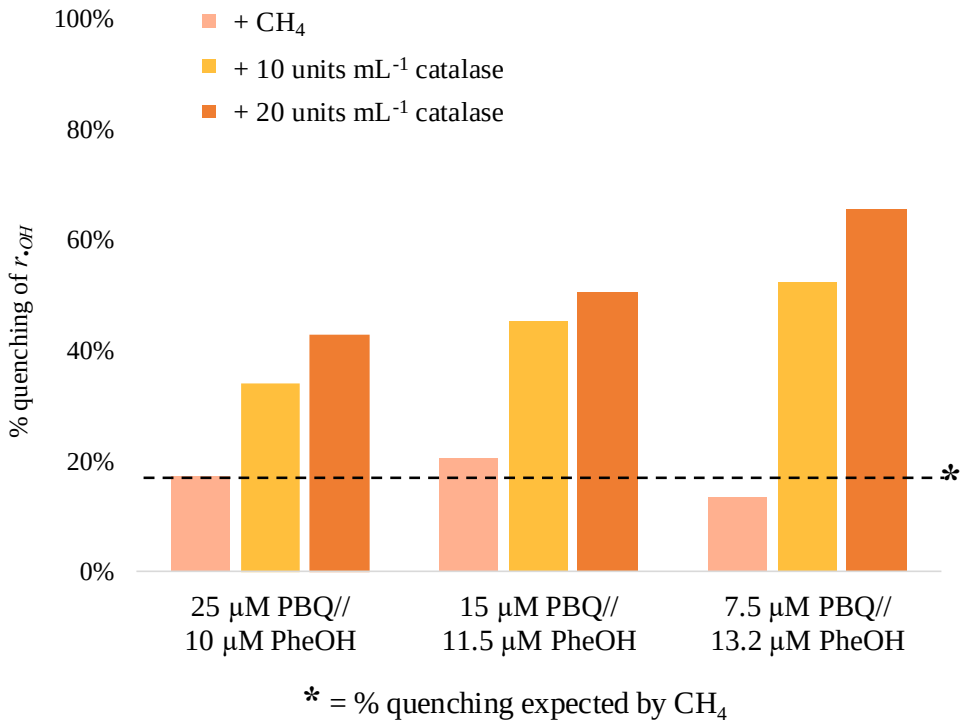

Figure 3.3 Percent of quenching of the rate of formation of salicylic acid (r_{SA}) by methane (pink), 10 units mL^{-1} catalase (yellow-orange), and 20 units mL^{-1} catalase (dark orange) in the presence of three different concentration ratios of p-benzoquinone (PBQ) and phenol (PheOH). Solutions were irradiated in a Rayonet merry-go-round reactor at 254 nm and r_{SA} was measured in triplicate for each concentration ratio.

Based on the electron donating capacity (EDC) and electron accepting capacity (EAC) of SRFA, it has been estimated that SRFA contains 14.0% and 3.62% w/w of phenols and quinones, respectively (Aeschbacher et al., 2012; Ritchie & Perdue, 2012; Buckley, et al., 2024), which is even higher than the PheOH:PBQ used in this work. It is thus conceivable that in DOM, the H_2O_2-dependent pathway leads to free •OH formed through electron transfer from phenolic to quinonoid moieties. Consequently, the respective concentrations of phenols and quinones should play a part in determining the rates and mechanisms of •OH formation in DOM.

3.5.3 •OH production by hydroxybenzoic acids

Based on methane quenching results from this study, the hydroxybenzoic acids chosen in this study indeed produce free •OH (Figure 3.2). The literature has hypthesized many potential mechanisms for free •OH by substituted phenols. One possible mechanism is •OH dissociation from excited hydroxybenzoic acids. Potential energy calculations support that •OH dissociation may occur when HBA is excited at 193 nm, but H dissociation is the major pathway (Yang et al. 2011; Vulpius et al., 2010). Yang et al. also found that •OH dissociation in subsituted phenols only occurs at the -OH group, not the -COOH group, and •OH dissociation does not occur for molecules that undergo intramolecular H-bonding, which may explain the uniqueness of HBA and DHBA to produce •OH. However, experimental work has yet to confirm that •OH dissociation is possible, especially at wavelengths relevant to environmental or engineered systems (>200 nm).

Another potential mechanism resulting in •OH formation is initiated by the photoionization of phenols. The photoionization of phenolic compounds generates hydrated electrons (Grossweiner et al., 1963; Robertson et al., 2023; Tyson & Verlet, 2019) which react quickly with dissolved oxygen (1.9×10^{10} M^{-1} s^{-1}, Buxton et al., 1988) to produce superoxide and subsequently H_2O_2. The photoionization of phenolic compounds also generates radical cations, to which water

has been hypothesized to undergo rapid nucleophilic addition and subsequent •OH-elimination (Sun et al., 2015). Others have suggested that rather than a phenoxy radical, hydrogen is abstracted from water by a triplet state quinoid enol tautomer through excited-state proton transfer (ESPT), supported by evidence that •OH formation by DHBA occurs only in water and not acetonitrile (Vulpius et al., 2010; Klíčová et al., 2012; Sun et al., 2015). Sun et al., (2015) also suggested that •OH production from DHBA is O_2-independent, which would imply no involvement of H_2O_2. Contrastingly, we found that the addition of 40 units mL^{-1} catalase quenched r_{SA} by 34.3% and 35.1% in the presence of HBA and DHBA, respectively (Figure A.8). These results suggest that the H_2O_2-dependent pathway contributes to approximately 35% percent of •OH formation through the photoionization of phenolic compounds and subsequent reduction of O_2. While further research is needed to clarify these mechanisms, the generation of •OH from phenolic compounds likely occurs through a combination of water- and H_2O_2-dependent pathways.

3.5.4 Relevance to natural aquatic systems

Understanding the mechanisms of hydroxylating species production from model sensitizers gives insight into complex the photochemical reactions of DOM in natural systems. In DOM, quinones and hydroxybenzoic acids exist within a mixture of carbonyls, phenols, carboxylic acids, aromatic species, and alicyclic moleules, thus it is presumable that mechanisms and rates of hydroxylating species production will depend on DOM concentration and composition. It was shown in this study that quionones may form •OH via an electron transfer in the presence of another quinone or electron donor. Therefore, for this pathway to occur, the concentration of electron donors must be high enough to outcompete reactions between a triplet state quinone and ground-state quinone, water, and O_2, or O_2-independent relaxation (Scheme 3.2). The contributions for each triplet state quinone deactivation pathway in Table 3.2 were estimated based on the average

of known rate constants of several quinones and previously reported quinone and phenol content in DOM (Text A.5). It is worth emphasizing that Table 3.2 only includes pathways beginning with triplet state quinones, thus free •OH may also be generated by other DOM chromophores through the generation of $O_2^{\bullet-}$/H_2O_2, oxidation of water/hydroxide, or photo-dissociation reactions (Table A.1). Nonetheless, Table 3.2 represents the upper limits of •OH-producing pathways, since other quinones in DOM do not have as high of hydroxylating species quantum yields compared to PBQ, MBQ, and AQS. The contribution of hydroxybenzoic acids to •OH production in DOM could not be estimated due to unknown deactivation rates for their triplet states. Mechanisms involving aromatic carbonyl compounds such as aromatic ketones and aldehydes may al[39]so contribute to •OH formation through the production of H_2O_2 (Anastasio et al., 1997; Zhang et al., 2012; Zhang et al., 2014), but these compounds likely contribute minimally to free •OH considering their low estimated content in DOM (<2.1% w/w of SRFA; Buckley et al., 2024), low triplet state one-electron reduction potentials relative to quinones (McNeill & Canonica, 2016), and the overall low contribution of the H_2O_2-dependent pathway (Cheng et al., 2025).

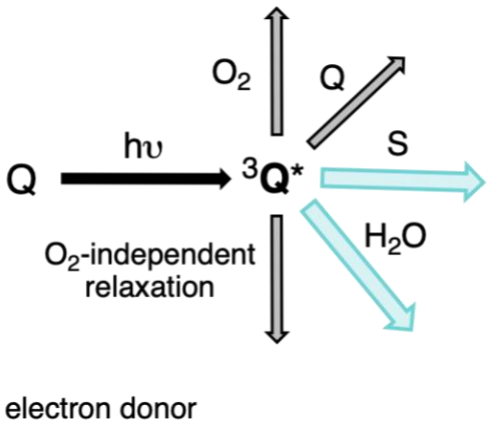

Scheme 3.2 Pathways for the deactivation of triplet state quinones in aqueous air-saturated conditions. Blue arrows represent pathways that may result in the formation of hydroxylating species, including •OH or a quinone-water exciplex ($[Q]^*\cdots H_2O$).

Table 3.2 Estimated contributions of pathways for the deactivation of triplet-state quinones at environmentally relevant DOM concentrations. Calculations for pathway contributions are outlined in Text A.5 with deactivation rates listed in Table A.4. The blue-shaded rows are pathways which lead to the formation of •OH or a quinone-water exciplex ($[Q]^{*}\cdots H_2O$).

Deactivation pathway	DOM concentration		
	2 $mg_C\ L^{-1}$	5 $mg_C\ L^{-1}$	10 $mg_C\ L^{-1}$
Electron transfer to S	2.5%	6.0%	8.7%
$[Q]^{*}\cdots H_2O$ formation	59.3%	57.2%	54.0%
Quenching by ground state quinone	0.6%	1.4%	2.6%
Energy transfer to O_2	34.8%	33.6%	31.7%
O_2-independent relaxation	3.4%	3.3%	3.1%

3.6 Limitations and future work

While this study provides novel insight to the mechanisms of •OH formation by model compounds of DOM, there are yet many challenges of studying short-lived species and the complexity of DOM. First, accurately measuring •OH is difficult due to the lack of selectivity of most probe compounds for •OH and unknown reaction rate constants between probe molecules and $[Q]^{*}\cdots H_2O$ or $QH^{\bullet}$–•OH. Future studies should focus on the reactivity of $[Q]^{*}\cdots H_2O$ and $QH^{\bullet}$–•OH, not only to determine their reactivity with probe compounds, but to assess the rates of hydroxylation of contaminants. While free •OH is non-selective and reacts at near diffusion-controlled rates, $[Q]^{*}\cdots H_2O$/$QH^{\bullet}$–•OH are more selective (demonstrated by their lower reactivity with methane) and greater in size, possibly attached to an even larger molecule or assembly of molecules (Norris et al., 2025). While the molecular weight of PBQ is 108.10 Da, the average molecular weight of DOM is between 500-1200 Da (Leenheer et al., 2001; Perdue & Ritchie, 2003; Stenson et al., 2003; McAdams et al., 2018), suggesting there is a wide range of size among quinones (and other sensitizers) in DOM. Also, several studies have shown the enhanced

production of reactive intermediates when measured by hydrophobic probe compounds, often attributed to a higher concentration of chromophores within water-deficient hydrophobic "pockets" of DOM (Latch & McNeill, 2006; Grandbois et al., 2008; Yan et al., 2021). This implies that the hydroxylation of contaminants not only depends on their reaction rates with $[Q]^{*}\cdots H_2O/QH^{\bullet}-{}^{\bullet}OH$, but on their accessibility to hydroxylating chromophores. The estimated the contributions of deactivation pathways in Table 3.2 are thus limited to the averages of reaction rates of the relatively small and freely dissolved model quinones that have been well-studied, and a more accurate estimation of DOM quinones requires known deactivation rates for a wider collection of quinones.

Next, the use of methane and catalase as quenchers for ${}^{\bullet}OH$ and H_2O_2 is not without limitations. Although methane is the only known molecule selective for ${}^{\bullet}OH$, its low aqueous solubility limits the concentrations of sensitizers and probes in solution. As demonstrated by Table 3.2, lowering the concentration of a model quinone alters its triplet state deactivation pathway, consequently impacting the rates and mechanisms of ${}^{\bullet}OH$ formation. It would be useful to identify more probe and quencher molecules that are selective for ${}^{\bullet}OH$ versus $[Q]^{*}\cdots H_2O/QH^{\bullet}-{}^{\bullet}OH$ so environmentally relevant concentrations of sensitizers may be used and accurate rates of ${}^{\bullet}OH$ formation be measured. Also, the use of catalase as an H_2O_2 should be cautioned due to its high reaction rate with ${}^{\bullet}OH$ and potential reactions with triplet states. Futher work is needed to identify a more selective quencher for H_2O_2 or clarify the reactivity between catalase and triplet states.

Future investiagtions should continue to focus on elucidating the pathways to ${}^{\bullet}OH$ and hydroxylating species formation in DOM from hydroxybenzoic acids and other derivatives of quinones and phenols. To our knowledge, there are only speculations of the mechanisms leading to ${}^{\bullet}OH$ formation by hydroxybenzoic acids, besides their formation of free ${}^{\bullet}OH$ and the

contribution of H_2O_2 determined herein. Understanding the mechanisms of $^{\bullet}OH$ formation by substituted phenols is of interest both due to the relatively high phenol content of DOM (14% w/w of SRFA; Buckley et al., 2024) and the impacts of O_2, water, and different substituents on phenol photoionization and $^{\bullet}OH$ formation (Feitelson et al., 1972; Vaughan & Blough, 1998; Gadosy et al., 1999; Zhang et al., 2012; Zhang et al., 2014; Sun et al., 2015; Wan et al., 2024). Recent work demonstrating heightened generation of $^{\bullet}OH$ from chlorinated DOM elicits further exploration regarding the impacts of oxidation processes on the photochemical formation of $^{\bullet}OH$ by DOM (Wan et al., 2024).

3.7 Environmental implications

The results of this work confirm prior speculations that quinones do not form free $^{\bullet}OH$ in isolation, but react with water to form a quinone-water exciplex or biradical which is capable of hydroxylating other molecules. Both this work and a recent study (Cheng et al., 2025) suggest that previous work has overestimated production of free $^{\bullet}OH$ and the contribution of the H_2O_2-dependent pathway in DOM because of the use of nonselective $^{\bullet}OH$ probes and the oversight of RI quenching by catalase. Accurately quantifying free $^{\bullet}OH$ and identifying its mechanisms of formation has critical implications for the predictions of contaminant fate in surface waters. The reactivity of a contaminant with $[Q]^{*}\cdots H_2O/QH^{\bullet}-{}^{\bullet}OH$ may be significantly lower than with free $^{\bullet}OH$, depending on its chemical structure and proximity to $[Q]^{*}\cdots H_2O/QH^{\bullet}-{}^{\bullet}OH$ in solution. Thus, estimating contaminant degradation rates based on a $[^{\bullet}OH]_{ss}$ that includes $[Q]^{*}\cdots H_2O/QH^{\bullet}-{}^{\bullet}OH$ may lead to underestimates of contaminant persistence. Next, understanding the mechanisms of $^{\bullet}OH$ generation by DOM is important to predicting the influence of DOM concentration and composition on its photoreactivity. This research demonstrated that role of electron transfer between phenols and quinones in the production of $O_2^{\bullet-}/H_2O_2$, although a small deactivation

pathway for triplet state quinones, will become more important in systems with high quinone and phenol contencentrations. From this work, it is apparent that the use of model sensitizers, and mixtures of model sensitizers, is necessary to understand the specific structures and intermolecular interactions involved in $^{\bullet}OH$ production by DOM. Identifying individual molecular entities responsible for the production of RIs and reactivity of DOM will continue to be important in the field of DOM research because of how DOM chemistry is altered through processes such as photomineralization and water/wastewater treatment, and consequently, how DOM chemistry impacts the cycling of nutrients and fate of contaminants in the environment.

3.8 Acknowledgements

This work was supported by the U.S. Army Research Office grant W911NF-20-1-0040.

4. Photochemical Degradation of Saxitoxins in Surface Waters

This chapter has been published as **Norris, K. E.**; Kurtz, T.; Wang, S.; Zeng, T.; Leresche, F.; Rosario-Ortiz, F. L. Photochemical Degradation of Saxitoxins in Surface Waters. *ACS EST Water* **2024**, *4* (2), 346–354. https://doi.org/10.1021/acsestwater.3c00281.

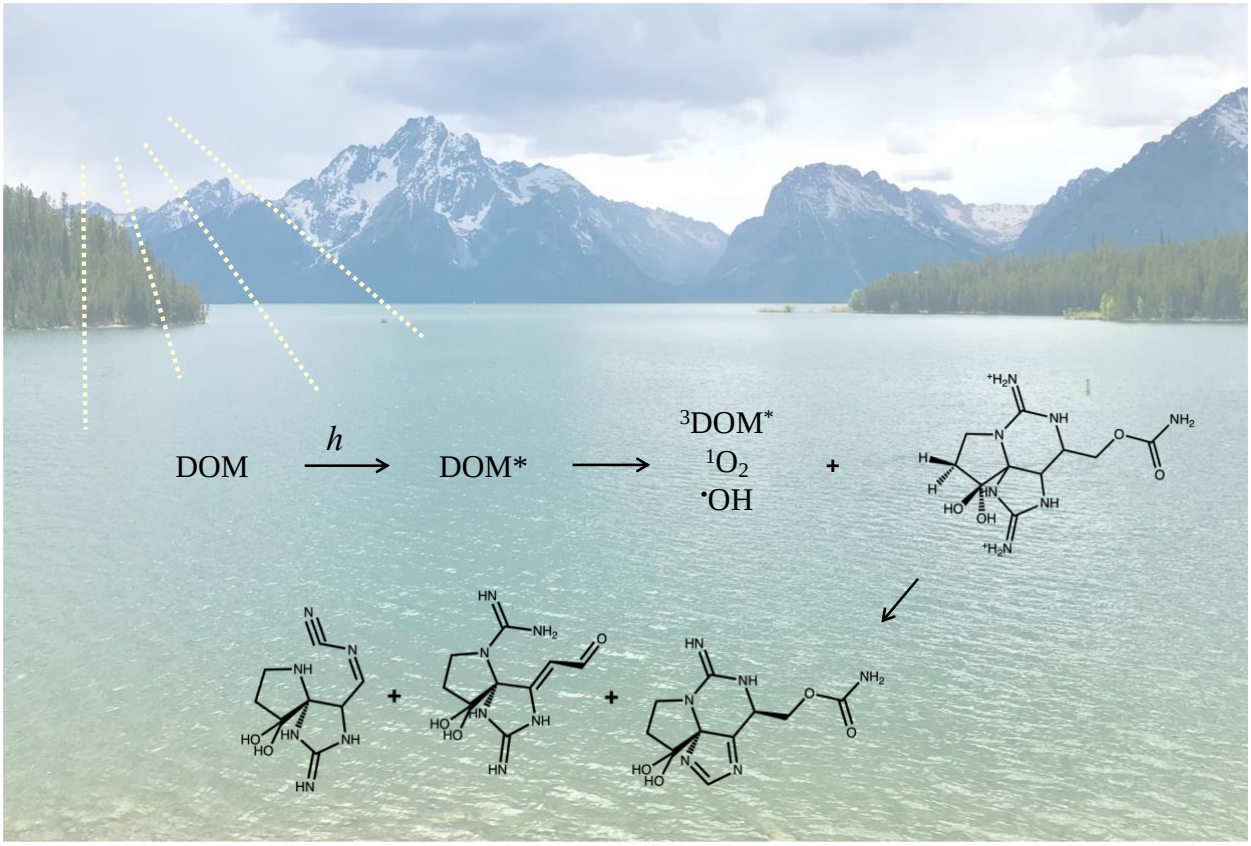

Figure 4.1 Graphical abstract for Photochemical Degradation of Saxitoxins in Surface Waters.

4.1 Abstract

Photochemical degradation has been shown to be a significant pathway in the environmental fate of many cyanotoxins, compounds produced by harmful cyanobacteria. However, there has been a lack of research on the photochemical fate of saxitoxins. This project evaluated the direct and sensitized photodegradation of three saxitoxin analogues including saxitoxin (STX), gonyautoxin-2 and -3 (GTX 2/3), and n-sulfocarbamoylgonyautoxin-1 and -2 (C1/2). Irradiation of STX and analogues in the presence or absence of dissolved organic matter

(DOM) revealed that none of the toxins undergo direct photolysis at pH 6 or 8, and only STX and GTX 2/3 undergo sensitized photolysis at pH 8. Sensitized photolysis half-lives ranged from 1 to 10 hours for STX and GTX 2/3. The contribution of reactive intermediates including singlet oxygen ($^1O_2$), triplet-state dissolved organic matter ($^3DOM^*$), and hydroxyl radicals ($^{\bullet}OH$) was assessed, with $^3DOM^*$ accounting for the majority of STX and GTX 2/3 degradation. Additionally, three transformation product candidates were identified for the photolysis of STX, and an electron-transfer mechanism was proposed. The kinetics, mechanism, and products of saxitoxin phototransformation are essential to understanding the persistence of these toxins in surface waters and assessing the impacts of harmful algal blooms.

4.2 Synopsis

The photochemical fate of three saxitoxin congeners is dominated by electron-transfer reactions with triplet-state DOM, showing the important role of DOM in the lingering impacts of HABs on surface waters.

4.3 Introduction

Cyanobacterial blooms are occurring more frequently in water bodies throughout the globe, largely due to anthropogenic nutrient input and the effects of the changing climate (O'Neil et al., 2012; Paerl & Paul, 2012; Gehringer & Wannicke, 2014). These blooms have become a public health concern due to the production of cyanotoxins, which include a wide variety of compounds such as neurotoxins (anatoxins and saxitoxins) and hepatotoxins (microcystins, nodularins, and cylindrospermopsins) (Carmichael, 1992; Carmichael, 1997; Carmichael et al., 2001). Exposure to cyanotoxins through drinking water, recreation, and shellfish has caused adverse health effects in humans and other mammals (Chorus & Welker, 2021). Therefore, understanding the persistence and fate of cyanotoxins is vital to evaluating the risks associated with cyanobacterial blooms.

While saxitoxins are the most potent class of cyanotoxins, their environmental fate has been given little attention (Christensen & Khan, 2020). Saxitoxins are a group of neurotoxic alkaloids with oral LD_{50} values ranging from 1.26-8.68 μmol/kg (Wiese et al., 2010; Munday et al., 2013). These compounds are produced by marine dinoflagellates as well as multiple genera of cyanobacteria, including *Anabaena*, *Cylindrospermopsis*, and *Lyngbya* (Wiese et al., 2010). There are 57 known analogues of saxitoxins (Wiese et al., 2010), and those most frequently mentioned in the literature include saxitoxin (STX), gonyautoxin (GTX), and n-sulfocarbamoyl-gonyautoxin (C-toxin) (Figure 4.2). STX and analogues have been detected in natural freshwaters across Argentina, Australia, Brazil, Denmark, Russia, and the United States with dissolved concentrations up to 193 μg/L (Christensen & Khan, 2020).

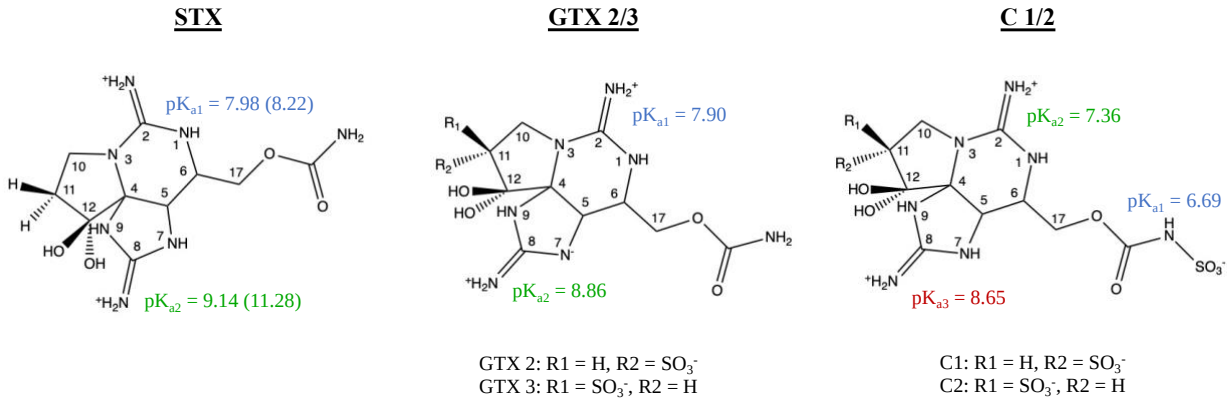

Figure 4.2 The structures of saxitoxin (STX), gonyautoxin-2 & 3 (GTX 2/3), and n-sulfocarbamoyl gonyautoxin-1 & 2 (C 1/2) and their predicted pK_a values. Experimental pK_as for STX are noted in parentheses (Rogers & Rapoport, 1980). Predicted pK_a values were determined using the Chemicalize software by Chemaxon (Swain, 2012). The pK_as of the sulfonic acid groups are <0.

The major concern regarding the fate of saxitoxins is that they have been shown to remain stable when dissolved in environmentally relevant conditions. Previous research has demonstrated that saxitoxins persisted in river and irrigation drain water for 90 days (Jones & Negri, 1997), natural surface waters for 1-2 months (Batoréu et al., 2005), and over 30 days in culture (Castro et

al., 2004). Interestingly, the transformations observed by Jones & Negri (1997) showed an increase in toxicity during the first 2-3 weeks due to slow hydrolysis of C 1/2 toxins to more potent analogues. Saxitoxins can also adsorb to clays and sediments (Burns et al., 2009), which could either act as a sink for the toxins or enhance their persistence through re-equilibration with the water column. While past research has suggested that saxitoxins are not susceptible to biodegradation (Jones & Negri, 1997; Ho et al., 2012a; Ho et al., 2012b; Tang et al., 2012), recent work has identified bacterial strains capable of degrading the toxins. A new study found that saxitoxins were degraded into nontoxic products by the SSZ01 strain of *Bacillus* flexus (Mohamed et al., 2023). Another recent study demonstrated that bacterioplankton from a Denmark lake reduced concentrations of STX and analogues by 42-59% (Jørgensen et al., 2022). Jørgensen and authors also showed that exposure to sunlight inhibited biosynthesis of STX, enhanced the release of intracellular STX from cells, and decreased STX concentrations in 0.2 µm-filtered lake water (Jørgensen et al., 2022). However, further analyses are necessary to quantify the rates and mechanisms of photodegradation for STX and analogues.

Photodegradation plays a role in the fate of many cyanotoxins (Kurtz et al., 2021), primarily via sensitized pathways. Sensitized photolysis may occur through reactions with a variety of reactive intermediates (RIs) including hydroxyl radicals ($^{\bullet}OH$), singlet-state oxygen ($^1O_2$), as well as excited triplet states of DOM ($^3DOM^*$). In a recent review, Kurtz et al. (2022) found direct photolysis to only be significant for anatoxin-a in natural systems and sensitized photolysis to be significant in the photodegradation of anatoxins, cylindrospermopsin, domoic acid, and microcystins. Several cyanotoxins undergo $^{\bullet}OH$-addition or H-abstraction reactions with second order rate constants ranging from 2.54×10^9 to 2.79×10^{10} M^{-1} s^{-1} (Park et al., 2019; He et al., 2015; Liu et al., 2016). Other published second order rate constants include 5.1×10^5 M^{-1} s^{-1} for a

$^1O_2$- ene/Diels alder reaction with domoic acid (Jaramillo et al., 2020) and 3.8×10^8 M^{-1} s^{-1} for $^3DOM^*$ energy transfer with domoic acid (Jin et al., 2018). These rate constants are helpful in understanding the kinetics and mechanisms of phototransformation for specific cyanotoxins, therefore, this work aims to fill the gap in knowledge regarding saxitoxins.

This work focused on the photodegradation of the analogues STX, GTX 2/3, and C 1/2 due to their prevalence in literature and commercial availability. The objectives of this research were to quantify the overall rates of photolysis, determine the contributions of direct and sensitized photolysis, and evaluate the contributions of RIs including $^3DOM^*$, $^1O_2$, and $^\bullet OH$. Other RIs, such as superoxide and carbonate radical anions, were not considered in this study since they are weak oxidants and have higher selectivity towards organic compounds, respectively. Additionally, the transformation products (TPs) resulting from the sensitized photolysis of STX were examined using high-resolution mass spectrometry (HRMS). Knowledge of the transformation products of STX and its reactivity with RIs was synthesized to outline a potential mechanism for sensitized photodegradation.

4.4 Materials and Methods

4.4.1 Chemicals and Solutions

A complete list of commercially available chemicals used in this work is found in Table B.1. All chemicals were used as received, with exception to *p*-nitroanisole, which was recrystallized from ethanol before used in the actinometry solution. Cyanotoxin certified calibration solutions were obtained from National Research Council Canada. GTX2/3 and C1/2 were obtained as combined mixtures (of GTX2 + GTX3, and C 1+C 2 respectively), the reported concentration in the manuscript refers to the sum of GTX2 + GTX3 (GTX2/3) or C 1+C 2 (C1/2) respectively. STX (61.4 μM) and GTX2/3 (146.1 μM, combined) standards arrived as solutions

dissolved in 0.5 mM hydrochloric acid (HCl). C1/2 (121.2 μM, combined) arrived as a solution dissolved in 20 μM acetic acid. Experimental solutions containing the cyanotoxin standards were made fresh daily and were stored at 4 °C in silanized glass vials, since saxitoxins adsorb to usual glass. All solutions were prepared in deionized water (18.2 mΩ cm, 5 ppb total organic carbon (TOC)) produced by a Sartorius arium® pro DI dispenser. The pH of surface waters typically ranges from 6.5-8.5, though during a cyanobacterial bloom pH may rise to 8-10 (Fang et al., 2018; Natumi et al., 2021). Thus, solutions for method development and initial experiments were performed at pH 6 and 8 (±0.1) and subsequent experiments at pH 8 (±0.1). pH was maintained by adding 10 mM of either pH 6 or 8 phosphate buffers, which were prepared by dissolving monosodium phosphate and disodium phosphate in DI water and adjusted with HCl or sodium hydroxide (NaOH).

Two DOM isolates from the International Humic Substances Society (St. Paul, Minnesota) were selected as representative of bodies of water where HABs may occur: Nordic Lake fulvic acid (NLFA, 1R105F) and Suwannee River fulvic acid (SRFA, 1S101F). The characteristics of these fulvic acids can be found in Table B.2 and their UV spectra are shown in Figure B.1. UV−vis spectra were measured on a Cary 100 Bio UV−visible spectrophotometer using a 1 cm path length quartz cuvette and dissolved organic carbon (DOC) was measured on a Sievers TOC analyzer model M5310C. DOM stock solutions (~50 $mg_C\ L^{-1}$) in 10 mM phosphate buffer (pH 6.0 and 8.0 ± 0.1) were prepared. After approximately 24 h of stirring, the solutions were filtered with ultrapure water prewashed Whatman 0.45 μm poly(ether sulfone) filters. pH was measured using a calibrated Thermo Scientific Orion Versa Star Pro Advanced Electrochemistry meter with an Orion ROSS Ultra pH/ATC triode (model 8157BNUMD).

4.4.2 Photochemical Experiments

Dark control, direct, and sensitized photolysis experiments and RI contribution determination were performed at the University of Colorado (Boulder, CO). Irradiation experiments were conducted in triplicate using an Oriel Sol1A solar simulator equipped with a 1000 W xenon lamp, which was operated at 800 W. The spectral distribution of the solar simulator lamp was measured using an Ocean Optics USB2000 spectrometer (Figure B.2) while the daily irradiance was measured using actinometry. Solutions spiked with 200-1000 nM STX or analogues were irradiated in 4 mL plastic cuvettes lying at an angle of approximately 30° from the horizontal. Absorbance and transmittance spectra of cuvettes are presented in Figure B.3. A recirculating water bath was used to maintain a temperature of 20±1 °C. Dark control experiments utilized the same vials as other experiments and were wrapped in foil to prevent the solutions from receiving any light exposure. Before high-performance liquid chromatography (HPLC) analysis, toxin samples were processed using a pre-column fluorescence derivatization as outlined in Text B.2. The toxin oxidation products are shown in Figure B.4. After derivatization, samples were allowed to sit at room temperature in the dark for 24±2 hours before undergoing HPLC analysis. Concentrations of the toxins, probe compounds, and actinometer were measured in triplicate or quadruplicate on an Agilent 1200 series HPLC system equipped with an Agilent Eclipse Plus C-18 5 μm particle size reverse-phase column using the isocratic methods detailed in Table B.3. Liquid chromatography-mass spectrometry (LCMS) analysis was performed at the Central Analytical Mass Spectrometry Facility of the University of Colorado to confirm the results of sensitized photolysis experiments. A Waters Synapt G2 high-definition mass spectrometer was used in combination with a Waters Acquity nano-UPLC equipped with a SeQuant ZIC-HILIC column; methods detailed in Text B.1.

A *p*-nitroanisole (PNA)/pyridine actinometer (10 μM PNA, 5 mM pyridine) was used to determine the daily photon irradiance of the solar simulator (Text B.3). The PNA quantum yield at this pyridine concentration is 1.74×10^{-3} (Laszakovits et al., 2017). For the solar simulator, the average PNA depletion rate constant was 1.56×10^{-4} s^{-1} and the average photon fluence rate in the 290-400 nm spectrum was found to be 2.85×10^{-4} mol m^{-2} s^{-1}. This photon fluence rate is compatible with a summer sunny day, noon photon fluence calculated for Boulder, CO in the 290-400 nm spectrum, 3.07×10^{-4} mol m^{-2} s^{-1} (Leresche et al., 2021). Observed rate constants were normalized according to the photon fluence rate at the time of each experiment over the average overall photon fluence.

4.4.3 Transformation Products

Identification of toxin transformation products (TPs) was performed at Syracuse University (Syracuse, New York) using liquid chromatography-high-resolution mass spectrometry (LC-HRMS). STX solutions (prepared by spiking 200 nM of STX into pH 8.3 ammonium formate amended with 50 μM of 2-acetonaphthone (2-AN)) were irradiated in septum-sealed quartz test tubes (held at ~30° from the horizontal) inside an Atlas Suntest XLS+(II) solar simulator equipped with a 1700 W xenon arc lamp and a daylight glass 300 nm UV filter. Foil-wrapped STX dark controls (prepared by spiking 200 nM of STX into pH 8.3 ammonium formate) and 2-AN controls (prepared by spiking 50 μM of 2-AN into pH 8.3 ammonium formate) were irradiated in parallel to monitor any nonphotochemical transformation of STX and any formation of products from 2-AN, respectively. Throughout the irradiation experiments, the lamp irradiance was maintained at 63 W/m^2 between 300 and 400 nm, and the test chamber temperature was controlled at 25±1 °C with an Atlas SunCool chiller. *p*-Nitroanisole/pyridine actinometer solutions were irradiated alongside each set of samples to monitor the incident light intensity. Sample aliquots were taken

at predetermined time intervals (i.e., 0, 1, 2, 3, 5, 7, 9, and 11 h) and stored in amber autosampler vials for TP screening using LC-HRMS.

Samples and controls were analyzed by a Thermo Scientific TriPlus RSH autosampler and liquid handling system with a Vanquish Horizon ultra-high-performance liquid chromatograph and an Orbitrap Exploris 240 quadrupole-Orbitrap mass spectrometer equipped with an OptaMax NG heated electrospray ionization probe. For chromatographic separation, 20 µL of samples were injected onto an Accucore 150 Amide HILIC column (150 × 2.1 mm, 2.6 µm; preceded with a 10 × 2.1 mm guard cartridge) running water and acetonitrile (both acidified with 0.1% v/v formic acid) as the mobile phases at a flow rate of 200 µL/min and a column temperature of 35 °C. Full scan mass spectra were acquired from 100 to 1,000 Da with a mass resolution of 120,000 at *m/z* 200 with an intensity threshold of 10^5 and a mass tolerance of 5 ppm. Full scan triggered data-dependent tandem mass spectra were acquired with a mass resolution of 15,000 at *m/z* 200 with an *m/z* isolation window of 1 using higher-energy collisional dissociation across five normalized collision energies (i.e., 15%, 30%, 45%, 60%, and 75%).

4.4.4 APEX predictions

APEX (Aqueous Photochemistry of Environmentally occurring Xenobiotics) is a code that predicts the phototransformation kinetics of substrates with respect to various environmental conditions[66]. The code was applied to estimate the half-life of STX and fractions of RIs reacting with STX for a [DOC] between 0.1-10 mg_C/L and depth of 1cm. Input parameters included the experimentally determined second-order rate constants between STX and DOM and average environmental water quality parameters (Table B.9). Since the steady-state concentrations of $^1O_2$ and $^\bullet OH$ estimated by APEX were much lower than the experimental steady-state concentrations, the quantum yields of $^1O_2$ and $^\bullet OH$ produced by DOM were adjusted in APEX so the model agreed

with a $[^1O_2]_{ss}$ of 3.47×10^{-13} and $[^3DOM^*]_{ss}$ of 5.78×10^{-13} at a depth of 1 cm and 5 mg_C/L DOM, assuming $[DOC] \propto [^3DOM^*]_{ss}$ at near-surface. APEX half-lives were estimated in terms of Summer Sunny Days (SSD), corresponding to 10 hours of 22 W m^{-2} irradiance on a fair-weather 15 of July at 45N latitude.

4.5 Results

4.5.1 Direct and Sensitized Photolysis

Dark control and direct photolysis experiments were performed with each saxitoxin analogue at pH 6 and 8 (±0.1) to evaluate degradation due to hydrolysis or direct photolysis. No significant amount of degradation was detected in either experiment (Figure B.5). The absence of a direct photolysis pathway was anticipated given that neither STX, GTX2/3, nor C1/2 absorb light in the solar spectrum according to their predicted UV-vis absorption spectra (Figure B.6).

A series of experiments were performed with each toxin at pH 6 and 8 (±0.1) in the presence of DOM to assess degradation due to sensitized photolysis. None of the three analogues underwent sensitized photolysis at pH 6, and C1/2 was not susceptible to sensitized photodegradation at either pH (Figure B.5). At pH 8, STX and GTX2/3 both underwent photolysis in the presence of either 5 $mg_C\ L^{-1}$ (0.416 [48–50]$mM_C\ L^{-1}$) SRFA or NLFA (Figure 4.3) following first-order kinetics. Both toxins displayed a higher degradation rate in the presence of NLFA compared with SRFA (Table 4.1). [48–50]It is important to note the amount of uncertainty in the rate constant for GTX 2/3 in the presence of SRFA, but since GTX 2/3 showed unquestionable degradation in the presence of NLFA, it is probable that GTX 2/3 undergoes photolysis in the presence of SRFA as well.

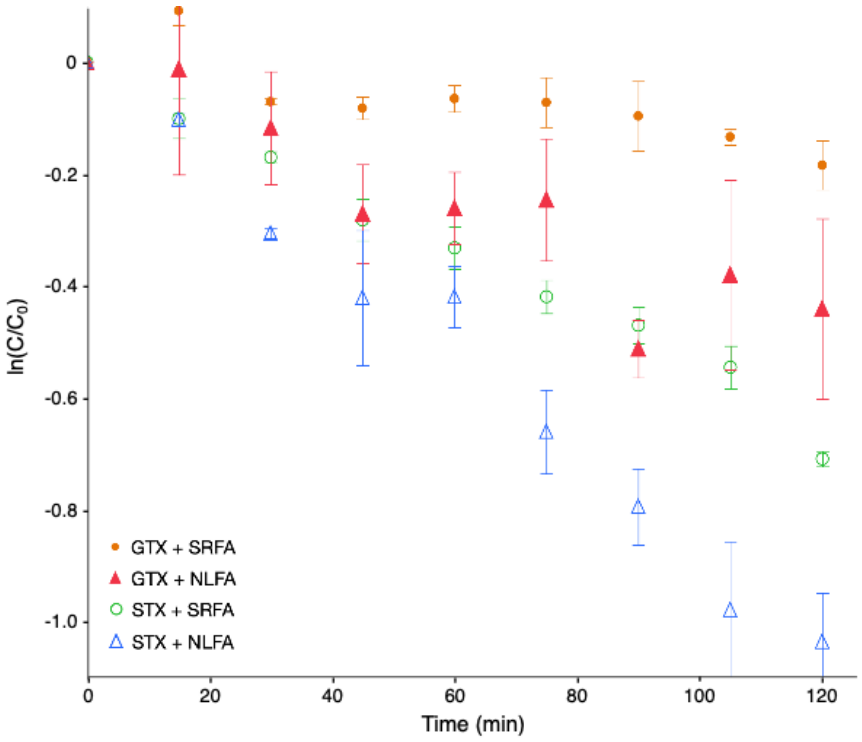

Figure 4.3 Indirect photolysis of saxitoxin (STX) and gonyautoxin 2 and 3 (GTX 2/3) at pH 8. Experimental solutions contained either 200 nM STX or 300 nM GTX2/3, 10 mM phosphate buffer, and 5 $mg_C L^{-1}$ Suwannee River or Nordic Lake fulvic acid (SRFA or NLFA). Points are the average of replicate experiments, with error bars representing standard error (n=3).

Table 4.1 The observed pseudo first-order rate constants (k_{STX}^{obs}) for saxitoxin (STX) and gonyautoxin 2 and 3 (GTX 2/3) in the presence of 5 $mg_C L^{-1}$ Suwannee River or Nordic Lake fulvic acid (SRFA or NLFA respectively), normalized to the average photon fluence rate. Experimental solutions are described in Figure 4.3; 95% confidence levels are indicated in parentheses.

Toxin	DOM Isolate	k_{STX}^{obs} ($\times 10^{-3}$ min^{-1})	Half-life (min)	p-value
STX	SRFA	5.27 (± 0.28)	132 (± 7)	<0.0001
	NLFA	8.40 (± 0.52)	83 (± 5)	<0.0001
GTX2/3	SRFA	1.18 (± 0.48)	590 (± 240)	0.00043
	NLFA	4.03 (± 0.78)	172 (± 33)	<0.0001

4.5.2 Contribution of reactive species

The contributions of $^{\bullet}OH$ and $^1O_2$ to saxitoxin phototransformation were determined using Equation 4.1, where f_{RI} is the toxin fraction reacting with $^{\bullet}OH$ or $^1O_2$, k_{STX}^{RI} is the second-order rate constant between the toxin and $^{\bullet}OH$ or $^1O_2$, $[RI]_{ss}$ is the steady-state concentration of $^{\bullet}OH$ or

$^1O_2$, k_{STX}^{obs} is the pseudo first-order rate constant between the toxin and DOM (Table 4.1), and k'^{RI}_{STX} is the pseudo first-order rate constant between $^{\bullet}OH$ or $^1O_2$ and the toxin.

$$f_{RI} = \frac{k_{STX}^{RI}[RI]_{ss}}{k_{STX}^{obs}} = \frac{k'^{RI}_{STX}}{k_{STX}^{obs}} \quad (4.1)$$

To examine the role of $^{\bullet}OH$ in the toxins' photodegradation, isopropyl alcohol (IPA) and tert-butyl alcohol (TBA) were added as $^{\bullet}OH$ quenchers. In most cases, the observed rate constant between STX or GTX 2/3 and DOM was not significantly different from the observed rate constants with the addition of IPA or TBA (Table B.4). However, the addition of IPA for STX in the presence of NLFA and GTX 2/3 in the presence of SRFA, unexpectedly increased the observed rate constant. It has previously been suggested that IPA may increase photodegradation rates, with the non-steroidal anti-inflammatory drug diclofenac also exhibiting more rapid photodegradation in the presence of IPA (Packer et al., 2003). The authors of that study suggest that this may be due to IPA forming other radical species (such as superoxide or hydroperoxyl radicals) or photoreduction occurring with IPA serving as a proton donor. This phenomenon, combined with the lack of difference between observed rate constants in the other IPA experiments and both TBA experiments, suggests that the overall contribution of $^{\bullet}OH$ toward the degradation of STX and GTX 2/3 is small.

Thus, the contribution of $^{\bullet}OH$ was determined by finding the second-order rate constants between the toxins and $^{\bullet}OH$ ($k_{STX}^{\bullet OH}$) and measuring the hydroxyl radical steady-state concentrations ($[^{\bullet}OH]_{ss}$) during the experiments. $k_{STX}^{\bullet OH}$ values (listed in Table 4.2) were found for STX and GTX 2/3 using competition kinetics with *p*-chlorobenzoic acid (pCBA), an $^{\bullet}OH$ probe, the method for which is described in Text B.4. $[^{\bullet}OH]_{ss}$ was determined using Equation 4.2, where $r_{^{\bullet}OH}$ is the rate of $^{\bullet}OH$ production by DOM and $k_{DOM}^{\bullet OH}$ is the rate constant between $^{\bullet}OH$ and each DOM isolate.

$[^{\bullet}OH]_{ss}$ was found to be 2.93×10^{-16} M and 5.29×10^{-16} M in the presence of SRFA and NLFA, respectively.

$$[^{\bullet}OH]_{ss} = \frac{r_{^{\bullet}OH}}{k_{DOM}^{^{\bullet}OH}[DOM] + k_{STX}^{^{\bullet}OH}[STX]} \quad (4.2)$$

$r_{^{\bullet}OH}$ was determined using benzoic acid (BA) as a probe during the irradiation of DOM and measuring the production of salicylic acid (SA) on HPLC. The rate of $^{\bullet}$OH production by DOM (Equation 4.3) was equivalent to the rate of SA production (r_{SA}) divided by the yield of SA production ($yield_{SA}$) in Equation 4.4, which has been measured to be 15.5% (Qian et al., 2001).

$$r_{^{\bullet}OH} = \frac{r_{SA}}{yield_{SA}} \quad (4.3)$$

$$BA + {}^{\bullet}OH \rightarrow SA \quad (4.4)$$

$k_{DOM}^{^{\bullet}OH}$ has previously been measured for SRFA (Westerhoff et al., 2007; McKay et al., 2011) but was measured for NLFA ($k_{NLFA}^{^{\bullet}OH}$ = 2.98×10^{8} $M_C^{-1}s^{-1}$) during this study using competition kinetics with pCBA (Text B.5). The measured $k_{NLFA}^{^{\bullet}OH}$ is comparable to the reported values of other fulvic acids, 2.06×10^{8} and 6.90×10^{8} $M_C^{-1}s^{-1}$ for SRFA and Pony Lake fulvic acid, respectively (McKay et al., 2011). $f_{^{\bullet}OH}$ was calculated using Equation 4.1 for STX and GTX 2/3 (Table 4.2).

The contribution of singlet oxygen to the photodegradation of STX and GTX 2/3 was quantified through a series of competition kinetics experiments using furfuryl alcohol (FFA) as a $^1O_2$ probe and rose bengal (RB, Figure B.7) as a $^1O_2$ photosensitizer. RB has a singlet oxygen quantum yield (φ_Δ) of 0.76 in water (Wilkinson et al., 1993). To account for the direct photodegradation of RB, the procedure outlined in Text B.6 was used. The $^1O_2$ steady state concentration, $[^1O_2]_{ss}$, was determined using Equation 4.5 by measuring the transformation of FFA in the presence of SRFA, NLFA, and RB solutions.

$$[^1O_2]_{ss} = \frac{k'^{^1O_2}_{FFA}}{k^{^1O_2}_{FFA}} \quad (4.5)$$

$k'^{^1O_2}_{FFA}$ is the pseudo-first-order transformation rate constant of FFA and $k^{^1O_2}_{FFA}$ is the second-order rate constant for the reaction between $^1O_2$ and FFA (1.00×10^8 M^{-1} s^{-1})[38]. $[^1O_2]_{ss}$ and $k'^{^1O_2}_{FFA}$ values are listed in Table B.5, with associated plots in Figure B.8. The $[^1O_2]_{ss}$ values agree with previously reported values for $[^1O_2]_{ss}$ in the presence of SRFA and Pony Lake fulvic acid (Leresche et al., 2019). RB-sensitized photodegradation experiments showed that STX is susceptible to $^1O_2$ mediated photodegradation, while GTX2/3 is not (Figure B.9). The pseudo-first order rate constant for the phototransformation of STX in the presence of RB ($k'^{^1O_2(RB)}_{STX}$) was found to be 4.38×10^{-3} s^{-1}. Dividing $k'^{^1O_2(RB)}_{STX}$ by $[^1O_2]_{ss}^{(RB)}$ yielded a bimolecular rate constant between STX and $^1O_2$, $k^{^1O_2}_{STX}$, of 1.27×10^7 $M^{-1}s^{-1}$. The measured $k^{^1O_2}_{STX}$ is comparable to the rate constants measured for the $^1O_2$-mediated oxidation of several amino acids and cyanopeptides (10^6-10^8 $M^{-1}s^{-1}$) (Natumi et al., 2021; Di Mascio et al., 2019). It is assumed that all photodegradation observed during these experiments is attributable to $^1O_2$. RB can also form a triplet state ($^3RB^{2-}$) which may degrade compounds through energy or electron transfer pathways (Lambert et al., 1997); however, since GTX2/3 was shown to degrade in the presence of other triplet state RIs (e.g., $^3DOM^*$) through possible electron transfer pathways, but did not degrade in the presence of $^3RB^{2-}$, it is assumed that $^3RB^{2-}$ is also not contributing to the degradation of STX. $k'^{^1O_2(SRFA)}_{STX}$ and $k'^{^1O_2(NLFA)}_{STX}$ were found by taking the product of $k^{^1O_2}_{STX}$ and either $[^1O_2]_{ss}^{(SRFA)}$ or $[^1O_2]_{ss}^{(NLFA)}$, and the fraction of STX's overall photodegradation attributed to singlet oxygen, $f_{^1O_2}$, was calculated to be 5.56% and 5.21% for STX in the presence of SRFA and NLFA, respectively.

The contribution of $^3DOM^*$ to the sensitized photolysis of STX and GTX2/3 was calculated as the difference between the overall first-order rate constants and the contributions of $^1O_2$ and $^{\bullet}OH$ (4. 6). The fraction of STX and GTX 2/3 reacting with $^3DOM^*$ ($f_{^3DOM^*}$) was determined by assuming the overall rate between STX or GTX 2/3 and DOM is the sum of its reaction rates with each RI (Equation 4.6). $f_{^3DOM^*}$ values are listed in Table 4.2.

$$k'_{STX}^{^3DOM^*} = k_{STX}^{obs} - k'_{STX}^{^1O_2} - k'_{STX}^{^{\bullet}OH} \quad (4.6)$$

Table 4.2 Second-order rate constants for the reaction between $^{\bullet}OH$ and the toxins ($k_{STX}^{^{\bullet}OH}$) and the fractions of STX and GTX 2/3 reacting with $^{\bullet}OH$ ($f_{^{\bullet}OH}$), $^1O_2$ ($f_{^1O_2}$), and [$^3DOM^*$] ($f_{^3DOM^*}$) in the presence of Suwanee River fulvic acid (SRFA) or Nordic Lake fulvic acid (NLFA). 95% confidence intervals are indicated in parentheses.

Toxin	$k_{STX}^{^{\bullet}OH}$**(×10^8 M^{-1}s^{-1})**	**DOM Isolate**	$f_{^{\bullet}OH}$	$f_{^1O_2}$	$f_{^3DOM^*}$
STX	7.47 (± 0.94)	SRFA	0.24%	5.56%	94.20%
		NLFA	0.27%	5.21%	94.52%
GTX 2/3	6.26 (± 1.27)	SRFA	0.79%	-	99.21%
		NLFA	0.49%	-	99.51%

Additionally, a model triplet photosensitizer, 2-acetonaphthone (2-AN), which is thought to be a reasonable surrogate for DOM (Wu et al., 2021), was used to model saxitoxin degradation via $^3DOM^*$ in a simplified solution for HRMS analysis. Both STX and GTX 2/3 showed degradation in the presence of 2-AN with their rate constants listed in Table B.6. 2-AN has a quantum yield for intersystem crossing of 0.84 (Canonica et al., 1995) and a triplet energy of ~248 kJ mol^{-1} (Herkstroeter et al., 1964) which falls squarely in the proposed range of proposed $^3DOM^*$ triplet energies (McNeill & Canonica, 2016; Zepp et al., 1985)). One important consideration is that 2-AN has been shown to undergo self-sensitization (Wu et al., 2021), with a direct photolysis rate of 1.31 h^{-1}. However, HRMS measurements showed that the concentration of 2-AN only decreased by 3% during the first three hours of irradiation before undergoing self-sensitization,

thus its degradation had a negligible impact on the transformation of the toxins (Figure B.10). It is also important to note that 2-AN is known to produce $^1O_2$ with a reported quantum yield of 0.13 (Zhao et al., 2020). The fraction of $^1O_2$ contributing to the toxins' degradation in the presence of 2-AN was determined to be 14.8% and 0% for STX and GTX 2/3, respectively (see Text B.7). Although the contribution of $^1O_2$ to STX's degradation was slightly higher in the presence of 2-AN compared to the two DOM isolates, it was still assumed that the major transformation products (TPs) resulted from reactions with ^{3}2-AN*.

It has been shown that DOM antioxidant moieties can inhibit the phototransformation of some contaminants by reducing reaction intermediates (Wenk & Canonica, 2012; Leresche et al., 2016). To determine whether such an inhibition effect is present, phenol, as model antioxidant, was added to the reaction matrices with STX or GTX 2/3 and SRFA or NLFA. The results indicate that phenol had no significant impact on the photodegradation of STX or GTX 2/3 when added at concentrations up to 100 μM (Table B.7 and Figure B.11).

4.5.3 STX transformation products

TP candidates were monitored during the irradiation of STX in the presence of 2-AN over the course of 11 hours (Figure B.12). Full scan mass spectra of samples and controls were imported into *Compound Discoverer 3.3* (Thermo Scientific) and processed via a node-based workflow (Figure B.13) developed to enable automated peak picking, retention time alignment, blank subtraction, peak componentization (e.g., grouping of isotopes, adducts, multi-charged ions, and in-source fragments), and molecular formula assignment (only considering elements C, H, O, and N). To perform nontarget screening of TPs, data files associated with dark controls were designated as the "control" group, while data files associated with irradiated STX samples were designated as the "treatment" group using irradiation time as the study factor. TP candidates were

filtered based on the following criteria: (1) peak intensity above 10^5; (2) reasonable peak shape; (3) presence in samples from the treatment group but absence in the dark controls; (4) TP-like time-series pattern (e.g., continuously increase or increase and decrease over the course of photolysis experiments); and (5) a reasonable molecular formula derived from the accurate mass and the isotopic pattern. Three TP candidates with *m/z* at 223.0937, 253.1041, and 283.1149, respectively, were prioritized for structural elucidation. All three TP candidates showed gradual increasing peak areas for the first six hours of irradiation before gradually decaying (Figure B.12). The molecular formulae and calculated exact masses of the TP candidates are as follows: $C_8H_{11}N_6O_2$ (223.094349 amu), $C_9H_{13}N_6O_3$ (253.104914 amu), and $C_{10}H_{15}N_6O_4$ (283.115479 amu).

4.6 Discussion

4.6.1 Sensitized photolysis

The observed variations in sensitized photolysis pathways between STX, GTX 2/3, and C 1/2 is likely due to the pK_a differences of the congeners. At pH 6, STX has an overall + 2 charge from both guanidine groups, GTX 2/3 has a +1 charge due to its negatively charged sulfonic acid group, and C 1/2 has a +1 charge due to its sulfonic acid group and acidic amine. At pH 8, STX has a +1 charge, GTX 2/3 is neutral, and C 1/2 has a -1 charge. Sensitized degradation only occurred when the guanidine groups on STX or GTX 2/3 were partially deprotonated (Table B.8), suggesting that their degradation occurs via an electron transfer pathway mechanism involving this site in the molecule. The greater values of k_{STX}^{obs} for STX and GTX2/3 in the presence of NLFA as compared to SRFA are difficult to discuss without knowing the steady-state concentration of $^3DOM^*$ per mole of carbon in each of the isolates. However, knowing that the steady state concentrations of $^{\bullet}OH$ and $^1O_2$ are similar for SRFA and NLFA, and the toxins degrade primarily

through triplet-state electron transfer reactions, it can be inferred that NLFA has a higher $[^3DOM^*]_{ss}$ at 5 $mg_C\ L^{-1}$ or produces more reactive triplet states.

$^{\bullet}OH$ are the most reactive transient species which typically react via hydrogen-abstraction or addition with rate constants between 10^8-10^{10} $M^{-1}s^{-1}$ (Buxton et al., 1988). Because of their high reactivity and lack of selectivity, however, $^{\bullet}OH$ are easily quenched by DOM and have low steady-state concentrations ranging from 10^{-17}-10^{-15} M in surface waters (Haag & Hoigne, 1985; Zepp et al., 1987; Vione et al., 2006), so their overall contribution to substrate degradation may be insignificant, as in the case of saxitoxins. The lack of reaction between GTX 2/3 and $^1O_2$, a strong electrophile, is thought to be due to the electron-withdrawing sulfonate moiety on GTX 2/3. Low reactivity of either toxin toward $^1O_2$ was expected, since $^1O_2$ is a strong electrophile that typically reacts with dienes or other conjugated electron systems (Jaramillo et al., 2020; Di Mascio et al., 2019; Foote, 1968; Boreen et al., 2008). Due to the small contribution of $^1O_2$, this pathway was not further explored, but the reactivity of $^1O_2$ towards double bonds suggests the reaction site is the double bond at C2 or C8 of STX.

$^3DOM^*$ reacts with organic substrates mainly via oxidation or energy transfer reactions (McNeill & Canonica, 2016). STX and GTX 2/3 likely do not undergo energy transfer with $^3DOM^*$ since this typically occurs with conjugated electron systems (Stratakis & Orfanopoulos, 1997; Liu et al., 1965; Kellogg & Simpson, 1965). Electron transfer reactions have been well-documented between $^3DOM^*$ and amines (Görner, 2007; Chen et al., 2009; Zhou et al., 2013), depending on both the availability of nonbonding electrons on N and the presence of an alpha hydrogen (Görner, 2007; Zhou et al., 2013). Additionally, there is evidence that the presence of electron-withdrawing substituents decreases reactivity of the electron-transfer between $^3DOM^*$ and phenylurea herbicides (Wan et al., 2021). The dependence on pH for the availability of N-electrons on the 1,

2, 3- guanidine on STX and GTX 2/3 supports an electron-transfer mechanism. Furthermore, the electron-withdrawing sulfonic acid groups explain the lack of reactivity of C 1/2 and decreased reactivity of GTX 2/3 with triplet states.

Though the pseudo first-order reaction rates cannot directly be compared, differences in reactivity of the toxins with 2-AN and DOM may be due to a variety of factors. First, the one-electron reduction potential of 2-AN is relatively low (1.10 V; Gereche et al., 2001) while DOM varies across sources with an average of ~1.36-1.95 V (Gereche et al., 2001). Conversely, decreased reactivity toward DOM could be due to inhibition of electron-transfer reactions by phenolic moieties of DOM. Inhibition of triplet pathways is thought to depend on the stability of the radical cation of the substrate in an electron transfer with $^3DOM^*$ (Gereche et al., 2001; Wenk & Canonica, 2013; Leresche et al., 2016). The hydrogen transfer following the electron transfer with STX or GTX 2/3 and $^3DOM^*$ will occur rather quickly if the radical cations are unstable (Scheme 4.1), so the lack of inhibition effect is not unexpected. It has also been suggested that phenol produces long-lived phenoxyl radicals (Canonica et al., 2000) which could react with the toxins and therefore negate any inhibition caused by phenol.

4.6.2 Photodegradation mechanism

Scheme 4.1 outlines a potential mechanism for the reaction between STX and $^3DOM^*$ to form the TP candidates: $C_8H_{11}N_6O_2$ (223.0937 *m/z*), $C_9H_{13}N_6O_3$ (253.1041 *m/z*), and $C_{10}H_{15}N_6O_4$ (283.1149 *m/z*). The TP structures suggested in Scheme 4.1 were based on the STX parent compound structure and molecular formula. In the first steps of the mechanism, an electron is transferred from the lone pair of the neutral guanidine group (~50% deprotonated at pH 8) to $^3DOM^*$ with a subsequent proton transfer from the alpha H, forming a radical on the alpha carbon. Next, the radical on C6 is quenched by O_2, forming $O_2^{\bullet-}$ (Remke et al., 2021; Zepp et al., 1998),

and the resulting intermediate undergoes hydrolysis to form the products. Overall, the proposed mechanism is similar to the one postulated by Leresche et al. (2016) for the demethylation of n,n-dimethyl-4-cyanoaniline. The pH dependence, lack of contribution from $^{1}O_2$ and $^{\bullet}OH$, and effect of electron-withdrawing substituents on the photodegradation of the toxins f[56–58]urther support the proposed electron transfer pathway. Though the precise mechanism has yet to be confirmed through isolation and characterization of the TP candidates, measuring oxygen consumption, or measuring superoxide formation, the identification of TP molecular formulae and photoreaction sites adds to the understanding of the photodegradation pathways of STX and similar compounds.

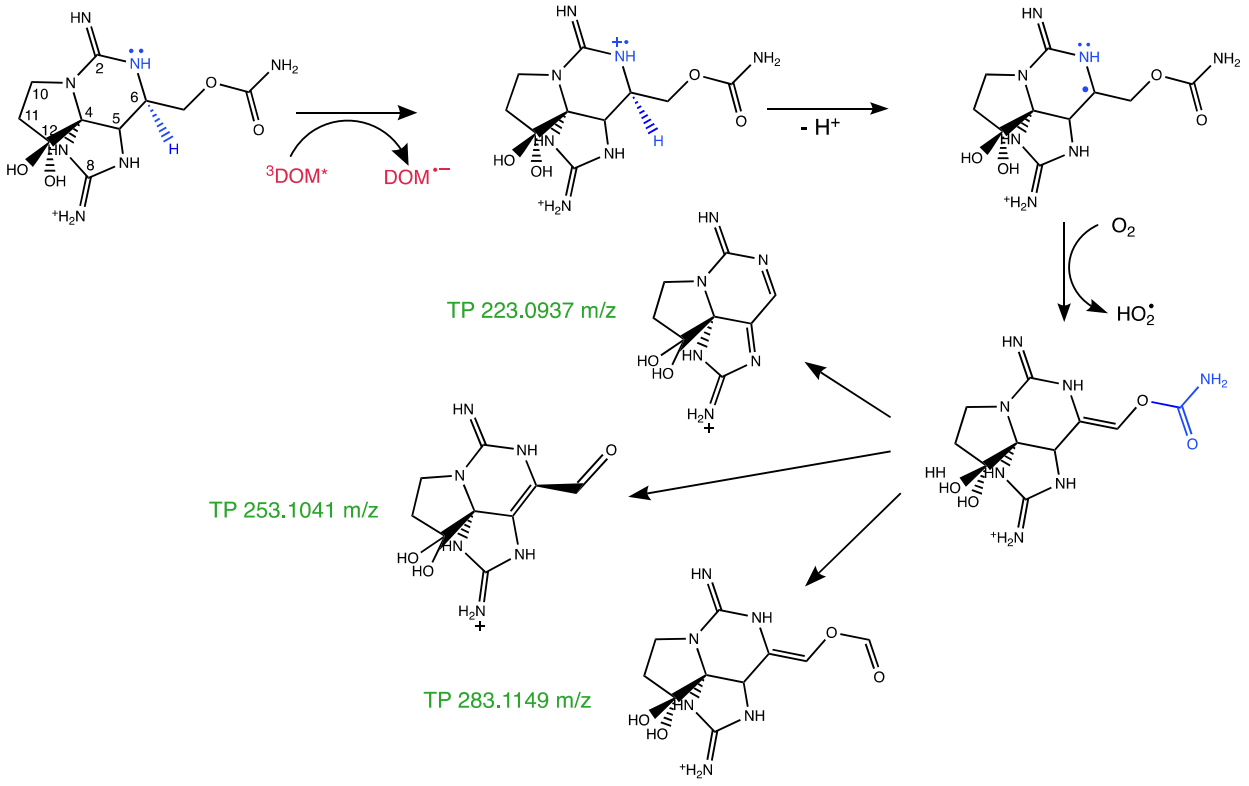

Scheme 4.1 Potential electron-transfer mechanism between saxitoxin (STX) and $^{3}DOM^{*}$ yielding the transformation product (TP) candidates, $C_8H_{11}N_6O_2$ (223.0937 m/z), $C_9H_{13}N_6O_3$ (253.1041 m/z), and $C_{10}H_{15}N_6O_4$ (283.1149 m/z).

4.6.3 APEX model of STX photolysis

Photoreactivity in natural waters depends on many factors including the sunlight pathlength, production and scavenging of RIs, and water chemistry (pH and concentrations of nitrate, nitrite, carbonate, bicarbonate, bromide, and DOC). Under the input conditions, APEX-estimated half-lives ranged between 0.08-3.5 SSD (Figure 4.4). As seen in Figure 4.4, the half-life of STX is the lowest at high [DOC], where the steady-state concentrations of RIs is greatest. The contribution of $^3DOM^*$ to the photodegradation of STX is dominant at [DOC] greater than 1 mg_C L^{-1}, but $^\bullet OH$ produced by nitrate and nitrite will have the greatest contribution in waters with little to no DOC. It is important to note that light screening will inhibit STX photolysis with increasing depths and turbidity. During a cyanobacterial bloom, high algal biomass would increase inhibition by light screening. Conversely, algal biomass is a source of DOM, which drives sensitized photodegradation. The APEX model highlights the importance of accounting for the impact of DOC concentration, water depth, and water chemistry on a substrate's half-life.

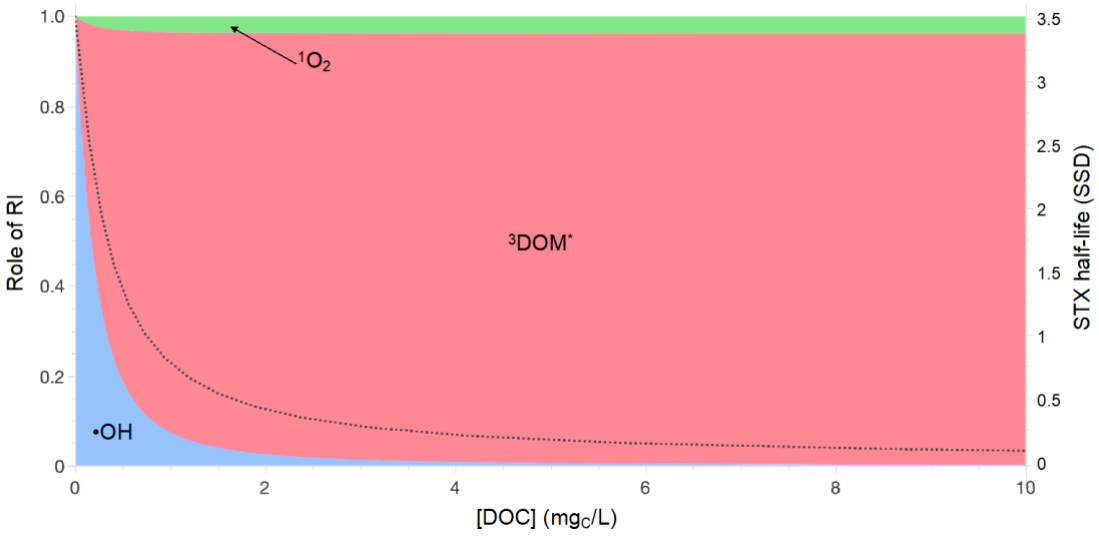

Figure 4.4 Role of reactive intermediates (RIs) and STX half-life (summer sunny days, SSD) as a function of DOC concentration (mg_C/L). The role of each RI is indicated as a fraction of overall photolysis, with $^1O_2$ in green, $^3DOM^*$ in red, and $^\bullet OH$ in blue. The dashed black line represents STX half-life. Data was downloaded from APEX code run through Octave 4.4.0 (Bodrato &Vione, 2014); the area plot was generated with JMP.

4.7 Conclusions

As concerns for cyanobacterial blooms continue to increase, understanding the environmental degradation pathways of cyanotoxins will be useful for the management of recreational and drinking water systems. Previous work has shown that some classes of cyanotoxins undergo phototransformation in sunlit surface waters, but to this point no photolysis pathway has been outlined for saxitoxins. This research showed that two saxitoxin analogues, STX and GTX 2/3, undergo sensitized photolysis at pH 8, with half-lives ranging from 1-10 hours. Evaluating the contributions of reactive species demonstrated that $^{3}DOM^{*}$ is the biggest contributor to sensitized photolysis for these toxins, with $^{1}O_2$ also contributing to STX's photodegradation at a DOC concentration of 5 $mg_C\ L^{-1}$. The observed pH dependence of the toxins' phototransformation and their degradation in the presence of 2-AN support a $^{3}DOM^{*}$-mediated oxidation pathway. Three transformation product candidates were identified and a mechanism for the photodegradation of STX was proposed. Future work should include further characterization and toxicity assessment of saxitoxin transformation products and evaluation of saxitoxin photodegradation in diverse environmental conditions (pH, temperature, algal biomass).

4.8 Acknowledgements

This work was supported by the National Science Foundation under Grant No. 2018497 and by the U.S. Army Research Office grant W911NF-20-1-0040.

5. Enhanced Degradation of Saxitoxins by Far-UVC Advanced Oxidation Processes

This chapter is in progress and will be submitted as: Norris, K. E; Payne, E.; Rosario-Ortiz, F.L. Enhanced Degradation of Saxitoxins by Far-UVC Advanced Oxidation Processes. **Expected Summer 2025.**

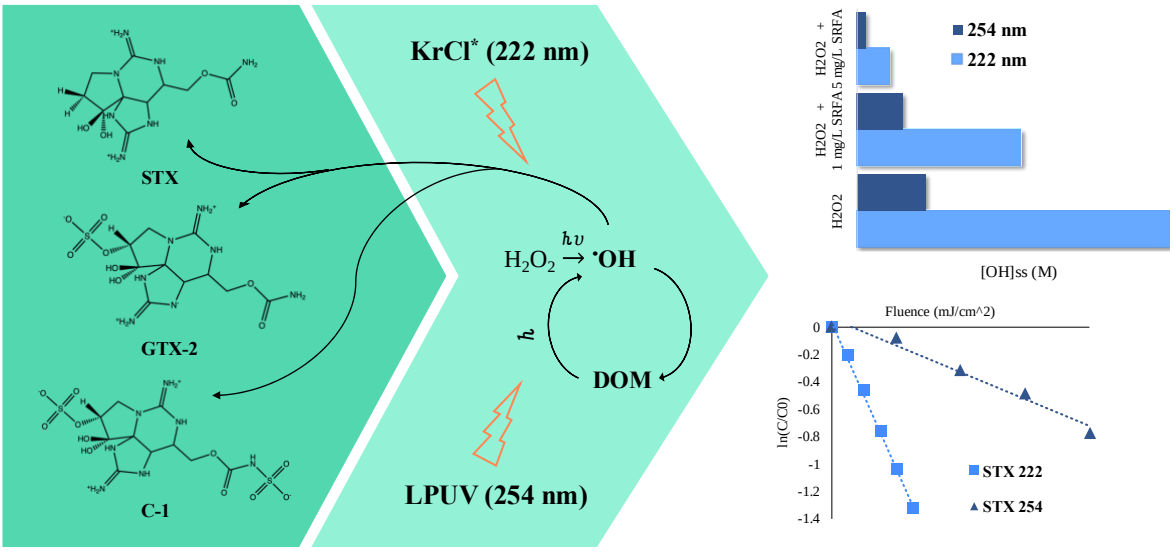

Figure 5.1 Graphical abstract for "Enhanced Degradation of Saxitoxins by Far-UVC Advanced Oxidation Processes".

5.1 Abstract

Harmful algal blooms (HABs) are becoming an increasing concern for drinking water utilities due to the production and release of cyanotoxins, including saxitoxins, into source waters. Many conventional water treatment processes have proven to be slow or ineffective in the removal of saxitoxins. This work investigated the removal of three saxitoxin congeners by UV-advanced oxidation processes (UV/AOP), utilizing KrCl* excimer and low-pressure UV (LPUV) lamps with hydrogen peroxide (H_2O_2) as a hydroxyl radical (•OH) promoter. After exposure to typical UV fluences, initial saxitoxin concentrations decreased by 30-75%, depending on congener and irradiation source. Degradation of all three saxitoxin congeners was 2.1-5.9 times faster in the KrCl* excimer system compared to the LPUV system due to the greater •OH steady-state

concentrations at 222 nm. While the addition of 1 mg_C L^{-1} of dissolved organic matter (DOM) caused a slight increase in saxitoxin degradation rates at 222 nm, saxitoxin removal was significantly inhibited in the presence of 5 mg_C L^{-1} DOM in both UV/ H_2O_2 systems because of increased $^{\bullet}OH$ scavenging by DOM.

5.2 Introduction

The global increasing occurrence of harmful algal blooms (HABs), largely due to climate change and eutrophication (O'Neil et al., 2012; Paerl & Paul, 2012; Paerl & Otten, 2013; Wurtsbaugh et al., 2019), has become a growing concern for both environmental and public health (Burford et al., 2020). Specifically, HABs have created major challenges in drinking water treatment because of the influx of algogenic organic matter (AOM), taste and odor compounds, and cyanotoxins (Hamilton et al., 2014, Dodds et al., 2009). It has been estimated that it has cost U.S. water utilities up to $30 million USD to upgrade their treatment processes to remove taste and odor compounds and cyanotoxins (Hamilton et al., 2014; U.S. EPA, 2015). Beyond the cost of water treatment, hundreds of millions of dollars have been spent on monitoring efforts, surface water remediation, and the treatment of HAB-related illnesses, and several million have been lost due to the impacts of HABs on tourism, recreation, and fisheries (Ralston et al., 2011; Bingham et al., 2015; Kouakou & Poder, 2019).

Cyanotoxins contain a wide variety of chemical structures and adverse biological effects. The main classes of cyanotoxins include hepatotoxins (microcystins and nodularins), cytotoxins, (cylindospermopsin), and neurotoxins (anatoxin-a and saxitoxins) (Carmichael et al., 2001). Saxitoxins are one of the most potent cyanotoxin classes (Wiese et al., 2010; Munday et al., 2013), including over 60 congeners produced by multiple genera of cyanobacteria and marine dinoflagellates. Of these congeners, some the most frequently detected are saxitoxin (STX), a

monosulfonated congener, gonyautoxin-2 and -3 (GTX-2/3), and the disulfonated n-sulfogonyautoxin-1 and -2 (C-1/2). If ingested, saxitoxins block sodium channels by binding to their receptors, inhibiting communication to the central nervous system and causing paralysis or death in some cases (Cestèle and Catterall, 2000; Munday et al., 2013). While saxitoxins are not currently subject to any national drinking water regulations in the United States (U.S. EPA, 2018), the World Health Organization recommended limit for acute exposure is 3 μg L^{-1} (World Health Organization, 2022). Considering its potency and the recent global increase of HABs, developing effective removal options is paramount to maintaining safe drinking water.

Previous work has demonstrated that saxitoxins are resistant to oxidation by many conventional methods including ozone, permanganate, and monochloramine (Newcombe & Nicholson, 2002; Ho et al., 2009; Maalouf et al., 2024). Rositano et al. (2001) and Orr et al. (2004) both found that ozone alone and in combination with hydrogen peroxide (H_2O_2) failed to degrade multiple saxitoxin congeners nor lower their toxicity. Potassium permanganate has been shown to have little effect on saxitoxin concentrations when added as a pre-oxidant dosed at 0.50 mg L^{-1} over 60 minutes (Ho et al., 2009), reacting with STX with a second-order rate constant of 1.7- 14 M^{-1} s^{-1} (increasing with pH) (Maalouf et al., 2024). Monochloramine has even lower second-order rate constants with STX, between 0- 0.8 M^{-1} s^{-1} (Maalouf et al., 2024). Until recently, chlorine was the only oxidant known to be effective in treating saxitoxins (Rositano et al., 1998; Newcombe & Nicholson, 2002; Nicholson et al., 2003; Ho et al., 2009; Maalouf et al., 2024). Second-order rate constants between STX and chlorine have been found to range from 16 M^{-1} s^{-1} (pH 6) to 1.4×10^4 M^{-1} s^{-1} (pH 10) for STX (Maalouf et al., 2024), with slower removal rates observed for other congeners (Nicholson et al., 2003; Ho et al., 2009). Due to their lack of absorbance in the UV-visible range, saxitoxins are not expected to be susceptible to direct photochemical degradation

(Norris et al., 2024). However, a recent article (Maalouf et al., 2024) demonstrated that UV-advanced oxidation processes, specifically UV/H_2O_2, may be an effective removal method for saxitoxins due to the fast reaction between STX and •OH ($k_{STX,\bullet OH}$ = 4.6 × 10^8 M^{-1} s^{-1} at pH 6-8, increasing to 1.5 × 10^9 M^{-1} s^{-1} at pH 10). The second-order rate constants between •OH and decarbamoyl saxitoxin (dcSTX) or neosaxitoxin (neoSTX) are on the same order of magnitude as STX (Maalouf et al., 2024).

The capacity for optimization of UV-AOP for the removal of saxitoxins in drinking water remains wide due to the lack of research on saxitoxins in drinking water treatment. In this study, we investigated the efficacy of two UV/H_2O_2 systems (254 nm and 222 nm) and evaluated the impact of DOM concentration on the removal of three saxitoxin congeners, STX, GTX-2/3, and C-1/2. Krypton chloride ($KrCl^*$) excimer lamps, emitting light at 222 nm, have been shown to generate hydroxyl radicals from H_2O_2 at rates almost 10 times higher than low-pressure UV (LPUV) sources that emit light at 254 nm (Payne et al., 2022), offering potentially much more efficient degradation of contaminants (Liu et al., 2017; Xu & Huan, 2023; Zhao et al., 2023; Bai et al., 2024). This work aims to expand the knowledge of effective techniques for the removal of saxitoxins and highlight the advantages of far-UVC (<230 nm) irradiation over the conventional LPUV light used in UV/H_2O_2 water treatment systems.

5.3 Materials and Methods

5.3.1 Chemicals and solutions

A complete list of reagents used in this work can be found in Table C.1. Saxitoxin certified calibration solutions were obtained from National Research Council Canada. STX (61.4 μM) and GTX-2/3 (146.1 μM, combined mixture of GTX-2 and GTX-3) standards arrived as solutions dissolved in 0.5 mM hydrochloric acid (HCl). C-1/2 (121.2 μM, combined mixture of C-1 and C-

2) arrived as a solution dissolved in 20 μM acetic acid. Experimental solutions containing saxitoxin standards were made fresh daily and were stored at 4 °C in silanized glass vials since saxitoxins adsorb to usual glass. All solutions were prepared in deionized water (18.2 mΩ cm, 5 ppb total organic carbon (TOC)) produced by a Sartorius arium proDI dispenser. Experimental solutions were maintained at pH 7 ± 0.05 using 10 mM sodium phosphate buffer. H_2O_2 solutions were prepared from a 30% w/v stock solution and concentrations in initial experimental solutions was measured using the I_3^- method as outline by Klassen et al. (1994).

Two DOM isolates were selected to represent the impact of DOM on saxitoxin degradation rates and •OH steady-state concentrations. These were Nordic Lake fulvic acid (NLFA, 1R105F) and Suwannee River fulvic acid (SRFA, 1S101F), were purchased from the International Humic Substances Society (St. Paul, Minnesota). The composition and characteristics of these fulvic acids can be found in Table C.2. DOM stock solutions (50 $mg_C\ L^{-1}$) were prepared in 10 mM phosphate buffer (pH 7.0 ± 0.1). After ~24 hr of stirring, the solutions were filtered with ultrapure water prewashed with Whatman 0.45 μm poly(ether sulfone) filters.

5.3.2 UV Exposures

UV exposures were performed in a bench-scale collimated beam apparatus. The far-UVC source used in this work was a KrCl* excimer lamp (USHIO, Cypress, CA) with a bandpass filter applied to isolate the 222 nm peak from a small peak at 258 nm emitted by the lamp. The LPUV source that was used contains four conventional mercury lamps emitting at 254 nm (15 W each, G15T8, USHIO). Incident UV irradiance was measured using a calibrated radiometer and sensor (models ILT5000 and SED240, respectively, International Light Inc.). The average fluence rate (E_0) of each system was determined by correcting the incident irradiance for sample depth, sample absorbance, water factor, reflection factor, divergence factor, and Petri factor (Bolton & Linden,

2003). For the 254 nm system, the incident irradiance was ~ 1 mW cm^{-2} and for the 222 nm system it was ~0.3 mW cm^{-2}. The incident irradiance was measured daily prior to experiments and the incident and average fluence rates for all experiments is shown in Table S3. The "incident fluence rate (E_{inc})", an adaptation to E_0 which omits the water factor, was used to normalize hydroxyl radical steady-state concentrations ($[^{\bullet}OH]_{ss}$) to the number of photons entering the water matrix to facilitate comparison between KrCl* and LPUV systems (Payne et al., 2022). Solutions were made in 6 cm diameter polystyrene Petri dishes (irradiation path length of 0.6 cm) and stirred continuously with a flea stir bar to ensure gentle mixing.

5.3.3 Analytical instrumentation

Saxitoxin concentrations were quantified using an Agilent 1200 series HPLC system equipped with an Agilent Eclipse Plus C-18 5 μm particle size reverse-phase column. An isocratic HPLC method was applied with fluorescence detection at 340/390 nm (excitation/detection) and a mobile phase consisting of a 10 mM ammonium formate solution with 2.5% acetonitrile that was adjusted to pH 6 with acetic acid. The flowrate of the mobile phase was 1 mL min^{-1} and the injection volume was 50 μL. A Cary-4000 UV-vis spectrophotometer was used to measure absorbance of experimental solutions and DOM isolates (Figure C.1). Organic carbon was measured using a Sievers M5310C TOC analyzer.

5.4 Results and Discussion

5.4.1 Direct UV and UV/H_2O_2 exposures

The transformation of saxitoxins exposed to direct UV and UV/H_2O_2 systems was evaluated by determining pseudo first-order rate constants at each wavelength ($k'_{STX,222nm}$ and $k'_{STX,254nm}$) were determined based on Equation 5.1, where F represents the UV fluence, the product

of the average irradiance (E_0) and the exposure time. The average irradiance for each experiment is listed in Table C.3.

$$ln(\frac{[STX]}{[STX]_0}) = -k'_{STX}F \quad (5.1)$$

Direct exposure to either $KrCl^*$ or LPUV radiation in ultrapure water had no effect on the concentrations of the three saxitoxin congeners, which was expected since the toxins do not absorb light above 190 nm (Norris et al., 2024) and undergo extremely slow hydrolysis (Jones & Negri, 1997). In the presence of 10 ppm H_2O_2, degradation of all three congeners was observed (Figure 5.2), with pseudo-first order rate constants ranging from 1.89- 5.16 $\times 10^{-3}$ cm^2 mJ^{-1} in the $KrCl^*$ system and 0.34 -1.05 $\times 10^{-3}$ cm^2 mJ^{-1} in the LPUV system (Table 5.1). The lower degradation rates of GTX and C1/2 compared to STX are likely due to the varying speciation of their guanidinium groups at pH 7 and the additional one and two electron-withdrawing sulfonate functional groups on GTX-2/3 and C-1/2, respectively. Since saxitoxins have been shown to be unreactive with H_2O_2 alone (Orr et al., 2004), it can be assumed that all observed degradation is due to reactions with $^{\bullet}OH$. Previous work has reported second-order rate constants between different saxitoxin congeners and $^{\bullet}OH$ ($k_{STX,^{\bullet}OH}$) of 4.6 $\times 10^8$- 1.5 $\times 10^9$ M^{-1} s^{-1} (Norris et al., 2024; Maalouf et al., 2024). Hydroxyl radicals have been shown to react with guanidinium groups on DNA guanosine and similar compounds via hydrogen abstraction or $^{\bullet}OH$ addition (Chatgilialoglu et al., 2011; Fleming et al., 2022). STX, GTX-2/3, and C-1/2 each contain two guanidinium groups, likely the targets of H-abstraction or $^{\bullet}OH$ addition.

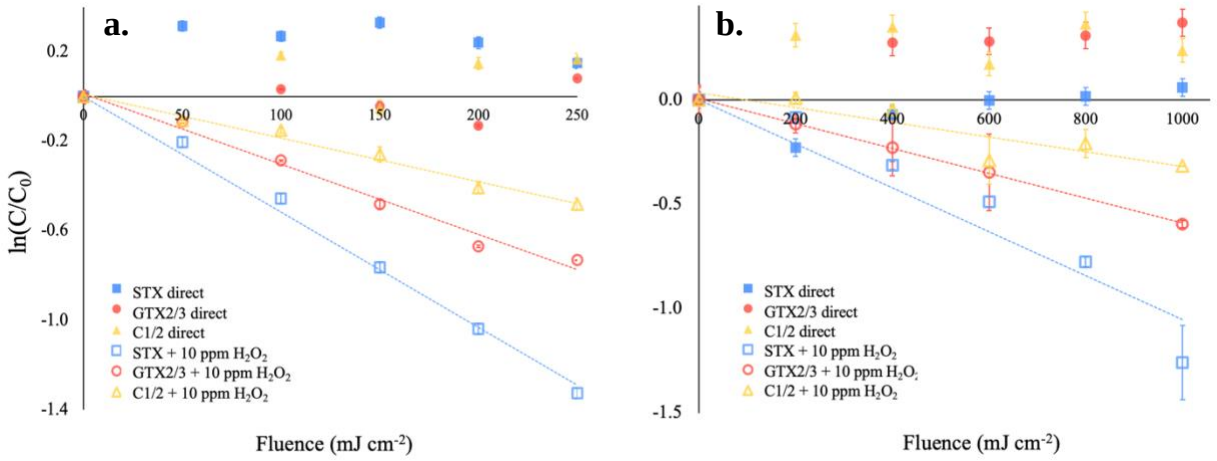

Figure 5.2 Transformation of saxitoxin (STX), gonyautoxin 2 and 3 (GTX 2/3), and n-sulfocarbamoyl gonyautoxin 1 and 2 (C 1/2) during exposure to (a) $KrCl^*$ excimer and (b) LPUV radiation. The natural logarithm of saxitoxin concentration over its initial concentration (500 nM) is shown on the y-axis and the UV fluence of the lamps is shown on the x-axis. Closed markers represent saxitoxins in ultrapure water without hydrogen peroxide; open markers represent saxitoxins in the presence of 10 ppm H_2O_2.

5.5 Influence of radiation source

Prior work has demonstrated that the rate of hydroxyl radical production is almost ten times higher in $KrCl^*/H_2O_2$ systems compared to $LPUV/H_2O_2$ (Payne et al., 2022), which can be attributed to the higher molar absorptivity of H_2O_2 and UV photon energy at 222 nm (99 ±1 M^{-1} cm^{-1} and 539 kJ mol^{-1}, respectively) compared to 254 nm (21 ± 0.2 $M^{-1}cm^{-1}$ and 471 kJ mol^{-1}, respectively; Payne et al., 2022). Accordingly, saxitoxin degradation rates were 2.1-5.9 times higher in the $KrCl^*/H_2O_2$ system compared to $LPUV/H_2O_2$ in systems both with and without the addition of DOM (Table 5.1).

Table 5.1 Fluence-based rate constants for three saxitoxin congeners: saxitoxin (STX), gonyautoxin 2 and 3 (GTX-2/3), or n-sulfocarbamoyl gonyautoxin 1 and 2 (C-1/2). Initial solutions contained 10 ppm H_2O_2, 10 mM phosphate buffer (pH 7), and 500 nM toxin, some spiked with 1 or 5 $mg_C\ L^{-1}$ SRFA or NLFA. Solutions were exposed to either 222 nm (KrCl* excimer, top row) or 254 nm (LPUV, bottom row) irradiation. 95% confidence intervals are indicated in parentheses.

	Saxitoxin congener	Ultrapure water	1 $mg_C\ L^{-1}$ SRFA[a]	1 $mg_C\ L^{-1}$ NLFA[b]	5 $mg_C\ L^{-1}$ SRFA[a]	5 $mg_C\ L^{-1}$ NLFA[b]
$k'_{STX,222nm}$ ($\times 10^{-3}\ cm^2\ mJ^{-1}$)	**STX**	5.16 (±0.28)	2.54 (±0.41)	6.20 (±1.79)	2.12 (±0.12)	1.88 (±0.12)
	GTX 2/3	3.08 (±0.26)	2.82 (±1.55)	1.48 (±0.31)	0.81 (±0.14)	0.48 (±0.09)
	C 1/2	1.89 (±0.17)	1.02 (±0.31)	1.38 (±0.67)	0.70 (±0.21)	0.59 (±0.18)
$k'_{STX,254nm}$ ($\times 10^{-3}\ cm^2\ mJ^{-1}$)	**STX**	1.05 (±0.24)	0.75 (±0.12)	1.23 (±0.34)	0.36 (±0.03)	0.41 (±0.05)
	GTX 2/3	0.85 (±0.24)	0.72 (±0.31)	0.82 (±0.37)	0.28 (±0.09)	0.60 (±0.26)
	C 1/2	0.34 (±0.20)	0.29 (±0.21)	0.30 (±0.27)	0.14 (±0.05)	0.28 (±0.17)

[a]SRFA= Suwanee River fulvic acid
[b]NLFA = Nordic Lake fulvic acid

The steady-state concentrations of •OH ($[^{\bullet}OH]_{ss}$) of each UV/H_2O_2 system were estimated using known •OH quantum yields and scavenging constants according to Equations 5.2 and 5.3. In these equations, $r_{\bullet OH}$ is the rate of •OH production by H_2O_2 and/or DOM, $k_{\bullet OH,S}$ is the second-order rate constant between •OH and each •OH scavenger in the system. $r_{\bullet OH}$ was determined using Equation 5.3, where $\phi_{H_2O_2,\lambda}$ and $\phi_{DOM,\lambda}$ are the wavelength-dependent quantum yield of •OH from H_2O_2 and DOM, respectively, and $\varepsilon_{H_2O_2,\lambda}$ and $\varepsilon_{DOM,\lambda}$ are the molar absorptivities of H_2O_2 and DOM, respectively.

$$[^{\bullet}OH]_{ss} = \frac{r_{\bullet OH}}{\sum k_{\bullet OH,S}[S]} \tag{5.2}$$

$$r_{\bullet OH} = E_0([H_2O_2]\phi_{H_2O_2,\lambda}\varepsilon_{H_2O_2,\lambda} + [DOM]\phi_{DOM,\lambda}\varepsilon_{DOM,\lambda}) \tag{5.3}$$

Molar absorptivities of H_2O_2 and the DOM isolates were determined based on the absorbance of solutions of 10 ppm H_2O_2 or 5 $mg_C\ L^{-1}$ DOM. $\phi_{H_2O_2,\lambda}$ has been previously

determined (Payne et al., 2022) and is listed along $\varepsilon_{H_2O_2,\lambda}$ and $\varepsilon_{DOM,\lambda}$ in Table C.4. $\phi_{DOM,\lambda}$ was determined based on the degradation of pCBA in the presence of DOM isolates (Text C.3 and Table C.4). $[^{\bullet}OH]_{ss}$ values listed in Table 5.2 correspond to the UV/AOP systems in Table 5.1.

Table 5.2 Hydroxyl radical steady-state concentrations normalized to E_{inc} (Table C.3) in each $KrCl^*/H_2O_2$ or $LPUV/H_2O_2$ system. All solutions contained 10 ppm H_2O_2 in ultrapure water or with 1 or 5 $mg_C\,L^{-1}$ SRFA or NLFA. pCBA was added at 10 uM for the pCBA method. Solutions for which the quantum yield/scavenging constant method was applied also contained 500 nM saxitoxin (STX). A light screening factor was applied in all $[^{\bullet}OH]_{ss}$ calculations (Text C.1).

$[^{\bullet}OH]_{ss}/E_{inc}$ ($M\,cm^2\,mW^{-1} \times 10^{-14}$)	Ultrapure water	1 $mg_C\,L^{-1}$ SRFA[a]	1 $mg_C\,L^{-1}$ NLFA[b]	5 $mg_C\,L^{-1}$ SRFA[a]	5 $mg_C\,L^{-1}$ NLFA[b]
UV_{222}	301 (±3.0)	155 (±1.8)	109 (±1.2)	35.0 (±0.57)	31.1 (±0.33)
UV_{254}	61.8 (±0.59)	42.2 (±0.42)	29.2 (±0.28)	8.39 (±0.09)	8.88 (±0.09)

[a]SRFA= Suwanee River fulvic acid
[b]NLFA = Nordic Lake fulvic acid

5.6 Influence of DOM

DOM acts as both a source and sink of •OH (Qian et al., 2001; Vione et al., 2006; Westerhoff et al., 2007; Page et al., 2011; Vione et al., 2014). In surface waters, DOM has been shown to produce •OH at rates on the order of ~10^{11} M s^{-1} (Page et al., 2011; Vione et al., 2006; Zhou & Mopper, 1990). While •OH produced by DOM may play a significant role in the sensitized photochemical fate of contaminants in surface waters (Haag & Cao, 1992; Boreen et al., 2003; Vione et al., 2010; Remucal, 2014), the production of •OH by DOM is likely too inefficient to contribute to contaminant degradation during UV/AOP due to shorter residence times. To our knowledge, the rates of •OH production and •OH quantum yields from SRFA and NLFA had not previously been measured for 222 nm exposures. In this study, $\phi_{DOM,222nm}$ was 2.30×10^{-3} for SRFA and 1.19×10^{-3} for NLFA, and $\phi_{DOM,254nm}$ was 7.73×10^{-4} and 8.90×10^{-4} for SRFA and NLFA,

respectively (Table C.4). In addition, scavenging of •OH can be predicted based on second-order rate constants between •OH and DOM, which range from 1.39- 4.53 × 10^8 M_C^{-1} s^{-1} for SRFA (Westerhoff et al., 2007; McKay et al., 2011) and 2.98 × 10^8 M_C^{-1} s^{-1} for NLFA (Norris et al., 2024). At the DOM concentrations used in this work (1- 5 mg_C L^{-1}), the scavenging factors for DOM ($\Sigma k_{\bullet OH,DOM}[DOM]$) are between 1.2- 18.8 × 10^4 s^{-1}, which increase the total scavenging factor ($\Sigma k_{\bullet OH,S}[S]$) to 2.4- 24 times the total scavenging factors of the systems with only H_2O_2 and saxitoxins in ultrapure water. Accordingly, the $[^{\bullet}OH]_{ss}/E_{inc}$ values in control experiments containing only DOM isolates DOM (no added H_2O_2) are 2-3 orders of magnitude lower than systems spiked with H_2O_2 (Table C.5).

DOM is a source of other reactive intermediates, including triplet state DOM ($^3DOM^*$) and singlet oxygen ($^1O_2$) which may sensitize the degradation of contaminants (Vione et al., 2014; Fotiou et al., 2016; Di Mascio et al., 2019; Jaramillo et al., 2020; Barrios et al., 2021; Natumi et al., 2021). In our previous work, $^3DOM^*$ contributed to >94%, $^1O_2$ contributed ~5%, and •OH contributed ~0.25% to the degradation of saxitoxins under simulated sunlight (Norris et al., 2024). It is thus conceivable that $^3DOM^*$ and $^1O_2$ contributed to some of the observed saxitoxin degradation in the UV/H_2O_2 systems. The $[^{\bullet}OH]_{ss}/E_{inc}$ of both UV systems containing 1 mg_C L^{-1} NLFA and 10 ppm H_2O_2 are much lower than those of the 10 ppm H_2O_2 systems, suggesting that the increased rate of STX degradation in the 1 mg_C L^{-1} NLFA/10 ppm H_2O_2 systems is not due to •OH. However, the addition of DOM in all other cases caused a decrease in saxitoxin degradation.

Light screening by DOM may also affect rates of •OH production by decreasing the amount of light absorbed by H_2O_2 or other radical promoters (Xu & Huang, 2023; Zhao et al., 2023). However, light screening effects were accounted for by applying a screening factor to all $r_{\bullet OH}$ measurements (Text C.1), thus the reported $[^{\bullet}OH]_{ss}/E_{inc}$ (Table 2) reflect near-surface conditions.

Considering the light screening correction and the low $[^{\bullet}OH]_{ss}/E_{inc}$ in systems containing DOM, it is not surprising that the addition of either SRFA or NLFA showed significant inhibition of saxitoxin degradation (Table 5.1) and lower •OH steady-state concentrations (Table 5.2) in both LPUV systems. This work demonstrates that the role of DOM as an •OH sink outweighs its role as a source of •OH in UV/H_2O_2 systems, thus, high DOM concentrations will significantly inhibit the targeted removal of contaminants.

5.7 Conclusions

As HABs continue to threaten public health and create challenges for water treatment, utilities must be prepared to face spikes in cyanobacteria and cyanotoxin concentrations in source waters. Although there are no current regulations on saxitoxins in drinking water, saxitoxins have been reported to reach concentrations in surface waters over 60 times the WHO recommended limit in drinking water (Christenson & Khan, 2020; World Health Organization, 2022). Due to the slow degradation of saxitoxins when exposed to ozone, permanganate oxidation, and monochloramine (Maalouf et al., 2024), it is imperative to develop and optimize alternative removal methods. This work demonstrated that UV/H_2O_2 with both $KrCl^*$ excimer and LPUV light sources is effective at degrading saxitoxins via indirect photochemical reactions with •OH. In comparing UV/H_2O_2 systems, the $KrCl^*$ excimer system with 0-1 mg_C L^{-1} DOM yielded the highest degradation rates for all saxitoxin congeners, reflected by the higher $[^{\bullet}OH]_{ss}$/Einc. Results from this study emphasize the advantages of UV_{222}/H_2O_2 over UV_{254}/H_2O_2 due to the enhanced generation of •OH under 222 nm irradiation, even in the presence of DOM. This study aims to guide utilities in the optimization of UV/H_2O_2, or AOP systems involving other radicals and reactive intermediates, for the removal of saxitoxins and similarly persistent contaminants.

Further investigation should concentrate on the effect of UV/H_2O_2 and chlorination processes on the toxicity of water matrices that contain saxitoxins to ensure safety of treated drinking water, as observed abatement in the parent toxin compound may not translate to an overall decrease in toxicity. While the transformation products of STX have been identified for their reaction with triplet states, future work is needed to characterize the products of hydroxylation or H-abstraction for saxitoxin congeners. Also, the generation of $^{\bullet}OH$ by DOM isolates under 222 nm irradiation had not previously been explored, but investigation should be continued regarding the production of reactive intermediates by DOM under far-UVC irradiation.

5.8 Acknowledgements

This work was supported by the U.S. Army Research Office grant W911NF-20-1-0040. The authors would also like to acknowledge the laboratory assistance of Alyx McCaig and Claire Brown through the University of Colorado Science Discovery Program.

6. Conclusion and Outlook

The research presented in this thesis explores the fundamental properties and photochemical reactivity of DOM, applying this knowledge to address the rising concern of cyanotoxins and their fate in natural and engineered aquatic systems. Chapters 2 and 3 contribute to the decades-long effort to characterize the structure and behaviors of DOM, emphasizing how the concentration, solvent properties, and molecular composition of DOM influence its three-dimensional conformation and production of reactive intermediates. Chapters 4 and 5 give novel insights into the photochemical fate of saxitoxins, which will help inform public health of their persistence in natural systems and guide utilities in the application of UV-AOP for their removal from drinking water.

Chapter 2 is a perspective article which presents a unified depiction of the three-dimensional structure of DOM based on findings from across several fields. As the study of DOM is at the nexus of soil and water research, previous models for DOM structure have attempted to fit all entities of DOM into one category (i.e. macromolecules or supramolecular assemblies). As an effort to combine past models and reflect the true nature of DOM, a new structural model is introduced, termed the *mixed dynamic assembly model* (MDAM). The MDAM model describes DOM as a mixture of freely dissolved molecules, some assemblies of molecules held together by strong H-bonds, with the capacity to form larger assemblies under certain conditions through weak noncovalent interactions. By defining a comprehensive structural model for DOM, we aim to align perspectives of the solubility and intermolecular interactions between DOM molecules in both environmental and engineered systems. Evidence of influence of ionic strength, concentration, pH, and the addition of organic acids on DOM conformation reveals the implications of solution chemistry both for DOM characterization and in predicting its behaviors in various aquatic

systems. Also, the contribution of charge-assisted H-bonds to the stability of DOM assemblies demonstrates the influence of DOM composition on its intermolecular interactions. Looking forward, Chapter 2 highlights the need for further work in understanding the dynamics of DOM associations and how DOM structure impacts the environmental fate of contaminants and nutrient availability, as well as the chemical transformations of DOM through biodegradation, photodegradation, and engineered oxidation processes.

In Chapter 3, novel insights into the mechanisms of hydroxyl radical production by DOM are delineated. Using model quinones and hydroxybenzoic acids, probe compounds, and quenchers, we distinguished the generation of free $^{\bullet}$OH from lower-energy hydroxylating species to the transformation of probe compounds, and assessed the contribution of the H_2O_2-dependent pathway. It was found that most quinones cannot generate $^{\bullet}$OH unless in the presence of an electron donor, such as phenol, but are capable of inducing the hydroxylation of benzoic acid and terephthalic acid through the formation of a quinone-water exciplex or biradical ($[Q]^{*}\cdots H_2O/QH^{\bullet}$–$^{\bullet}$OH). On the other hand, hydroxybenzoic acids produce free $^{\bullet}$OH through multiple mechanisms, one involving the production of H_2O_2 (contributing to ~35% of overall $^{\bullet}$OH production) likely initiated by photoionization of the substituted phenols. Based on triplet quinone deactivation rate constants, it was estimated that only at environmentally relevant concentrations of DOM, only 10-20% of hydroxylating species formed by DOM are free $^{\bullet}$OH. This chapter demonstrates that typical methods used to measure $^{\bullet}$OH from DOM overestimate free $^{\bullet}$OH production, which may lead to inaccurate predictions of contaminant degradation rates in natural aquatic systems. Chapter 3 also emphasizes the advantages of using model compounds to understand the specific mechanisms responsible for bulk DOM properties and reactivity. Future work should focus on the mechanisms of $^{\bullet}$OH production by substituted phenols (including those formed during engineered

oxidation of DOM), larger quinone and hydroxybenzoic acid derivatives that would better represent the true molecular size of DOM, and mixtures of electron accepting molecules (mainly aromatic ketones and quinones) with electron donors found in DOM. The production of •OH by DOM will continue to be relevant to understanding the persistence of contaminants in the environment, and it is important that researchers understand how DOM composition determines its photoreactivity.

Chapter 4 harnesses the fundamental knowledge of DOM photochemistry from Chapter 3 in evaluating the photodegradation saxitoxins in natural aquatic systems. This research reveals that three congeners of saxitoxins undergo sensitized photodegradation in sunlit surface waters with half lives between 1-10 hours, mainly due to electron transfer reactions with $^{3}DOM^{*}$. Elucidating the degradation rates and mechanisms of saxitoxins is helpful to assess their persistence as harmful cyanobacterial blooms continue to threaten the health of aquatic systems and humans. Since saxitoxins are the most potent class of cyanotoxins and are resistant to many other natural degradation processes, it is imperative to continue to understand the mechanisms of their environmental fate as well as the parallel development of potential remediation and drinking water removal methods. Further, while three transformation products of saxitoxin were identified in this chapter, additional research is needed to identify the structures and toxicity of the photodegradation products of saxitoxins and other cyanobacterial metabolites.

In Chapter 5, UV_{222} and UV_{254} irradiation combined with H_2O_2 was applied to assess a potential option to remove saxitoxins from drinking water. Saxitoxin concentrations decreased by 30-75% in the presence of 10 ppm H_2O_2, however, degradation was 2.1-5.9 times faster in the 222 nm $KrCl^{*}$ system compared to the 254 nm LPUV system. This research not only provides a guidance for the optimization of UV/AOP systems in the removal of saxitoxins, but demonstrates

the enhanced efficiency of $KrCl^*$ systems compared to LPUV in the targeted removal of contaminants. This chapter also displays the prominent role of DOM as an inhibitor to contaminant degradation due to high rates of $^{\bullet}OH$ scavenging and light screening, however, DOM may contribute as a source of reactive intermediates at low concentrations (<2 $mg_C\ L^{-1}$). Since UV_{222} is still an emerging technology, several questions remain regarding the cost-effectiveness of $KrCl^*$ systems, the impact of background water matrices, and formation of byproducts. Future investigations should continue to optimize UV_{222}/AOP in the targeted removal of persistent contaminants such as saxitoxins, analyze the dual role of DOM as a source and sink for reactive intermediates under UV_{222} irradiation, and assess the byproducts of saxitoxins and DOM after exposure to UV_{222}.

This thesis simultaneously addresses some of the fundamental properties and behaviors of DOM while providing practical information regarding the fate of saxitoxins in environmental and engineered systems. Chapters 3 and 4 provoke additional questions regarding the structures and toxicity of saxitoxin phototransformation products, as well as the behaviors of DOM in UV_{222}/AOP systems. While Chapters 2 and 3 of this research advance our understanding of DOM conformation and photochemical reactivity, they also highlight the challenges in studying the chemical mechanisms of a complex group of molecules for which the exact chemical structures are unknown. Model photosensitizers and computational models have proven to be help elucidate the specific mechanisms involved in RI formation and visualize interactions between DOM molecules. However, to more accurately represent the properties and behaviors of DOM in natural systems, a broader set of model compounds and computational structures should be used in future investigations. Collectively, this thesis highlights the importance of understanding the fundamental

chemistry of DOM and its many realms of influence, including the fate of emerging contaminants, biogeochemical cycling, and water/wastewater treatment processes.

References

Aeschbacher, M.; Graf, C.; Schwarzenbach, R. P.; Sander, M. Antioxidant Properties of Humic Substances. *Environ. Sci. Technol.* **2012**, *46* (9), 4916–4925. https://doi.org/10.1021/es300039h.

Aiken, G. R.; Malcolm, R. L. Molecular Weight of Aquatic Fulvic Acids by Vapor Pressure Osmometry. *Geochim. Cosmochim. Acta* **1987**, *51* (8), 2177–2184. https://doi.org/10.1016/0016-7037(87)90267-5.

al Housari, F.; Vione, D.; Chiron, S.; Barbati, S. Reactive Photoinduced Species in Estuarine Waters. Characterization of Hydroxyl Radical, Singlet Oxygen and Dissolved Organic Matter Triplet State in Natural Oxidation Processes. *Photochem Photobiol Sci* **2010**, *9* (1), 78–86. https://doi.org/10.1039/b9pp00030e.

Appiani, E.; Ossola, R.; Latch, D. E.; Erickson, P. R.; McNeill, K. Aqueous singlet oxygen reaction kinetics of furfuryl alcohol: Effect of temperature, pH, and salt content. *Environmental Science: Processes and Impacts* **2017**, *19*(4), 507–516. https://doi.org/10.1039/c6em00646a

Aquino, A. J. A.; Tunega, D.; Pašalić, H.; Schaumann, G. E.; Haberhauer, G.; Gerzabek, M. H.; Lischka, H. Molecular Dynamics Simulations of Water Molecule-Bridges in Polar Domains of Humic Acids. *Environ. Sci. Technol.* **2011**, *45* (19), 8411–8419. https://doi.org/10.1021/es201831g.

Baalousha, M.; Motelica-Heino, M.; Coustumer, P. L. Conformation and Size of Humic Substances: Effects of Major Cation Concentration and Type, pH, Salinity, and Residence Time. *Colloids Surf. Physicochem. Eng. Asp.* **2006**, *272* (1–2), 48–55. https://doi.org/10.1016/j.colsurfa.2005.07.010.

Bai, Q.; Wu, Q.-Y.; Ye, B.; Wu, Y.-P.; Lee, J.-W.; Lee, M.-Y.; Wang, W.-L. Assessing Excimer Far-UVC (222 Nm) Irradiation for Advanced Oxidation Processes: Oxidants Photochemistry and Micropollutants Degradation. *Water Research* **2024**, *267*, 122505. https://doi.org/10.1016/j.watres.2024.122505.

Baigorri, R.; Fuentes, M.; González-Gaitano, G.; García-Mina, J. M. Simultaneous Presence of Diverse Molecular Patterns in Humic Substances in Solution. *J. Phys. Chem. B* **2007**, *111* (35), 10577–10582. https://doi.org/10.1021/jp0738154.

Barrios, B.; Mohrhardt, B.; Doskey, P. V.; Minakata, D. Mechanistic Insight into the Reactivities of Aqueous-Phase Singlet Oxygen with Organic Compounds. *Environ. Sci. Technol.* **2021**, *55* (12), 8054–8067. https://doi.org/10.1021/acs.est.1c01712.

Bates, H. A.; Rapoport, Henry. Chemical Assay for Saxitoxin, the Paralytic Shellfish Poison. *J. Agric. Food Chem.* **1975**, *23* (2), 237–239. https://doi.org/10.1021/jf60198a016.

Bates, H. A.; Kostriken, R.; Rapoport, H. A Chemical Assay for Saxitoxin. Improvements and Modifications. *J. Agric. Food Chem.* **1978**, *26* (1), 252–254. https://doi.org/10.1021/jf60215a060.

Batistela, V.R., Pellosi, D.S., de Souza, F.D., da Costa, W.F., de Oliveira Santin, S.M., de Souza, V.R., Caetano, W., de Oliveira, H.P.M., Scarminio, I.S., Hioka, N. pK_a determination of xanthene derivates in aquous solutions by multivariate analysis applied to UV-Vis spectrophotometric data. *Spectrochim. Acta. A.* **2011**, *79*, 889–897. https://doi.org/10.1016/j.saa.2011.03.027.

Batoréu, M. C. C.; Dias, E.; Pereira, P.; Franca, S. Risk of Human Exposure to Paralytic Toxins of Algal Origin. *Environmental Toxicology and Pharmacology* **2005**, *19* (3), 401–406. https://doi.org/10.1016/j.etap.2004.12.002.

Bingham, M; Lupi, F.; Sinha, S. K. *Economic Benefits of Reducing Harmful Algal Blooms in Lake Erie*; Environmental Consulting & Technology, Inc, 2015; p 66. https://legacyfiles.ijc.org/tinymce/uploaded/Publications/Economic-Benefits-Due-to-Reduction-in-HABs-October-2015.pdf (accessed 2025-03-03).

Blough, N. V.; Zepp, R. G. Reactive Oxygen Species in Natural Waters. In *Active Oxygen in Chemistry*; Foote, C. S., Valentine, J. S., Greenberg, A., Liebman, J. F., Eds.; Springer Netherlands: Dordrecht, 1995; pp 280–333. https://doi.org/10.1007/978-94-007-0874-7_8.

Bodesheim, M.; Schütz, M.; Schmidt, R. Triplet State Energy Dependence of the Competitive Formation of O2(1Σ+g), O2(1Δg) and O2(3Σ−g) in the Sensitization of O2 by Triplet States. *Chemical Physics Letters* **1994**, *221* (1), 7–14. https://doi.org/10.1016/0009-2614(94)87008-X.

Bodrato, M and Vione, D. APEX (Aqueous Photochemistry of Environmentally occurring Xenobiotics): a free software tool to predict the kinetics of photochemical processes in surface waters. *Environmental Science: Processes & Impacts* **2014**, *16*, 732- 740. https://doi-org.colorado.idm.oclc.org/10.1039/C3EM00541K

Boreen, A. L.; Arnold, W. A.; McNeill, K. Photodegradation of Pharmaceuticals in the Aquatic Environment: A Review. *Aquat. Sci.* **2003**, *65* (4), 320–341. https://doi.org/10.1007/s00027-003-0672-7.

Boreen, A.; Edhlund, B.; Cotner, J.; McNeill, K. Indirect Photodegradation of Dissolved Free Amino Acids: The Contribution of Singlet Oxygen and the Differential Reactivity of DOM from Various Sources. *Environ. Sci. Technol.* **2008** *42*(15), 5492-5498. https://doi.org/10.1021/es800185d

Buckley, S.; McKay, G.; Leresche, F.; Rosario-Ortiz, F. Inferring the Molecular Basis for Dissolved Organic Matter Photochemical and Optical Properties. *Environ. Sci. Technol.* **2024**. https://doi.org/10.1021/acs.est.3c10881.

Burford, M. A.; Carey, C. C.; Hamilton, D. P.; Huisman, J.; Paerl, H. W.; Wood, S. A.; Wulff, A. Perspective: Advancing the Research Agenda for Improving Understanding of Cyanobacteria in a Future of Global Change. *Harmful Algae* **2020**, *91*, 101601. https://doi.org/10.1016/j.hal.2019.04.004.

Burns, J. M.; Hall, S.; Ferry, J. L. The Adsorption of Saxitoxin to Clays and Sediments in Fresh and Saline Waters. *Water Research* **2009**, *43* (7), 1899–1904. https://doi.org/10.1016/j.watres.2009.02.004.

Buxton, G. V.; Greenstock, C. L.; Helman, W. P.; Ross, A. B. Critical Review of Rate Constantsfor Reactions of Hydrated Electrons, Hydrogen Atoms and Hydroxyl Radicals (·OH/·O^- in Aqueous Solution. *Journal of Physical and Chemical Reference Data* **1988**, *17* (2), 513–886. https://doi.org/10.1063/1.555805.

Buxton, G. V.; Stuart, C. R. Re-evaluation of the thiocyanate dosimeter for pulse radiolysis. *J. Chem. Soc., Faraday Trans*. **1995**, 91, 279-281. https://doi.org/10.1039/FT9959100279.

Canonica, S.; Jans, U.; Stemmler, K.; Hoigne, J. Transformation Kinetics of Phenols in Water: Photosensitization by Dissolved Natural Organic Material and Aromatic Ketones. *Environ. Sci. Technol.* **1995**, *29* (7), 1822–1831. https://doi.org/10.1021/es00007a020.

Canonica, S.; Hellrung, B.; Wirz, J. Oxidation of Phenols by Triplet Aromatic Ketones in Aqueous Solution. *J. Phys. Chem. A* **2000**, *104* (6), 1226–1232. https://doi.org/10.1021/jp9930550.

Carmichael W. W. The Cyanotoxins, *Advances in Botanical Research* **1997**, *27*, 211-256. https://doi.org/10.1016/S0065-2296(08)60282-7.

Carmichael, W. W. Cyanobacteria secondary metabolites—the cyanotoxins, *Journal of Applied Bacteriology* **1992**, *72* (6), 445–459. https://doi.org/10.1111/j.1365-2672.1992.tb01858.x

Carmichael, W. W.; Azevedo, S. M.; An, J. S.; Molica, R. J.; Jochimsen, E. M.; Lau, S.; Rinehart, K. L.; Shaw, G. R.; Eaglesham, G. K. Human Fatalities from Cyanobacteria: Chemical and Biological Evidence for Cyanotoxins. *Environ Health Perspect* **2001**, *109* (7), 663–668.

Carmichael, W. W.; Azevedo, S. M.; An, J. S.; Molica, R. J.; Jochimsen, E. M.; Lau, S.; Rinehart, K. L.; Shaw, G. R.; Eaglesham, G. K. Human Fatalities from Cyanobacteria: Chemical and Biological Evidence for Cyanotoxins. *Environ Health Perspect* **2001**, *109* (7), 663–668.

Castro, D.; Vera, D.; Lagos, N.; García, C.; Vásquez, M. The Effect of Temperature on Growth and Production of Paralytic Shellfish Poisoning Toxins by the Cyanobacterium Cylindrospermopsis Raciborskii C10. *Toxicon* **2004**, *44* (5), 483–489. https://doi.org/10.1016/j.toxicon.2004.06.005.

Cestèle, S.; Catterall, W. A. Molecular Mechanisms of Neurotoxin Action on Voltage-Gated Sodium Channels. *Biochimie* **2000**, *82* (9), 883–892. https://doi.org/10.1016/S0300-9084(00)01174-3.

Chandler, D. Interfaces and the Driving Force of Hydrophobic Assembly. *Nature* **2005**, *437* (7059), 640–647. https://doi.org/10.1038/nature04162.

Chatgilialoglu, C.; D'Angelantonio, M.; Kciuk, G.; Bobrowski, K. New Insights into the Reaction Paths of Hydroxyl Radicals with 2′-Deoxyguanosine. *Chem. Res. Toxicol.* **2011**, *24* (12), 2200–2206. https://doi.org/10.1021/tx2003245.

Chen, Y.; Hu, C.; Hu, X.; Qu, J. Indirect Photodegradation of Amine Drugs in Aqueous Solution under Simulated Sunlight. *Environ. Sci. Technol.* **2009**, *43* (8), 2760–2765. https://doi.org/10.1021/es803325j.

Chin, Y.-P.; Mcknight, D.; D'Andrilli, J.; Brooks, N.; Cawley, K.; Guerard, J.; Perdue, E.; Stedmon, C.; Tratnyek, P.; Westerhoff, P.; Wozniak, A.; Bloom, P.; Foreman, C.; Gabor, R.; Hamdi, J.; Hanson, B.; Hozalski, R.; Kellerman, A.; McKay, G.; Reckhow, D. Identification of Next-Generation International Humic Substances Society Reference Materials for Advancing the Understanding of the Role of Natural Organic Matter in the Anthropocene. *Aquat. Sci.* **2023**, *85*, 32. https://doi.org/10.1007/s00027-022-00923-x.

Chorus, I., & Welker, M. (Eds.). Toxic Cyanobacteria in Water: A Guide to Their Public Health Consequences, Monitoring and Management (2nd ed.). *CRC Press.* **2021** https://doi.org/10.1201/9781003081449

Christensen, V. G.; Khan, E. Freshwater Neurotoxins and Concerns for Human, Animal, and Ecosystem Health: A Review of Anatoxin-a and Saxitoxin. *Sci Total Environ* **2020**, *736*, 139515. https://doi.org/10.1016/j.scitotenv.2020.139515.

Conte, P.; Piccolo, A. Conformational Arrangement of Dissolved Humic Substances. Influence of Solution Composition on Association of Humic Molecules. *Environ. Sci. Technol.* **1999**, *33* (10), 1682–1690. https://doi.org/10.1021/es9808604.
Cooper, W. J.; Lean, D. R. S. Hydrogen Peroxide Concentration in a Northern Lake: Photochemical Formation and Diel Variability. *Environ. Sci. Technol.* **1989**, *23* (11), 1425–1428. https://doi.org/10.1021/es00069a017.

Couch, K.; Leresche, F.; Farmer, C.; McKay, G.; Rosario-Ortiz, F. L. Assessing the Source of the Photochemical Formation of Hydroxylating Species from Dissolved Organic Matter Using Model Sensitizers. *Environ. Sci.: Processes Impacts* **2022**, *24* (1), 102–115. https://doi.org/10.1039/D1EM00345C.

Del Vecchio, R.; Blough, N. V. On the Origin of the Optical Properties of Humic Substances. *Environ. Sci. Technol.* **2004**, *38* (14), 3885–3891. https://doi.org/10.1021/es049912h.

Di Mascio, P.; Martinez, G. R.; Miyamoto, S.; Ronsein, G. E.; Medeiros, M. H. G.; Cadet, J. Singlet Molecular Oxygen Reactions with Nucleic Acids, Lipids, and Proteins. *Chem. Rev.* **2019**, *119* (3), 2043–2086. https://doi.org/10.1021/acs.chemrev.8b00554.

Ding, Y.; Teppen, B. J.; Boyd, S. A.; Li, H. Measurement of Associations of Pharmaceuticals with Dissolved Humic Substances Using Solid Phase Extraction. *Chemosphere* **2013**, *91* (3), 314–319. https://doi.org/10.1016/j.chemosphere.2012.11.039.

Dodds, W. K.; Bouska, W. W.; Eitzmann, J. L.; Pilger, T. J.; Pitts, K. L.; Riley, A. J.; Schloesser, J. T.; Thornbrugh, D. J. Eutrophication of U.S. Freshwaters: Analysis of Potential Economic Damages. *Environ. Sci. Technol.* **2009**, *43* (1), 12–19. https://doi.org/10.1021/es801217q.

Elemental Compositions and Stable Isotopic Ratios of IHSS Samples. International Humic Substances Society. https://humicsubstances.org/elemental-compositions-and-stable-isotopic-ratios-of-ihss-samples/ (accessed May 10, 2023).

Engebretson, R. R.; Von Wandruszka, Ray. Micro-Organization in Dissolved Humic Acids. *Environ. Sci. Technol.* **1994**, *28* (11), 1934–1941. https://doi.org/10.1021/es00060a026.

EPA Drinking Water Health Advisories for Cyanotoxins. U.S. EPA. https://www.epa.gov/habs/epa-drinking-water-health-advisories-cyanotoxins (accessed 2025-03-02).

Escalona, Y.; Petrov, D.; Galicia-Andrés, E.; Oostenbrink, C. Exploring the Macroscopic Properties of Humic Substances Using Modeling and Molecular Simulations. *Agronomy* **2023**, *13* (4), 1044. https://doi.org/10.3390/agronomy13041044.

Fang, F.; Gao, Y.; Gan, L.; He, X.; Yang, L. Effects of different initial pH and irradiance levels on cyanobacterial colonies from Lake Taihu, China. *Journal of Applied Phycology* **2018**, 30(3). https://doi.org/10.1007/s10811-018-1394-5.

Fleming, A. M.; Burrows, C. J. Chemistry of ROS-Mediated Oxidation of the Guanine Base in DNA and Its Biological Consequences. *International journal of radiation biology* **2021**, *98* (3), 452. https://doi.org/10.1080/09553002.2021.2003464.

Foote, C. S. Mechanisms of Photosensitized Oxidation. *Science* **1968**, *62* (3857), 963-970. https://doi.org/10.1126/science.162.3857.963

Fotiou, T.; Triantis, T. M.; Kaloudis, T.; O'Shea, K. E.; Dionysiou, D. D.; Hiskia, A. Assessment of the Roles of Reactive Oxygen Species in the UV and Visible Light Photocatalytic Degradation of Cyanotoxins and Water Taste and Odor Compounds Using C–TiO2. *Water Research* **2016**, *90*, 52–61. https://doi.org/10.1016/j.watres.2015.12.006.

Gan, D.; Jia, M.; Vaughan, P.; Falvey, D.; Blough, N. Aqueous. Photochemistry of Methyl-Benzoquinone. *J. Phys. Chem. A* **2008**, *112*, 2803-2812. https://doi.org/10.1021/jp710724e

Gehringer, M. M.; Wannicke, N. Climate Change and Regulation of Hepatotoxin Production in Cyanobacteria. *FEMS Microbiol Ecol* **2014**, *88* (1), 1–25. https://doi.org/10.1111/1574-6941.12291.

Gerecke, A. C.; Canonica, S.; Müller, S. R.; Schärer, M.; Schwarzenbach, R. P. Quantification of Dissolved Natural Organic Matter (DOM) Mediated Phototransformation of Phenylurea Herbicides in Lakes. *Environ. Sci. Technol.* **2001**, *35* (19), 3915–3923. https://doi.org/10.1021/es010103x.

Gorner, H. Photoreduction of 9,10-Anthraquinone Derivatives: Transient Spectroscopy and Effects of Alcohols and Amines on Reactivity in Solution. *Photochem. Photobio*. **2003** *77* (2), 171-179. https://doi.org/10.1562/00318655

Görner, H. Photoinduced Oxygen Uptake for 9,10-Anthraquinone in Air-Saturated Aqueous Acetonitrile in the Presence of Formate, Alcohols, Ascorbic Acid or Amines. *Photochem. Photobiol. Sci.* **2006**, *5* (11), 1052–1058. https://doi.org/10.1039/B606968A.

Görner, H. Oxygen Uptake after Electron Transfer from Amines, Amino Acids and Ascorbic Acid to Triplet Flavins in Air-Saturated Aqueous Solution. *Journal of Photochemistry and Photobiology B: Biology* **2007**, *87* (2), 73–80. https://doi.org/10.1016/j.jphotobiol.2007.02.003.

Grandbois, M.; Latch, D. E.; McNeill, K. Microheterogeneous Concentrations of Singlet Oxygen in Natural Organic Matter Isolate Solutions. *Environ. Sci. Technol.* **2008**, *42* (24), 9184–9190. https://doi.org/10.1021/es8017094.

Grebel, J. E.; Pignatello, J. J.; Mitch, W. A. Sorbic Acid as a Quantitative Probe for the Formation, Scavenging and Steady-State Concentrations of the Triplet-Excited State of Organic Compounds. *Water Research **2011**, 45* (19), 6535–6544. https://doi.org/10.1016/j.watres.2011.09.048.

Guidelines for Drinking-Water Quality, Fourth edition incorporating the first and second addenda.; World Health Organization, Ed.; World Health Organization: Geneva, 2022.

Haag, W. R. & Hoigne, J. Photo-Sensitized Oxidation in Natural Waters via •OH Radicals. *Chemosphere* **1985**, *14* (1l/12), 1659-1671. https://doi.org/10.1016/0045-6535(85)90107-9

Haag, W. R.; Yao, C. C. D. Rate Constants for Reaction of Hydroxyl Radicals with Several Drinking Water Contaminants. *Environ. Sci. Technol.* **1992**, *26* (5), 1005–1013. https://doi.org/10.1021/es00029a021.

Hamilton, D. P.; Wood, S. A.; Dietrich, D. R.; Puddick, J. Costs of Harmful Blooms of Freshwater Cyanobacteria. In *Cyanobacteria*; John Wiley & Sons, Ltd, 2014; pp 245–256. https://doi.org/10.1002/9781118402238.ch15.

Hassett, J. P. Dissolved Natural Organic Matter as a Microreactor. *Science* **2006**, *311* (5768), 1723–1724. https://doi.org/10.1126/science.1123389.

Hayes, M. H. B.; Swift, R. S. Vindication of Humic Substances as a Key Component of Organic Matter in Soil and Water. In *Advances in Agronomy*; Elsevier, 2020; Vol. 163, pp 1–37. https://doi.org/10.1016/bs.agron.2020.05.001.

Haynes, W.M. (ed.). *CRC Handbook of Chemistry and Physics*. 94th Edition. CRC Press LLC, Boca Raton: FL **2013**, 3-344.

He, X.; de la Cruz, A. A.; Hiskia, A.; Kaloudis, T.; O'Shea, K.; Dionysiou, D. D. Destruction of Microcystins (Cyanotoxins) by UV-254 Nm-Based Direct Photolysis and Advanced Oxidation Processes (AOPs): Influence of Variable Amino Acids on the Degradation Kinetics and

Reaction Mechanisms. *Water Research* **2015**, *74*, 227–238. https://doi.org/10.1016/j.watres.2015.02.011.

Herkstroeter, W. G.; Lamola, A. A.; Hammond, G. S. Mechaisms of Photochemical Reactions in Solution. XXVIII. 1 Values of Triplet Excitation energies of Selected Sensitizers. *Journal of the American Chemical Society* **1964**, *86*(21), 4537–4540. https://doi.org/10.1021/ja01075a005

Hertkorn, N.; Frommberger, M.; Witt, M.; Koch, B. P.; Schmitt-Kopplin, Ph.; Perdue, E. M. Natural Organic Matter and the Event Horizon of Mass Spectrometry. *Anal. Chem.* **2008**, *80* (23), 8908–8919. https://doi.org/10.1021/ac800464g.

Ho, L.; Tanis-Plant, P.; Kayal, N.; Slyman, N.; Newcombe, G. Optimising Water Treatment Practices for the Removal of Anabaena Circinalis and Its Associated Metabolites, Geosmin and Saxitoxins. *Journal of Water and Health* **2009**, *7* (4), 544–556. https://doi.org/10.2166/wh.2009.075.

Ho, L., Tang, T., Monis, P. T., & Hoefel, D. Biodegradation of multiple cyanobacterial metabolites in drinking water supplies. *Chemosphere*, **2012** *87*(10), 1149–1154. https://doi.org/10.1016/j.chemosphere.2012.02.020

Ho, L.; Hoefel, D.; Grasset, C.; Palazot, S.; Newcombe, G.; Saint, C. P.; & Brookes, J. D. Removal of cyanobacterial metabolites through wastewater treatment plant filters. *Water Science and Technology* **2012** *65*(7), 1244–1251. https://doi.org/10.2166/wst.2012.002

Iglesias, A.; López, R.; Gondar, D.; Antelo, J.; Fiol, S.; Arce, F. Effect of pH and Ionic Strength on the Binding of Paraquat and MCPA by Soil Fulvic and Humic Acids. *Chemosphere* **2009**, *76* (1), 107–113. https://doi.org/10.1016/j.chemosphere.2009.02.012.

International Humic Substances Society 2024 Products. International Humic Substances Society. https://humicsubstances.org/ (accessed 2024-06-05).

Isolation of IHSS Samples. International Humic Substances Society. https://humic-substances.org/isolation-of-ihss-samples/ (accessed 2024-06-04).

Jaramillo, M.; Joens, J. A.; O'Shea, K. E. Fundamental Studies of the Singlet Oxygen Reactions with the Potent Marine Toxin Domoic Acid. *Environ. Sci. Technol.* **2020**, *54* (10), 6073–6081. https://doi.org/10.1021/acs.est.9b07380.

Jaramillo, M.; Joens, J.A.; O'Shea, K.E. Fundamental studies of the singlet oxygen reactions with the potent marine toxin domoic acid. *Environmental Science & Technology* **2020**, *54* (10), 6073-6081. doi:10.1021/acs.est.9b07380.

Jin, H.; Lian, L.; Zhou, H.; Yan, S.; Song, W. Mechanistic consideration of the photochemical transformation of domoic acid (algal toxin) in DOM-Rich brackish water. *Chemosphere* **2018** *209*, 328–337. doi:10.1016/j.chemosphere.2018.06.084.

Jin, S.; Mofidi, A. A.; Linden, K. G. Polychromatic UV Fluence Measurement Using Chemical Actinometry, Biodosimetry, and Mathematical Techniques. *J. Environ. Eng.* **2006**, *132* (8), 831–841. https://doi.org/10.1061/(ASCE)0733-9372(2006)132:8(831).

Jones, G. J.; Negri, A. P. Persistence and Degradation of Cyanobacterial Paralytic Shellfish Poisons (PSPs) in Freshwaters. *Water Research* **1997**, *31* (3), 525–533. https://doi.org/10.1016/S0043-1354(96)00134-0.

Jørgensen, N. O. G.; Podduturi, R.; Michelsen, C. F.; Jepsen, T.; Moraes, M. de A. B. Fate of Saxitoxins in Lake Water: Preliminary Testing of Degradation by Microbes and Sunlight. *Water* **2022**, *14* (21), 3556. https://doi.org/10.3390/w14213556.

Kellogg, R. E. & Simpson, W. T. Perturbation of Singlet-Triplet Transition Energies *J. Am. Chem. Soc.* **1965**, *87* (19), 4230–4234. https://doi.org/10.1021/ja00947a002

Klassen, N. V.; Marchington, David.; McGowan, H. C. E. H2O2 Determination by the I3- Method and by KMnO4 Titration. *Anal. Chem.* **1994**, *66* (18), 2921–2925. https://doi.org/10.1021/ac00090a020.

Koprivnjak, J. F.; Perdue, E. M.; Pfromm, P. H. Coupling Reverse Osmosis with Electrodialysis to Isolate Natural Organic Matter from Fresh Waters. *Water Res.* **2006**, *40* (18), 3385–3392. https://doi.org/10.1016/j.watres.2006.07.019.

Kouakou, C. R. C.; Poder, T. G. Economic Impact of Harmful Algal Blooms on Human Health: A Systematic Review. *J Water Health* **2019**, *17* (4), 499–516. https://doi.org/10.2166/wh.2019.064.

Kurtz, T.; Zeng, T.; Rosario-Ortiz, F. L. Photodegradation of Cyanotoxins in Surface Waters. *Water Research* **2021**, *192*, 116804. https://doi.org/10.1016/j.watres.2021.116804.

Lam, B.; Simpson, A. J. Investigating Aggregation in Suwannee River, USA, Dissolved Organic Matter Using Diffusion-Ordered Nuclear Magnetic Resonance Spectroscopy. *Environ. Toxicol. Chem.* **2009**, *28* (5), 931–939. https://doi.org/10.1897/08-441.1.

Lambert, C. R., & Kochevar, I. E. Electron Transfer Quenching of the Rose Bengal Triplet State. *Photochemistry and Photobiology* **1997**, *66*(1), 15–25. https://doi.org/10.1111/j.1751-1097.1997.tb03133.x

Laszakovits Juliana R. P-Nitroanisole/Pyridine and p-Nitroacetophenone/Pyridine Actinometers Revisited: Quantum Yield in Comparison to Ferrioxalate. *Environmental Science & Technology Letters* **2017**, *v. 4* (1), 11–14. https://doi.org/10.1021/acs.estlett.6b00422.

Latch, D. E.; McNeill, K. Microheterogeneity of Singlet Oxygen Distributions in Irradiated Humic Acid Solutions. *Science* **2006**, *311* (5768), 1743–1747. https://doi.org/10.1126/science.1121636.

Lawrence, J. F.; Niedzwiadek, B. Quantitative Determination of Paralytic Shellfish Poisoning Toxins in Shellfish by Using Prechromatographic Oxidation and Liquid Chromatography with

Fluorescence Detection. *Journal of AOAC INTERNATIONAL* **2001**, *84* (4), 1099–1108. https://doi.org/10.1093/jaoac/84.4.1099.

Leenheer, J. A.; Rostad, C. E.; Gates, P. M.; Furlong, E. T.; Ferrer, I. Molecular Resolution and Fragmentation of Fulvic Acid by Electrospray Ionization/Multistage Tandem Mass Spectrometry. *Anal. Chem.* **2001**, *73* (7), 1461–1471. https://doi.org/10.1021/ac0012593.

Lehn, J.-M. *Supramolecular Chemistry—Scope and Perspectives Molecules, Supermolecules, and Molecular Devices (Nobel Lecture)*. Angew. Chem. Int. Ed. Engl., 27: 89-112. https://doi.org/10.1002/anie.198800891 https://onlinelibrary.wiley.com/doi/epdf/10.1002/anie.198800891 (accessed 2024-04-01).

Leresche, F.; von Gunten, U.; Canonica, S. Probing the Photosensitizing and Inhibitory Effects of Dissolved Organic Matter by Using *N* , *N* -Dimethyl-4-Cyanoaniline (DMABN). *Environ. Sci. Technol.* **2016**, *50* (20), 10997–11007. https://doi.org/10.1021/acs.est.6b02868.

Leresche, F.; McKay, G.; Kurtz, T.; von Gunten, U.; Canonica, S.; Rosario-Ortiz, F. L. Effects of Ozone on the Photochemical and Photophysical Properties of Dissolved Organic Matter. *Environ. Sci. Technol.* **2019**, *53* (10), 5622–5632. https://doi.org/10.1021/acs.est.8b06410.

Leresche, F.; Salazar, J. R.; Pfotenhauer, D. J.; Hannigan, M. P.; Majestic, B. J.; Rosario-Ortiz, F. L. Photochemical Aging of Atmospheric Particulate Matter in the Aqueous Phase. *Environ. Sci. Technol.* **2021**, acs.est.1c00978. https://doi.org/10.1021/acs.est.1c00978.

Leresche, F.; Vialykh, E. A.; Rosario-Ortiz, F. L. Computational Calculation of Dissolved Organic Matter Absorption Spectra. *Environ. Sci. Technol.* **2022**, *56* (1), 491–500. https://doi.org/10.1021/acs.est.1c06252.

Li, H.; McKay, G. Fluorescence Quenching of Humic Substances and Natural Organic Matter by Nitroxide Free Radicals. *Environ. Sci. Technol.* **2023**, *57* (1), 719–729. https://doi.org/10.1021/acs.est.2c02220.

Lian, L.; Yao, B.; Hou, S.; Fang, J.; Yan, S.; Song, W. Kinetic Study of Hydroxyl and Sulfate Radical-Mediated Oxidation of Pharmaceuticals in Wastewater Effluents. *Environ. Sci. Technol.* **2017**, *51* (5), 2954–2962. https://doi.org/10.1021/acs.est.6b05536

Liu, J.; Ye, J.; Ou, H.; Lin, J. Effectiveness and Intermediates of Microcystin-LR Degradation by UV/H2O2 via 265 Nm Ultraviolet Light-Emitting Diodes. *Environ Sci Pollut Res* **2017**, *24* (5), 4676–4684. https://doi.org/10.1007/s11356-016-8148-1.

Liu, R. S. H.; Turro, N. J.; Hammond, G. S. Mechanisms of Photochemical Reactions in Solution. XXXI. Activation and Deactivation of Conjugated Dienes by Energy Transfer. *J. Am. Chem. Soc.* **1965**, *87* (15), 3406–3412. https://doi.org/10.1021/ja01093a021.

Liu, Y.; Ren, J.; Wang, X.; Fan, Z. Mechanism and reaction pathways for microcystin-LR degradation through UV/H2O2 treatment. *PLoS ONE* **2016**, *11*(6), 1– 11. doi:10.1371/journal.pone.0156236.

Maalouf, S.; Adams, C.; Hoppe-Jones, C. Determination of Oxidation Rate Constant for Nodularin-r, Saxitoxin, Dc-Saxitoxin, and Neo-Saxitoxin with Conventional Water Treatment Plant Oxidants and Advanced Oxidation Processes. *AWWA Water Science* **2024**, *6* (3), e1374. https://doi.org/10.1002/aws2.1374.

MacCarthy, P. A Proposal to Establish a Reference Collection of Humic Materials for Interlaboratory Comparisons. *Geoderma* **1976**, *16* (2), 179–181. https://doi.org/10.1016/0016-7061(76)90039-2.

Mao, J.; Cao, X.; Olk, D. C.; Chu, W.; Schmidt-Rohr, K. Advanced Solid-State NMR Spectroscopy of Natural Organic Matter. *Prog. Nucl. Magn. Reson. Spectrosc.* **2017**, *100*, 17–51. https://doi.org/10.1016/j.pnmrs.2016.11.003.

Maoz, A.; Chefetz, B. Sorption of the Pharmaceuticals Carbamazepine and Naproxen to Dissolved Organic Matter: Role of Structural Fractions. *Water Res.* **2010**, *44* (3), 981–989. https://doi.org/10.1016/j.watres.2009.10.019.

McKay, G. Emerging Investigator Series: Critical Review of Photophysical Models for the Optical and Photochemical Properties of Dissolved Organic Matter. *Environ. Sci. Process. Impacts* **2020**, *22* (5), 1139–1165. https://doi.org/10.1039/D0EM00056F.

McKay, G.; Dong, M. M.; Kleinman, J. L.; Mezyk, S. P.; Rosario-Ortiz, F. L. Temperature Dependence of the Reaction between the Hydroxyl Radical and Organic Matter. *Environ. Sci. Technol.* **2011**, *45* (16), 6932–6937. https://doi.org/10.1021/es201363j.

McKay, G.; Korak, J. A.; Erickson, P. R.; Latch, D. E.; McNeill, K.; Rosario-Ortiz, F. L. The Case Against Charge Transfer Interactions in Dissolved Organic Matter Photophysics. *Environ. Sci. Technol.* **2018**, *52* (2), 406–414. https://doi.org/10.1021/acs.est.7b03589.

McNeill, K. & Canonica, S. Triplet State Dissolved Organic Matter in Aquatic Photochemistry: Reaction Mechanisms, Substrate Scope, and Photophysical Properties. *Environ. Sci.: Processes Impacts* **2016**, *18* (11), 1381–1399. https://doi.org/10.1039/C6EM00408C.

McNeill, K.; Canonica, S. Triplet State Dissolved Organic Matter in Aquatic Photochemistry: Reaction Mechanisms, Substrate Scope, and Photophysical Properties. *Environ. Sci.:Processes Impacts* **2016**, *18* (11), 1381–1399. https://doi.org/10.1039/C6EM00408C.

Mitschke, N.; Vemulapalli, S. P. B.; Dittmar, T. NMR Spectroscopy of Dissolved Organic Matter: A Review. *Environ. Chem. Lett.* **2022**. https://doi.org/10.1007/s10311-022-01528-4.

Mohamed, Z.A.; Mostafa, Y.; Alamri, S.; Hashem, M.; Alrumman, S. Biotransformation and detoxification of saxitoxin by *Bacillus flexus* in batch experiments. *Archives of Microbiology* **2023**, *205*(63)

Molecular Weight to Size Calculator. NanoComposix. https://nanocomposix.com/pages/molecular-weight-to-size-calculator (accessed 2024-06-05).

Mopper, K.; Stubbins, A.; Ritchie, J. D.; Bialk, H. M.; Hatcher, P. G. Advanced Instrumental Approaches for Characterization of Marine Dissolved Organic Matter: Extraction Techniques, Mass Spectrometry, and Nuclear Magnetic Resonance Spectroscopy. *Chem. Rev.* **2007**, *107* (2), 419–442. https://doi.org/10.1021/cr050359b.

Morris, K. F.; Cutak, B. J.; Dixon, A. M.; Larive, C. K. Analysis of Diffusion Coefficient Distributions in Humic and Fulvic Acids by Means of Diffusion Ordered NMR Spectroscopy. *Anal. Chem.* **1999**, *71* (23), 5315–5321. https://doi.org/10.1021/ac9907585.

Munday, R.; Thomas, K.; Gibbs, R.; Murphy, C.; Quilliam, M. A. Acute Toxicities of Saxitoxin, Neosaxitoxin, Decarbamoyl Saxitoxin and Gonyautoxins 1&4 and 2&3 to Mice by Various Routes of Administration. *Toxicon* **2013**, *76*, 77–83. https://doi.org/10.1016/j.toxicon.2013.09.013.

Nakatani, N.; Ueda, M.; Shindo, H.; Takeda, K.; Sakugawa, H. Contribution of the Photo-Fenton Reaction to Hydroxyl Radical Formation Rates in River and Rain Water Samples. *ANAL. SCI.* 2007, *23* (9), 1137–1142. https://doi.org/10.2116/analsci.23.1137.

Natumi, R.; Dieziger, C.; Janssen, E. M.-L. Cyanobacterial Toxins and Cyanopeptide Transformation Kinetics by Singlet Oxygen and PH-Dependence in Sunlit Surface Waters. *Environ. Sci. Technol.* **2021**, *55* (22), 15196–15205. https://doi.org/10.1021/acs.est.1c04194.

Nebbioso, A.; Piccolo, A. Molecular Characterization of Dissolved Organic Matter (DOM): A Critical Review. *Anal. Bioanal. Chem.* **2013**, *405* (1), 109–124. https://doi.org/10.1007/s00216-012-6363-2.

Neta, P, and Dorfman, L M. Pulse Radiolysis Studies. XIII. Rate Constants for the Reaction of Hydroxyl Radicals with Aromatic Compounds in Aqueous Solutions. *Advan. Chem. Ser.* **1968**, *81*, 222-230. https://doi:10.1021/ba-1968-0081.ch015.

Newcombe, G.; Nicholson, B. Treatment Options for the Saxitoxin Class of Cyanotoxins. *Water Supply* **2002**, *2* (5–6), 271–275. https://doi.org/10.2166/ws.2002.0179.

Ni, J.; Pignatello, J. J. Charge-Assisted Hydrogen Bonding as a Cohesive Force in Soil Organic Matter: Water Solubility Enhancement by Addition of Simple Carboxylic Acids. *Environ. Sci. Process. Impacts* **2018**, *20* (9), 1225–1233. https://doi.org/10.1039/C8EM00255J.

Nicholson, B. C.; Shaw, G. R.; Morrall, J.; Senogles, P. -J.; Woods, T. A.; Papageorgiou, J.; Kapralos, C.; Wickramasinghe, W.; Davis, B. C.; Eaglesham, G. K.; Moore, M. R. Chlorination for Degrading Saxitoxins (Paralytic Shellfish Poisons) in Water. *Environmental Technology* **2003**, *24* (11), 1341–1348. https://doi.org/10.1080/09593330309385678.

Norris, K. E.; Kurtz, T.; Wang, S.; Zeng, T.; Leresche, F.; Rosario-Ortiz, F. L. Photochemical Degradation of Saxitoxins in Surface Waters. *ACS EST Water* **2024**. https://doi.org/10.1021/acsestwater.3c00281.

O'Neil, J. M.; Davis, T. W.; Burford, M. A.; Gobler, C. J. The Rise of Harmful Cyanobacteria Blooms: The Potential Roles of Eutrophication and Climate Change. *Harmful Algae* **2012**, *14*, 313–334. https://doi.org/10.1016/j.hal.2011.10.027.

Orr, P. T.; Jones, G. J.; Hamilton, G. R. Removal of Saxitoxins from Drinking Water by Granular Activated Carbon, Ozone and Hydrogen Peroxide—Implications for Compliance with the Australian Drinking Water Guidelines. *Water Research* **2004**, *38* (20), 4455–4461. https://doi.org/10.1016/j.watres.2004.08.024.

Packer, J. L.; Werner, J. J.; Latch, D. E.; McNeill, K.; Arnold, W. A. Photochemical fate of pharmaceuticals in the environment: Naproxen, diclofenac, clofibric acid, and ibuprofen. *Aquatic Sciences* **2003** *65*(4), 342–351. https://doi.org/10.1007/s00027-003-0671-8

Paerl, H. W.; Otten, T. G. Harmful Cyanobacterial Blooms: Causes, Consequences, and Controls. *Microb Ecol* **2013**, *65* (4), 995–1010. https://doi.org/10.1007/s00248-012-0159-y.

Paerl, H. W.; Paul, V. J. Climate Change: Links to Global Expansion of Harmful Cyanobacteria. *Water Research* **2012**, *46* (5), 1349–1363. https://doi.org/10.1016/j.watres.2011.08.002.

Page, S. E.; Arnold, W. A.; McNeill, K. Assessing the Contribution of Free Hydroxyl Radical in Organic Matter-Sensitized Photohydroxylation Reactions. *Environ. Sci. Technol.* **2011**, *45* (7), 2818–2825. https://doi.org/10.1021/es2000694.

Pan, B.; Ghosh, S.; Xing, B. Nonideal Binding between Dissolved Humic Acids and Polyaromatic Hydrocarbons. *Environ. Sci. Technol.* **2007**, *41* (18), 6472–6478. https://doi.org/10.1021/es070790d.

Pan, B.; Ning, P.; Xing, B. Part IV—Sorption of Hydrophobic Organic Contaminants. *Environ. Sci. Pollut. Res.* **2008**, *15* (7), 554–564. https://doi.org/10.1007/s11356-008-0051-y.

Park, J.A.; Yang, B.; Jang, M., Kim, J.H.; Kim, S.B.; Park, H.D.; Choi, J.W. Oxidation and molecular properties of microcystin-LR, microcystin-RR and anatoxin-a using UV-light-emitting diodes at 255 nm in combination with H2O2. *Chemical Engineering* **2019** *366*, 423–432. doi:10.1016/j.cej.2019.02.101.

Pavlik, J. W.; Perdue, E. M. Number-Average Molecular Weights of Natural Organic Matter, Hydrophobic Acids, and Transphilic Acids from the Suwannee River, Georgia, as Determined Using Vapor Pressure Osmometry. *Environ. Eng. Sci.* **2015**, *32* (1), 23–30. https://doi.org/10.1089/ees.2014.0269.

Payne, E. M.; Liu, B.; Mullen, L.; Linden, K. G. UV 222 Nm Emission from KrCl* Excimer Lamps Greatly Improves Advanced Oxidation Performance in Water Treatment. *Environ. Sci. Technol. Lett.* **2022**, *9* (9), 779–785. https://doi.org/10.1021/acs.estlett.2c00472.

Perdue, E. M.; Ritchie, J. D. 5.10 - Dissolved Organic Matter in Freshwaters. In *Treatise on Geochemistry*; Holland, H. D., Turekian, K. K., Eds.; Pergamon: Oxford, 2003; pp 273–318. https://doi.org/10.1016/B0-08-043751-6/05080-5.

Petrov, D.; Tunega, D.; Gerzabek, M. H.; Oostenbrink, C. Molecular Dynamics Simulations of the Standard Leonardite Humic Acid: Microscopic Analysis of the Structure and Dynamics. *Environ. Sci. Technol.* **2017**, *51* (10), 5414–5424. https://doi.org/10.1021/acs.est.7b00266.

Peuravuori, J. NMR Spectroscopy Study of Freshwater Humic Material in Light of Supramolecular Assembly. *Environ. Sci. Technol.* **2005**, *39* (15), 5541–5549. https://doi.org/10.1021/es050341i.

Peuravuori, J.; Bursáková, P.; Pihlaja, K. ESI-MS Analyses of Lake Dissolved Organic Matter in Light of Supramolecular Assembly. *Anal. Bioanal. Chem.* **2007**, *389* (5), 1559–1568. https://doi.org/10.1007/s00216-007-1553-z.

Piccolo, A. The supramolecular structure of humic substances. *Soil Sci.* **2001** *166*, 810–832. https://doi.org/10.1097/00010694-200111000-00007.

Piccolo, A.; Nardi, S.; Concheri, G. Micelle-Like Conformation of Humic Substances as Revealed by Size-Exclusion Chromatography. *Chemosphere* **1996**, *33* (4), 595-602.

Qian, J; Mopper, K; Kieber, D.J. Photochemical production of the hydroxyl radical in Antarctic waters. *Deep. Sea. Res. Part I: Oceanogr. Res. Pap.* **2001,** *48*(3):741–759. https://doi.org/10.1016/S0967-0637(00)00068-6

Quilliam, M.A., Janeček, M. and Lawrence, J.F. Characterization of the oxidation products of paralytic shellfish poisoning toxins by liquid chromatography/mass spectrometry. *Rapid Commun. Mass Spectrom.* **1993,** *7*, 482-487. https://doi.org/10.1002/rcm.1290070616

Ralston, E. P.; Kite-Powell, H.; Beet, A. An Estimate of the Cost of Acute Food and Water Borne Health Effects from Marine Pathogens and Toxins in the United States. *J Water Health* **2011**, *9* (4), 680–694. https://doi.org/10.2166/wh.2011.157.

Recommendations for Public Water Systems to Manage Cyanotoxins in Drinking Water. U.S. EPA. https://www.epa.gov/sites/default/files/2017-06/documents/cyanotoxin-management-drinking-water.pdf (accessed 2025-03-03).

Reemtsma, T.; These, A.; Springer, A.; Linscheid, M. Differences in the Molecular Composition of Fulvic Acid Size Fractions Detected by Size-Exclusion Chromatography–on Line Fourier Transform Ion Cyclotron Resonance (FTICR–) Mass Spectrometry. *Water Res.* **2008**, *42* (1–2), 63–72. https://doi.org/10.1016/j.watres.2007.06.063.

Remke, S. C.; Bürgin, T. H.; Ludvíková, L.; Heger, D.; Wenger, O. S.; von Gunten, U.; Canonica, S. Photochemical Oxidation of Phenols and Anilines Mediated by Phenoxyl Radicals in Aqueous Solution. *Water Research* **2022**, *213*, 118095. https://doi.org/10.1016/j.watres.2022.118095.

Remke, S. C.; von Gunten, U.; Canonica, S. Enhanced transformation of aquatic organic compounds by long-lived photooxidants (LLPO) produced from dissolved organic matter. *Water Research* **2021**, *190*, 116707. https://doi.org/10.1016/j.watres.2020.116707

Remucal, C. K. The Role of Indirect Photochemical Degradation in the Environmental Fate of Pesticides: A Review. *Environ. Sci.: Processes Impacts* **2014**, *16* (4), 628. https://doi.org/10.1039/c3em00549f.

Reuter, J. H.; Perdue, E. M. Calculation of Molecular Weights of Humic Substances from Colligative Data: Application to Aquatic Humus and Its Molecular Size Fractions. *Geochim. Cosmochim. Acta* **1981**, *45* (11), 2017–2022. https://doi.org/10.1016/0016-7037(81)90056-9.

Ritchie, J. D.; Perdue, E. M. Proton-Binding Study of Standard and Reference Fulvic Acids, Humic Acids, and Natural Organic Matter. *Geochimica et Cosmochimica Acta* **2003**, *67* (1), 85–96. https://doi.org/10.1016/S0016-7037(02)01044-X.

Rizzuto, S.; Baho, D. L.; Jones, K. C.; Zhang, H.; Leu, E.; Nizzetto, L. Binding of Waterborne Pharmaceutical and Personal Care Products to Natural Dissolved Organic Matter. *Sci. Total Environ.* **2021**, *784*, 147208. https://doi.org/10.1016/j.scitotenv.2021.147208.

Rogers, R.S., & Rapoport, H. The pKa's of saxitoxin. *Journal of the American Chemical Society* **1980**, *102*, 7335-7339. https://doi.org/10.1021/JA00544A030

Rositano, J.; Nicholson, B.C.; Pieronne, P. Destruction of Cyanobacterial Toxins By Ozone. *Ozone: Science & Engineering* **1998**, 20(3), 223 238. https://doi.org/10.1080/01919519808547273

Rositano, J.; Newcombe, G.; Nicholson, B.; Sztajnbok, P. Ozonation of Nom and Algal Toxins in Four Treated Waters. *Water Research* **2001**, *35* (1), 23–32. https://doi.org/10.1016/S0043-1354(00)00252-9.

Rostad, C. E.; Leenheer, J. A. Factors That Affect Molecular Weight Distribution of Suwannee River Fulvic Acid as Determined by Electrospray Ionization/Mass Spectrometry. *Anal. Chim. Acta* **2004**, *523* (2), 269–278. https://doi.org/10.1016/j.aca.2004.06.065.

Schmitt, M.; Erickson, P. R.; McNeill, K., Triplet-State Dissolved Organic Matter Quantum Yields and Lifetimes from Direct Observation of Aromatic Amine Oxidation. Environ. Sci. Technol. 2017, 51 (22), 13151-13160

Schwarzenbach, R.P., Gschwend, P.M. and Imboden, D.M. *Environmental organic chemistry*, 3rd Ed. John Wiley & Sons, 2016.

Schweitzer, C.; Mehrdad, Z.; Noll, A.; Grabner, E.-W.; Schmidt, R. Mechanism of Photosensitized Generation of Singlet Oxygen during Oxygen Quenching of Triplet States and the General Dependence of the Rate Constants and Efficiencies of O2(1Σg+), O2(1Δg), and O2(3Σg-) Formation on Sensitizer Triplet State Energy and Oxidation Potential. *J. Phys. Chem. A* 2003, *107* (13), 2192–2198. https://doi.org/10.1021/jp026189d.

Sharpless, C. M. Lifetimes of Triplet Dissolved Natural Organic Matter (DOM) and the Effect of NaBH4 Reduction on Singlet Oxygen Quantum Yields: Implications for DOM Photophysics. *Environ. Sci. Technol.* **2012**, *46* (8), 4466–4473. https://doi.org/10.1021/es300217h.

Sleighter, R. L.; Hatcher, P. G. The Application of Electrospray Ionization Coupled to Ultrahigh Resolution Mass Spectrometry for the Molecular Characterization of Natural Organic Matter. *J. Mass Spectrom.* **2007**, *42* (5), 559–574. https://doi.org/10.1002/jms.1221.

Šmejkalová, D.; Piccolo, A. Aggregation and Disaggregation of Humic Supramolecular Assemblies by NMR Diffusion Ordered Spectroscopy (DOSY-NMR). *Environ. Sci. Technol.* **2008**, *42* (3), 699–706. https://doi.org/10.1021/es071828p.

Stenson, A. C.; Marshall, A. G.; Cooper, W. T. Exact Masses and Chemical Formulas of Individual Suwannee River Fulvic Acids from Ultrahigh Resolution Electrospray Ionization Fourier Transform Ion Cyclotron Resonance Mass Spectra. *Anal. Chem.* **2003**, *75* (6), 1275–1284. https://doi.org/10.1021/ac026106p.

Stevenson, F. J. *Humus Chemistry: Genesis, Composition, Reactions*, 2nd ed.; John Wiley & Sons: New York, 1994.

Stratakis, M. & Orfanopoulos, M. Regioselectivity in the ene reaction of singlet oxygen with alkenes bearing an electron withdrawing group at β- position. *Tetrahedron Letters* **1997**, *38* (6), 1067-1070. https://doi.org/10.1016/S0040-4039(96)02469-0

Swain, M. Chemicalize. *Org. J. Chem. Inf. Model.* **2012**, *52*, 613– 615, https://doi.org/10.1021/ci300046g

Swift, R. S. Organic Matter Characterization. *SSSA Book Ser.* **1996**, 1011.

Tang, T.; Hoefel, D.; Mosisch, T.; Ho, L. Assessing the Fate and Biodegradation of Cyanobacterial Metabolites in Australian Waters. *Water Practice and Technology* **2012**, *7* (4). https://doi.org/10.2166/wpt.2012.064.

Thurman, E. M. *Organic Geochemistry of Natural Waters*; Springer Netherlands: Dordrecht, 1985. https://doi.org/10.1007/978-94-009-5095-5.

Thurman, E. M.; Malcolm, R. L. Preparative Isolation of Aquatic Humic Substances. *Environ. Sci. Technol.* **1981**, *15* (4), 463–466. https://doi.org/10.1021/es00086a012.

Trout, C. C.; Kubicki, J. D. Deprotonation Energies of a Model Fulvic Acid. I. Carboxylic Acid Groups. *Geochim. Cosmochim. Acta* **2006**, *70* (1), 44–55. https://doi.org/10.1016/j.gca.2005.08.017.

Vialykh, E. A.; Salahub, D. R.; Achari, G.; Cook, R. L.; Langford, C. H. Emergent Functional Behaviour of Humic Substances Perceived as Complex Labile Aggregates of Small Organic Molecules and Oligomers. *Environ. Chem.* **2019**, *16* (7), 505–516. https://doi.org/10.1071/EN19095.

Vialykh, E. A.; McKay, G.; Rosario-Ortiz, F. L. Computational Assessment of the Three-Dimensional Configuration of Dissolved Organic Matter Chromophores and Influence on Absorption Spectra. *Environ. Sci. Technol.* **2020**, *54* (24), 15904–15913. https://doi.org/10.1021/acs.est.0c05860.

Vione, D.; Falletti, G.; Maurino, V.; Minero, C.; Pelizzetti, E.; Malandrino, M.; Ajassa, R.; Olariu, R.-I.; Arsene, C. Sources and Sinks of Hydroxyl Radicals upon Irradiation of Natural Water Samples. *Environ. Sci. Technol.* **2006**, *40* (12), 3775–3781. https://doi.org/10.1021/es052206b.

Vione, D.; Minella, M.; Maurino, V.; Minero, C. Indirect Photochemistry in Sunlit Surface Waters: Photoinduced Production of Reactive Transient Species. *Chem. Eur. J.* **2014**, *20* (34), 10590–10606. https://doi.org/10.1002/chem.201400413.

Vione, D.; Fabbri, D.; Minella, M.; Canonica, S. Effects of the antioxidant moieties of dissolved organic matter on triplet-sensitized phototransformation processes: Implications for the photochemical modeling of sulfadiazine. *Water Research* **2018**, 128, 38-48. https://doi.org/10.1016/j.watres.2017.10.020

Voelker, B. M.; Morel, F. M. M.; Sulzberger, B. Iron Redox Cycling in Surface Waters: Effects of Humic Substances and Light. *Environ. Sci. Technol.* **1997**, *31* (4), 1004–1011. https://doi.org/10.1021/es9604018.

von Sonntag, J.; Mvula, E.; Hildenbrand, K.; von Sonntag, C. Photohydroxylation of 1,4-Benzoquinone in Aqueous Solution Revisited. *Chem. Eur. J.* **2004**, 10, 440-451 https://doi.10.1002/chem.200305136

Wan, D.; Wang, J.; Dionysiou, D. D.; Kong, Y.; Yao, W.; Selvinsimpson, S.; Chen, Y. Photogeneration of Reactive Species from Biochar-Derived Dissolved Black Carbon for the Degradation of Amine and Phenolic Pollutants. *Environ. Sci. Technol.* **2021**, *55* (13), 8866–8876. https://doi.org/10.1021/acs.est.1c01942.

Wang, Z.; Nagata, M.; Murano, H.; Pignatello, J. J. Participation of Strong Charge-Assisted Hydrogen Bonds in Interactions of Dissolved Organic Matter. *Water Research* **2024**. https://doi.org/10.1016/j.watres.2024.122274.
Wang, L.; Cao, J.; Wang, P.; Fu, Y.; Chen, J.; Wang, Z. Hydroperoxide-Independent Generation of Spin Trapping Artifacts by Quinones and DMPO: Implications for Radical Identification in Quinone-Related Reactions. *Environ. Health* **2024**, envhealth.4c00142. https://doi.org/10.1021/envhealth.4c00142.

Wells, M. J. M. Supramolecular Answers to the Organic Matter Controversy. *J. Environ. Qual.* **2019**, *48* (6), 1644–1651. https://doi.org/10.2134/jeq2019.02.0089.

Wells, M. J. M.; Stretz, H. A. Supramolecular Architectures of Natural Organic Matter. *Sci. Total Environ.* **2019**, *671*, 1125–1133. https://doi.org/10.1016/j.scitotenv.2019.03.406.

Wenk, J., & Canonica, S. Phenolic antioxidants inhibit the triplet-induced transformation of anilines and sulfonamide antibiotics in aqueous solution. *Environmental Science and Technology* **2012**, *46*(10), 5455–5462. https://doi.org/10.1021/es300485u

Wenk, J., von Gunten, U., Canonica, S., 2011. Effect of dissolved organic matter on the transformation of contaminants Induced by excited triplet states and the hydroxyl radical. Environ. Sci. Technol. 45(4), 1334-1340.

Wershaw, R. Model for Humus in Soils and Sediments. *Environ. Sci. Technol.* **1993**, *27* (5), 814–816. https://doi.org/10.1021/es00042a603.

Westerhoff, P.; Mezyk, S. P.; Cooper, W. J.; Minakata, D. Electron Pulse Radiolysis Determination of Hydroxyl Radical Rate Constants with Suwannee River Fulvic Acid and Other Dissolved Organic Matter Isolates. *Environ. Sci. Technol.* **2007**, *41* (13), 4640–4646. https://doi.org/10.1021/es062529n.

Wiese, M.; D'Agostino, P. M.; Mihali, T. K.; Moffitt, M. C.; Neilan, B. A. Neurotoxic Alkaloids: Saxitoxin and Its Analogs. *Mar Drugs* **2010**, *8* (7), 2185–2211. https://doi.org/10.3390/md8072185.

Wilkinson, F.; Helman, W. P.; Ross, A. B. Quantum Yields for the Photosensitized Formation of the Lowest Electronically Excited Singlet State of Molecular Oxygen in Solution. *Journal of Physical and Chemical Reference Data* **1993**, *22*(1), 113–262. https://doi.org/10.1063/1.555934

Wu, B.; Arnold, W. A.; Ma, L. Photolysis of Atrazine: Role of Triplet Dissolved Organic Matter and Limitations of Sensitizers and Quenchers. *Water Research* **2021**, *190*, 116659. https://doi.org/10.1016/j.watres.2020.116659.

Wurtsbaugh, W. A.; Paerl, H. W.; Dodds, W. K. Nutrients, Eutrophication and Harmful Algal Blooms along the Freshwater to Marine Continuum. *WIREs Water* **2019**, *6* (5), e1373. https://doi.org/10.1002/wat2.1373.

Xu, J.; Huang, C.-H. Enhanced Direct Photolysis of Organic Micropollutants by Far-UVC Light at 222 Nm from KrCl* Excilamps. *Environ. Sci. Technol. Lett.* **2023**, *10* (6), 543–548. https://doi.org/10.1021/acs.estlett.3c00313.

Yakimov, B. P.; Rubekina, A. A.; Budylin, G. S.; Zherebker, A. Y.; Kompanets, V. O.; Chekalin, S. V.; Vainer, Y. G.; Fadeev, V. V.; Gorbunov, M. Y.; Perminova, I. V.; Shirshin, E. A. Ultrafast Energy Transfer Determines the Formation of Fluorescence in DOM and Humic Substances. *Environ. Sci. Technol.* **2021**, *55* (15), 10365–10377. https://doi.org/10.1021/acs.est.1c00998.

Yan, S.; Sun, J.; Sha, H.; Li, Q.; Nie, J.; Zou, J.; Chu, C.; Song, W. Microheterogeneous Distribution of Hydroxyl Radicals in Illuminated Dissolved Organic Matter Solutions. *Environ. Sci. Technol.* **2021**, *55* (15), 10524–10533. https://doi.org/10.1021/acs.est.1c03346.
Zafiriou, O. C.; Joussot-Dubien, J.; Zepp, R. G.; Zika, R. G. Photochemistry of Natural Waters. *Environ. Sci. Technol.* **1984**, *18* (12), 358A-371A. https://doi.org/10.1021/es00130a711.

Zepp, R. G.; Schlotzhauer, P. F.; Sink, R. Merritt. Photosensitized Transformations Involving Electronic Energy Transfer in Natural Waters: Role of Humic Substances. *Environ. Sci. Technol.* **1985**, *19* (1), 74–81. https://doi.org/10.1021/es00131a008.

Zepp, R. G.; Hoigne, Juerg.; Bader, Heinz. Nitrate-Induced Photooxidation of Trace Organic Chemicals in Water. *Environ. Sci. Technol.* **1987**, *21* (5), 443–450. https://doi.org/10.1021/es00159a004.

Zepp, R. G.; Gumz, M. M.; Miller, W. L.; Gao, H. Photoreaction of Valerophenone in Aqueous Solution. *J. Phys. Chem. A* **1998**, *102* (28), 5716–5723. https://doi.org/10.1021/jp981130l.

Zhao, J.; Payne, E. M.; Liu, B.; Shang, C.; Blatchley, E. R.; Mitch, W. A.; Yin, R. Making Waves: Opportunities and Challenges of Applying Far-UVC Radiation in Controlling Micropollutants in Water. *Water Research* **2023**, *241*, 120169. https://doi.org/10.1016/j.watres.2023.120169.

Zhao, J.; Zhou, Y.; Li, C.; Xie, Q.; Chen, J.; Chen, G.; Peijnenburg, W. J. G. M.; Zhang, Y.; Qu, J. Development of a Quantitative Structure-Activity Relationship Model for Mechanistic Interpretation and Quantum Yield Prediction of Singlet Oxygen Generation from Dissolved Organic Matter. *Science of The Total Environment* **2020**, *712*, 136450. https://doi.org/10.1016/j.scitotenv.2019.136450.

Zhou, L.; Ji, Y.; Zeng, C.; Zhang, Y.; Wang, Z.; Yang, X. Aquatic Photodegradation of Sunscreen Agent P-Aminobenzoic Acid in the Presence of Dissolved Organic Matter. *Water Research* **2013**, *47* (1), 153–162. https://doi.org/10.1016/j.watres.2012.09.045.

Zhou, X.; Mopper, K. Determination of Photochemically Produced Hydroxyl Radicals in Seawater and Freshwater. *Marine Chemistry* **1990**, *30*, 71–88. https://doi.org/10.1016/0304-4203(90)90062-H.

Appendices

Appendix A. Supplemental Information for Chapter 3: Unraveling the Mechanisms of Hydroxyl Radical Production by Dissolved Organic Matter Model Photosensitizers

Table A.1 Reactions potentially involved in the photochemical production of hydroxyl radicals by dissolved organic matter (DOM).

$O_2^{\bullet-}$ / $HO_2^{\bullet}$ dismutation and H_2O_2 photolysis
$O_2^{\bullet-} + H^+ \rightarrow HO_2^{\bullet}$
$HO_2^{\bullet} + O_2^{\bullet-} \rightarrow HO_2^- + O_2$
$HO_2^- + H^+ \rightarrow H_2O_2$
$H_2O_2 + h\nu \rightarrow {}^{\bullet}OH$
$Fe^{2+} + H_2O_2 \rightarrow Fe^{3+} + {}^{\bullet}OH + OH^-$

Reactions generating $O_2^{\bullet-}$ / $HO_2^{\bullet}$
$DOM + h\nu \rightarrow DOM' + e^-$
$e^- + O_2 \rightarrow O_2^{\bullet-}$
$H^{\bullet} + O_2 \rightarrow HO_2^{\bullet}$
$^3DOM^* + S \rightarrow DOM^{\bullet-} + S^+$
$DOM^{\bullet-} + O_2 \rightarrow O_2^{\bullet-}$
$^3DOM^* + O_2 \rightarrow DOM^{\bullet+} + O_2^{\bullet-}$
[a]S = electron donor

Photo-dissociation reactions
$DOM + h\nu \rightarrow {}^{\bullet}OH + DOM'$
$DOM + h\nu \rightarrow H^{\bullet} + DOM'$

Oxidation of water/hydroxide
$^1DOM^* + H_2O/OH^- \rightarrow DOM^{\bullet-} + H^+ + {}^{\bullet}OH$
$^3DOM^* + H_2O/OH^- \rightarrow DOM^{\bullet-} + H^+ + {}^{\bullet}OH$

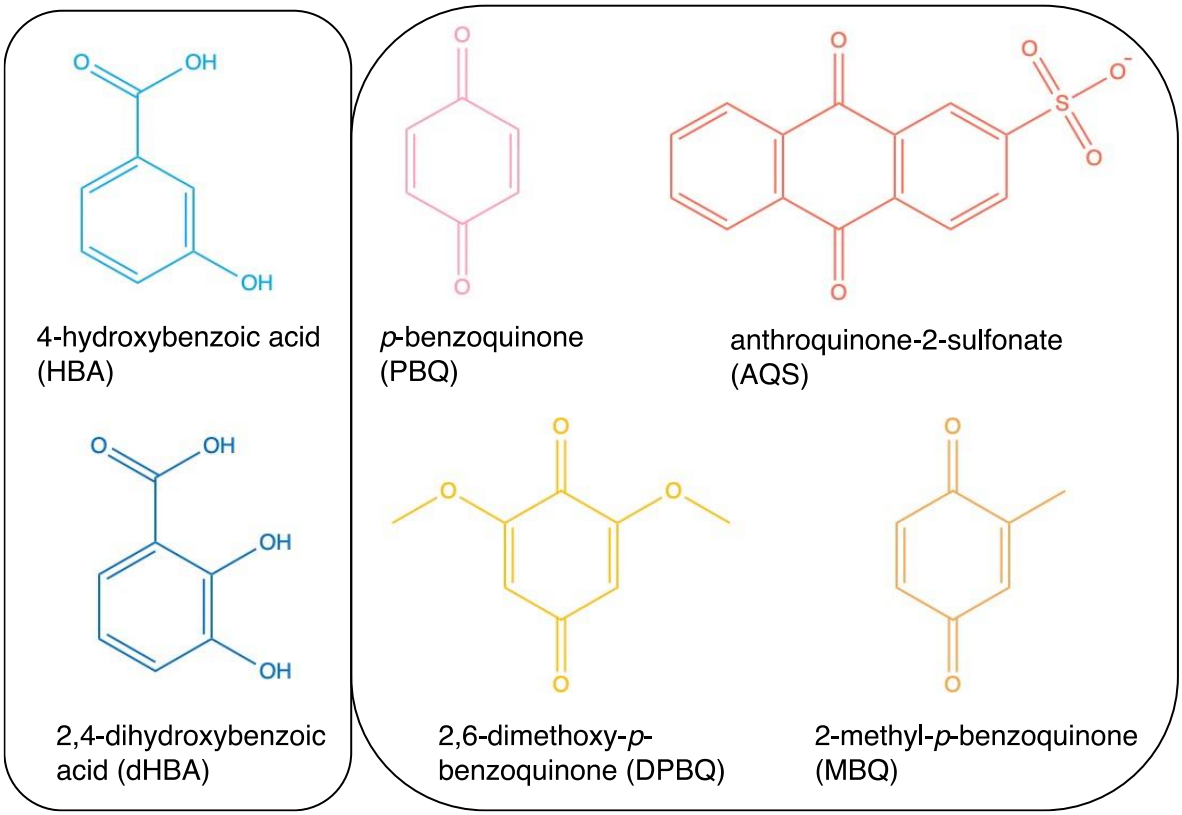

Figure A.1 Model photosensitizers examined in this study.

Table A.2 Chemicals used in this research.

Chemical	**Producer**	**CAS**
Acetonitrile	VWR	75-05-8
Anthroquinone-2-sulfonate	EMD	131-08-8
Benzoic acid	Alfa Aesar	65-85-0
Catalase	Sigma-Aldrich	9001-05-2
2,4-dihydroxybenzoic acid	Aldrich	89-86-1
2,6-dimethoxy-*p*-benzoquinone	Alfa Aesar	530-55-2
Furfuryl alchohol (98%)	TCI America	98-00-0
Hydrogen peroxide (30%)	Supelco	7722-84-1
4-hydroxybenzoic acid	Aldrich	99-96-7
2-hydroxyterephthalic acid	Sigma-Aldrich	636-94-2
Methanol	VWR	67-56-1
methyl-*p*-benzoquinone	Aldrich	553-97-9
p-benzoquinone	Alfa Aesar	106-51-4
p-nitroanisole	Aldrich	100-17-4
Salicylic acid	EMD	69-72-7
Phosphoric acid	Fisher Chemical	7664-38-2
Pyridine	Mallinckrodt	110-86-1
Sodium nitrite	Sigma-Aldrich	7632-00-0
Sodium phosphate dibasic dihydrate (98%)	Fisher Chemical	10028-24-7
Sodium phosphate monobasic dihydrate (99%)	Fisher Chemical	13472-35-0
Sodium terephthalate	Pfaltz and Bauer	100-21-0
Uridine	Sigma	58-96-8

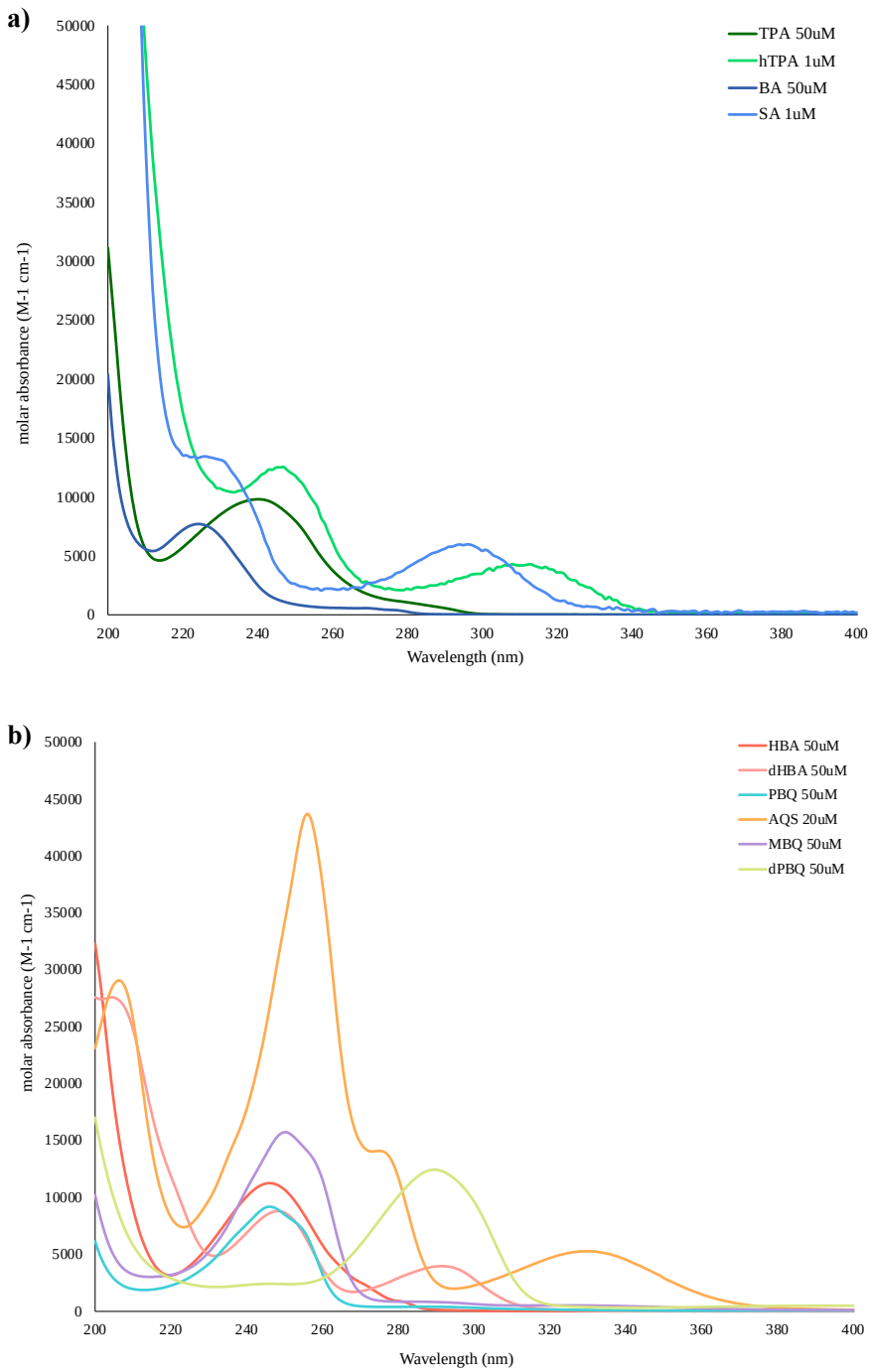

Figure A.2 UV-visible spectra of (a) probe compounds, terephthalic acid (TPA) and benzoic acid (BA) and their transformation products, hydroxyterephthalic acid (hTPA) and salicylic acid (SA) and (b) model photosensitizers. (HBA=4-hydroxybenzoic acid, DHBA=2,4-dihydroxybenzoic acid, PBQ=*p*-benzoquinone, AQS-anthroquinone-2-sulfonate, MBQ=methyl-*p*-benzoquinone, DPBQ=dimethoxy-*p*-benzoquinone).

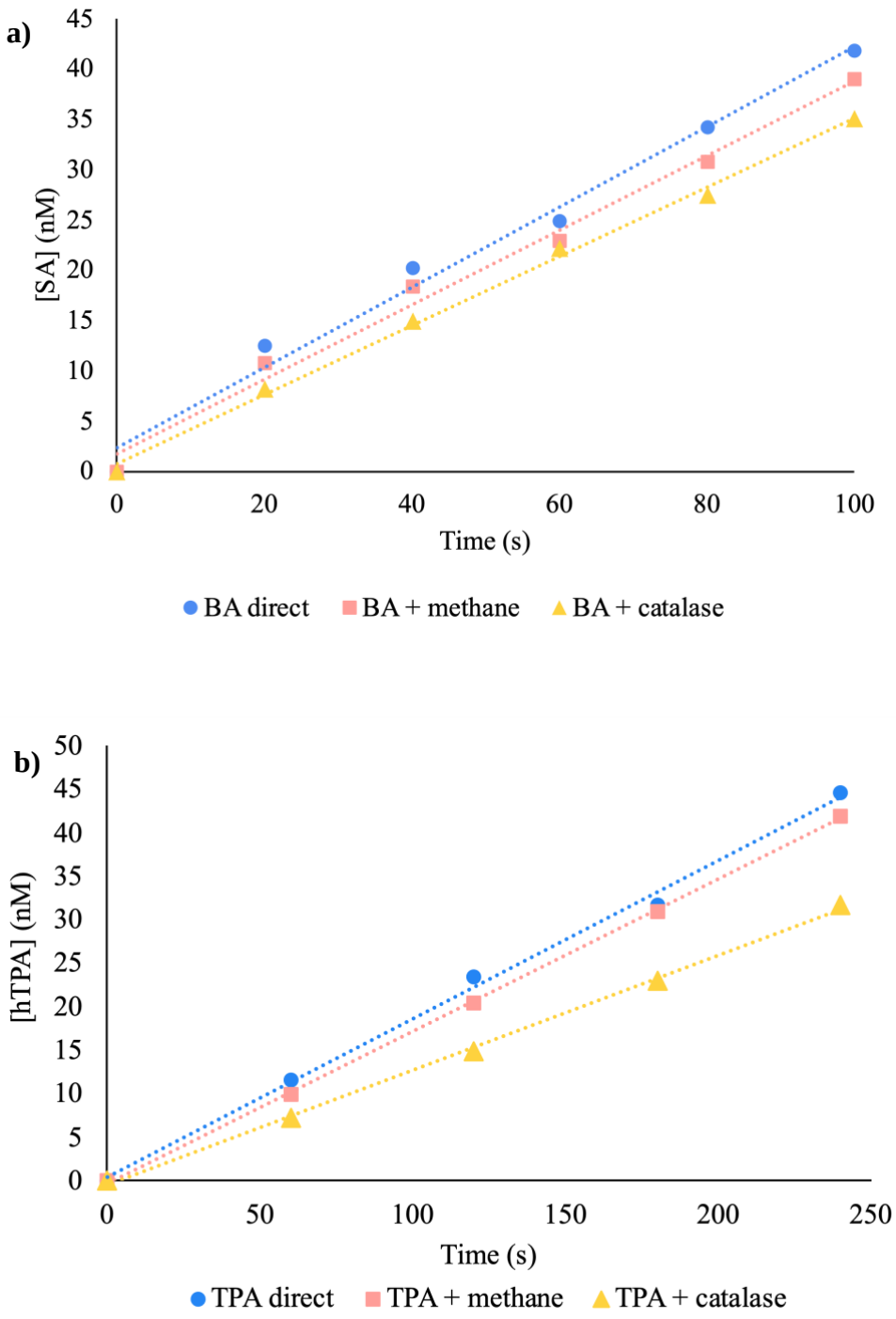

Figure A.3 Rates of direct photolysis of probe compounds alone and in the presence of 8.43 × 104 M methane or 40 units mL-1 catalase. The transformations of a) benzoic acid (BA) to salicylic acid (SA) at 254 nm and b) terephthalic acid (TPA) to hydroxyterephthalic acid (htPA) at 300 nm are shown.

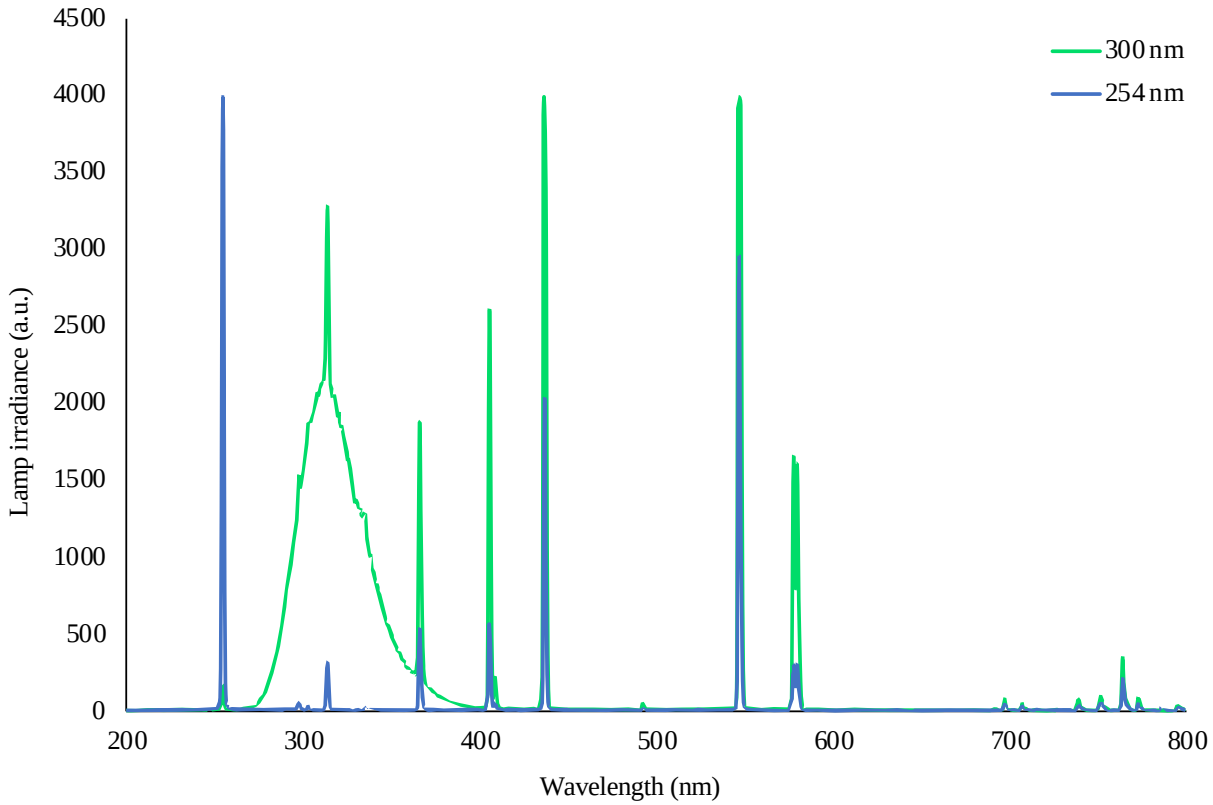

Figure A.4 Emission spectra of Rayonet reactor 254 and 300 nm LED lamps measured using an Ocean Optics USB2000 spectrometer.

Text A.1 PNA/pyridine and uridine actinometry methods.

The photon fluence rate, E_p^0 (units of mol m^{-2} s^{-1}), for experiments using the 300 nm lamps was calculated referencing equations provided by Laszakovits et al. (2017) using the PNA/pyridine actinometry described by Equations A.1 and A.2. k_{PNA} is the measured PNA phototransformation rate constant (units of s^{-1}) quantified by HPLC (Table A.3). Φ_{PNA} is the quantum yield for PNA phototransformation (unitless, calculated using Equation A.2), $f_{p,\lambda}$ is the normalized emission spectrum of the lamp at 300 nm (unitless), and $\varepsilon_{PNA,\lambda}$ is the molar absorption coefficient at wavelength λ (units of m^2 mol^{-1}).

$$E_p^0(\lambda = 300\,nm) = \frac{k_{PNA}}{(2.303)(\Phi_{PNA,\lambda})(f_{p,\lambda})(\varepsilon_{PNA,\lambda})} \quad \text{(A.1)}$$

$$\Phi_{PNA} = 0.29[Pyr] + 0.00029 \quad \text{(A.2)}$$

For experiments using 254 nm lamps, E_p^0 was determined with uridine actinometry. The degradation rate of uridine ($k_{uridine}$; $[uridine]_0$=1.2 μM) was quantified using HPLC (Table S3) and related to E_p^0 according to Equation A.3. $\Phi_{uridine,\lambda}$ is the quantum yield for uridine phototransformation at 254 nm (0.020, Jin et al., 2006), $\varepsilon_{uridine,\lambda}$ is the molar absorption coefficient of uridine at 254 nm, 10185 M^{-1} cm^{-1} (Jin et al., 2006), and l is the pathlength of the quartz vials used in irradiation experiments (1.25 cm).

$$E_p^0(\lambda = 254\,nm) = \frac{k_{uridine}[uridine]_0 l}{1000(\Phi_{uridine,\lambda})(1-10^{-\varepsilon_{uridine,\lambda}[uridine]_0 l})} \quad \text{(A.3)}$$

Table A.3 HPLC analytical methods. The injection volume was 50 µL and flowrate was 1.0 mL min^{-1} unless otherwise noted.

Compound	Eluent	Retention Time (min)	Detection Wavelength (UV) or Excitation/Detection Wavelength (Fluorescence) (nm)	Limit of Detection (nM)[2]	Limit of Quantitation (nM)[2,3]
p-nitroanisole[1]	50% 10 mM phosphoric acid 50% acetonitrile	3.2	300	66	200
uridine	80% 10 mM phosphoric acid 20% methanol	3.6	262	27	82
salicylic acid	70% 10 mM phosphoric acid 30% acetonitrile	6.0	300/410	1.4	4.1
2-hydroxy-terephthalic acid	80% 10 mM phosphoric acid 20% acetonitrile	3.4	250/410	10.3	31.2
2,4,6-trimethylphenol	60% acetonitrile 30% DI water 10% 10 mM phosphoric acid	4.6	280	41	124

[1]Flow rate: 1.5 mL min^{-1}

[2]Determined using the standard deviation of the response and the slope method

[3]All calculations were made with data points collected above the limit of quantitation

Text A.2 Methane as a partial quencher of •OH.

Typically, quencher compounds are added to experimental solutions such that ~95% or greater of the reactive intermediate (•OH) reacts with the quencher (Equation A.4) so that the kinetic expression for $[•OH]_{ss}$ reduces to the rate of •OH formation divided by the quenching rate (Equation A.5). In these equations, $f_{Q,rct}$ is the fraction of quencher reacting with •OH, $k_{•OH,Q}$ is the second order rate constant between the quencher and •OH, $k_{•OH,S}$ is the second order rate constant between each •OH scavenger in the system (quencher compound, probe molecule, photosensitizer, etc.), and $r_{•OH}$ is the rate of •OH production.

$$f_{Q,rct} = \frac{k_{•OH,Q}[Q]}{\sum k_{•OH,S}[S]} \quad \text{(A.4)}$$

$$[•OH]_{ss} = \frac{r_{•OH}}{\sum k_{•OH,S}[S]} \approx \frac{r_{•OH}}{k_{•OH,Q}[Q]} \quad \text{(A.5)}$$

The aqueous solubility of methane at 25°C and standard atmospheric pressure (101.35 kPa) is 1.42×10^4 M (Haynes, 2013). Using Henry's law, the saturation concentration of methane was calculated to be 1.18×10^4 M at the atmospheric pressure of Boulder, CO (84 kPa). In our experimental solutions, the methane concentration was limited to 8.43×10^4 M (Figure A.5) since we needed to maintain a steady dissolved oxygen concentration. Considering the second order rate constant between CH_4 and •OH, 1.2×10^8 M^{-1} s^{-1} (Buxton et al., 1988), the quenching rate by methane at this concentration is 1.42×10^5 s^{-1}. Thus, to achieve 95% or greater quenching by methane, the collective •OH quenching by other components in the system (probe molecules and photosensitizers) must be less than 7.45×10^3 s^{-1}, which is not possible since the concentrations of BA or TPA must be high enough so that their transformation products are above the limit of detection, and the concentration of the sensitizer must be high enough to generate detectable

amounts of •OH. Therefore, the maximum quenching that could be achieved by methane was ~50% in the presence of the photosensitizers and probe compounds used in these experiments. Under these concentration limitations, the probe compounds were neither at a low or high concentration limit, thus we could not directly compare rate of •OH formation because the rate of probe transformation is influenced by the probe compound (Equation A.6). Thus, the experimental rates of SA and hTPA formation in the presence of methane ($r_{form,TP(CH_4)}$) were compared with their predicted rates ($r_{form,TP(pred.)}$) based on Equation A.7, where $k_{\bullet OH,PC}$, $k_{\bullet OH,S}$, and $k_{\bullet OH,CH_4}$ are the second-order rate constants between the probe compound, sensitizer, and methane, respectively. With the concentrations chosen in these experiments, the minimum fraction of •OH reacting with methane (Equation A.4) was 15% to be able to show significant reduction of r_{PC} by methane.

$$r_{PC} = \frac{d[PC]}{dt} = -k_{\bullet OH,PC}[\bullet OH]_{ss}[PC] \quad \text{(A.6)}$$

$$r_{form,TP(pred.)} = r_{form,TP} \times \frac{k_{\bullet OH,PC}[PC] + k_{\bullet OH,S}[S]}{k_{\bullet OH,PC}[PC] + k_{\bullet OH,S}[S] + k_{\bullet OH,CH_4}[CH_4]} \quad \text{(A.7)}$$

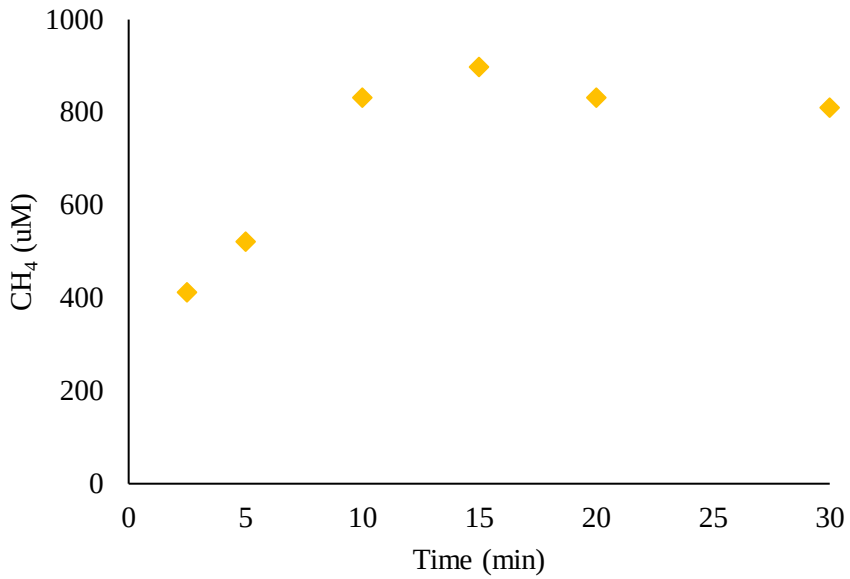

Figure A.5 Concentration of methane in solution vs time bubbling with an 80:20 CH4:O2 flow rate ratio. Concentrations converted from CO_2 concentration determined using an acidified ammonium bicarbonate standard curve. Concentrations were measured by GC-FID (see Buckley et al., 2024 for method).

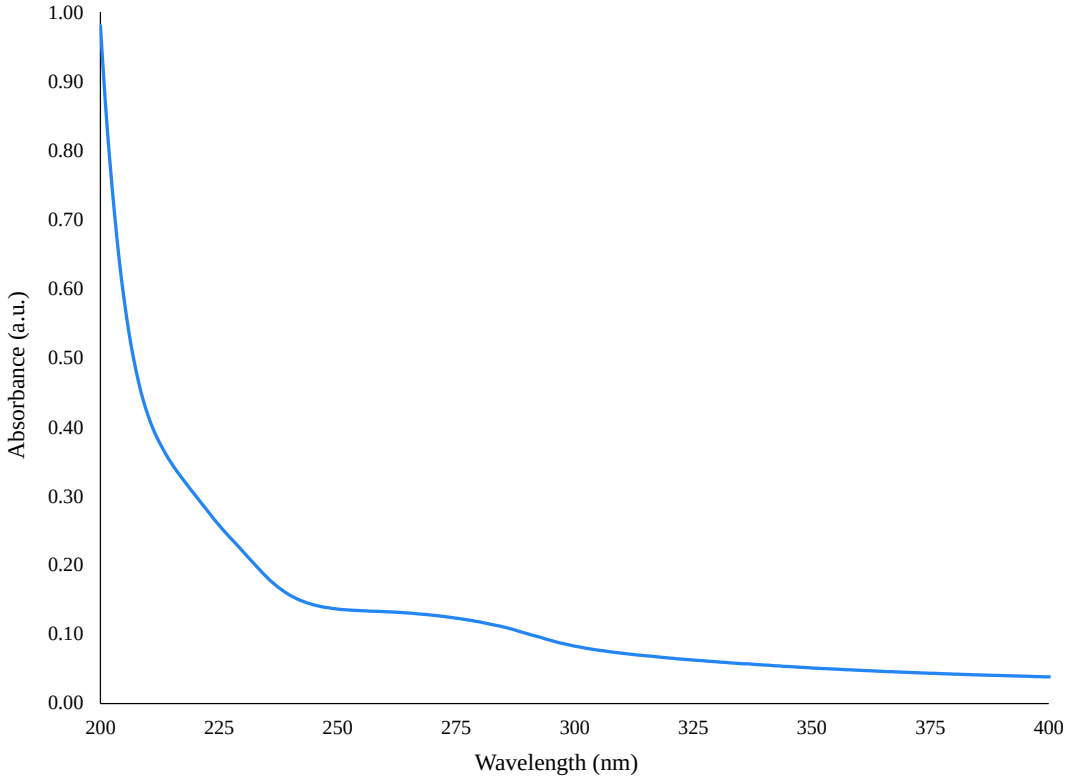

Figure A.6 UV-visible spectra of catalase (40 units mL^{-1}).

Text A.3 Pulse radiolysis determination of $k_{\bullet OH,cat}$

The rate constant between •OH and catalase ($k_{\bullet OH,cat}$) was determined using the Model TB-8/16-1S linear accelerator pulse radiolysis system at the Department of Energy Radiation Laboratory, University of Notre Dame. The electron pulse radiolysis of an aqueous solution generates •OH along with hydrated electrons and hydrogen atoms according to Equation A.8 (Buxton et al., 1988), where the numbers in brackets are the absolute yields (G-values) of each species in units of μmol per Joule.

$$H_2O \xrightarrow{radiolysis} [0.28]\ {}^{\bullet}OH + [0.28]\ e^-_{aq} + [0.06]\ H^{\bullet} + [0.07]\ H_2O_2 + [0.26]\ H_3O^+ + [0.05]\ H_2 \qquad \text{A.8}$$

To isolate the •OH radical, the catalase solutions were pre-saturated with nitrous oxide (N_2O), which converts hydrated electrons and hydrogen atoms to •OH (Buxton et al, 1988). Dosimetry was based on the transient absorbance produced by an N_2O-saturated solution of 10 mM KSCN at 475 nm using $G\epsilon$ = 5.1 x 10^{-4} m^2 J^{-1} was assumed (Buxton and Stuart, 1995) corresponding to doses of 5-6 Gy (ca. 3-4 mM) per 4 ns pulse. The quantification of $k_{\bullet OH,cat}$ was determined using a standard solution of 98.5 μM KSCN in 10 mM phosphate buffered solution at pH 7.0 $\pm$ 0.1 saturated with N_2O gas. The absorbance of the transient produced by SCN^- ($[(SCN)_2^{\bullet -}]$) was monitored in the presence of increasing concentrations of catalase to determine the ratio of $[(SCN)_2^{\bullet -}]_0$ (absorbance of the transient in the absence of catalase) to $[(SCN)_2^{\bullet -}]$. $k_{\bullet OH,cat}$was calculated using a linear regression of the plot of $[(SCN)_2^{\bullet -}]_0/[(SCN)_2^{\bullet -}]$ versus $[cat]/[SCN^-]$ according to Equation A.9, where $k_{\bullet OH,SCN^-}$ is a predetermined value of 1.1 × 10^{10} M^{-1} s^{-1} (Buxton et al., 1988).

$$\frac{[(SCN)_2^{\bullet -}]_0}{[(SCN)_2^{\bullet -}]} = 1 + \frac{k_{\bullet OH,cat}}{k_{\bullet OH,SCN^-}} \frac{[cat]}{[SCN^-]} \qquad \text{A.9}$$

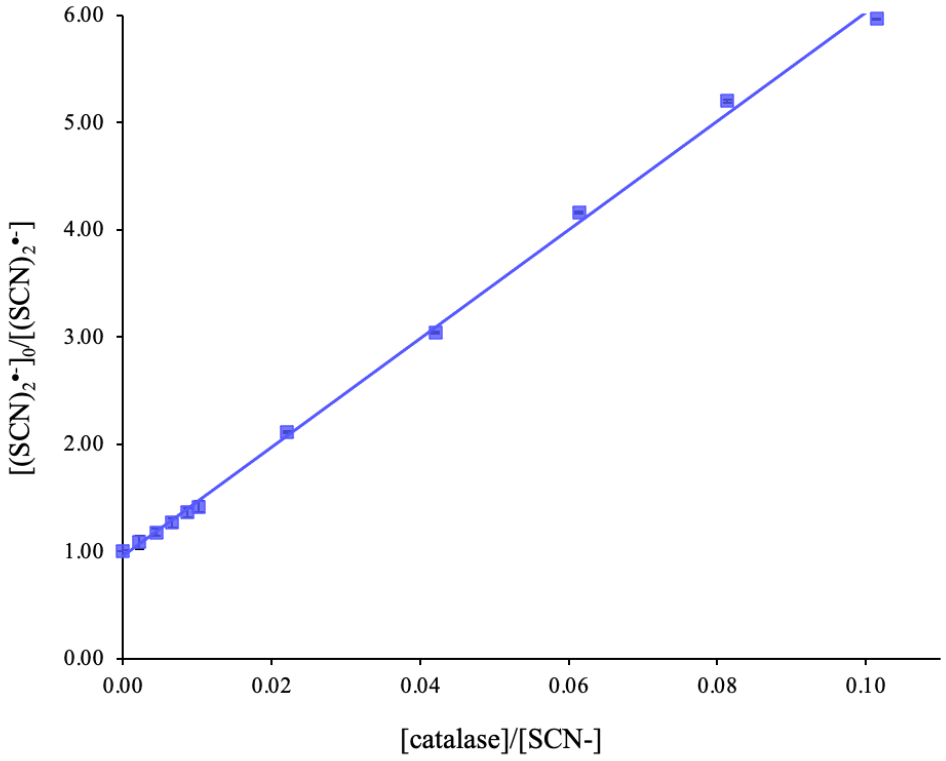

Figure A.7 Ratio of $(SCN)_2^{\bullet-}$ transient absorbance at 475 nm in a blank (98.5 μM KSCN with 10 mM phosphate buffer at pH 7.0 $\pm$ 0.1 at 22.0 ^{o}C, saturated with N_2O gas) compared to samples spiked with concentrations between 0.2-10 μM catalase ($[(SCN)_2^{\bullet-}]_0/[(SCN)_2^{\bullet-}]$). All measurements made using the linear accelerator pulse radiolysis system at the Department of Energy Radiation Laboratory, University of Notre Dame; methods outlined in Text A.3.

Text A.4 Calculation of light screening factors

A light screening factor ($S_{M,\lambda}$) was calculated for each experimental solution at both 254 nm and 300 nm according to Equation A.10 (Wenk et al., 2011). $\varepsilon_{M,\lambda}$ (M^{-1} cm^{-1}) is the wavelength specific molar absorption coefficient of molecule M (probe compound, model sensitizer, or catalase); [M] is the concentration of the probe compound, sensitizer, or catalase; l is the path length of the quartz vials used in photochemical experiments (1.25 cm).

$$S_{M,\lambda} = \frac{1 - e^{-2.303 \sum (\varepsilon_{M,\lambda}[M])l}}{2.303 \sum (\varepsilon_{M,\lambda}[M])l} \qquad \text{A.10}$$

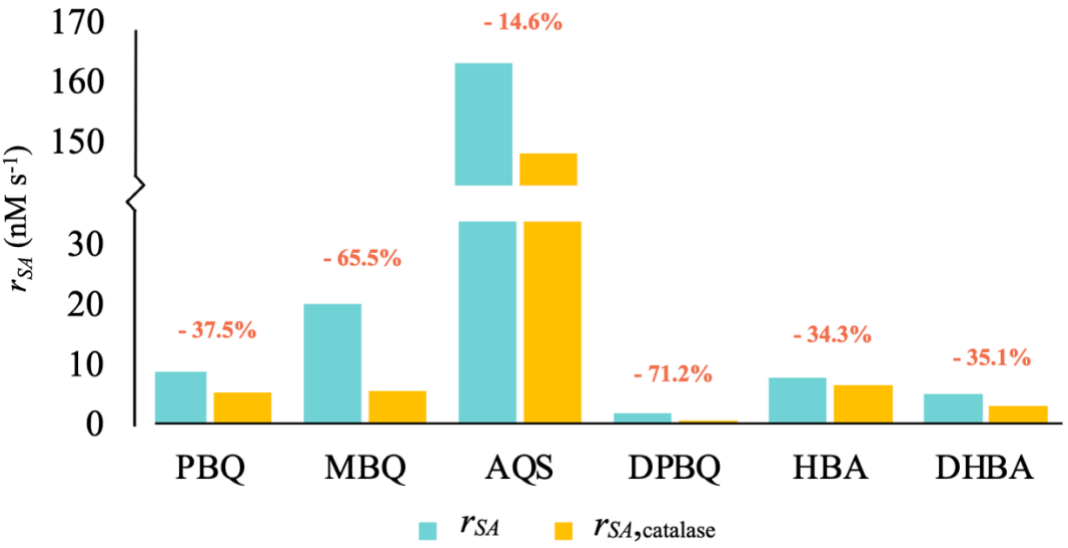

Figure A.8 Rates of salicylic acid production (r_{SA}) in the presence of model sensitizers at 254 nm in the absence (blue bars) and presence (orange bars) of catalase. At the experimental concentrations (2 mM benzoic acid, 25 μM of the model photosensitizer, and 0 or 40 units mL^{-1} catalase), > 95% of •OH react with BA to ensure that quenching of •OH by catalase is negligible. The percent reduction in r_{SA} due to the addition of catalase is displayed above the bars in red. PBQ = p-benzoquinone, AQS = anthroquinone-2-sulfonate, MBQ = methyl-p-benzoquinone, DPBQ = dimethoxy-p-benzoquinone, HBA = 4-hydroxybenzoic acid, and DHBA = 2,4-dihydroxybenzoic acid.

Text A.5 Estimated contributions of deactivation pathways for triplet state quinones in DOM

To understand the pathways leading to the formation of •OH by DOM, it is important to understand all potential deactivation pathways for the precursors to •OH and other hydroxylating species. Because triplet state quinones are believed to be precursors to hydroxylating species and have been relatively well-studied, the known rate constants between triplet state quinones ($^3Q^*$) and oxygen, water, quinones, and phenolic compounds, as well as their O_2-independent relaxation, can be used to calculate their hypothetical contributions to $^3Q^*$ deactivation at environmentally relevant concentrations. The percent contribution of each pathway was determined using Equation A.11 based on the average of several reported $^3Q^*$ rate constants and the concentrations of H_2O, O_2, and the average quinone and phenol content in Suwanee River fulvic acid (SRFA). In Equation A.11, $k_{^3Q^*,D}[D]$ represents the second order rate constant between $^3Q^*$ and H_2O, O_2, phenols, or quinones (note the O_2-independent pathway, k_d, is first-order). The concentrations and rate constants for each solute and deactivation pathway are found in Table A.4.

$$\%\,contribution = \frac{k_{^3Q^*,D}[D]}{k_d + k_{^3Q^*,O_2}[O_2] + + k_{^3Q^*,H_2O}[H_2O] + k_{^3Q^*,PheOH}[PheOH] + k_{^3Q^*,Q}[Q]} \qquad \text{A.11}$$

Table A.4 Concentrations and rate constants used for the estimated contributions of each deactivation pathway for triplet state quinones (Table 3.2 of manuscript). Suwanee River fulvic acid (SRFA) was used as a representative of dissolved organic matter (DOM) at concentrations of 2-10 $mg_C\,L^{-1}$.

	Solute concentration (M)			
Solute:	2 $mg_C\,L^{-1}$	5 $mg_C\,L^{-1}$	10 $mg_C\,L^{-1}$	**Notes**
Quinone	1.28×10^{-6}	3.20×10^{-6}	6.40×10^{-6}	Using EAC[a] of SRFA = 671 μmol e^- gHS^{-1} (Aeschbacher et al., 2012)
Phenol	5.68×10^{-5}	1.42×10^{-5}	2.84×10^{-5}	Using EDC[b] of SRFA = 1.49 mmol PheOH gHS^{-1} (average of values from Aeschbacher et al., 2012 and Ritchie & Perdue, 2003)
H_2O	55	55	55	
O_2	2.58×10^{-4}	2.58×10^{-4}	2.58×10^{-4}	Assuming air-saturated conditions
		$k_{^3Q^*,D}[D]$ (s^{-1})		
Deactivation pathway:	$k_{^3Q^*,D}$ ($M^{-1}\,s^{-1}$)	2 $mg_C\,L^{-1}$	5 $mg_C\,L^{-1}$	10 $mg_C\,L^{-1}$	**Reference**
$^3Q^* + Q$	6.50×10^9	8.32×10^3	2.08×10^4	4.16×10^4	Gan et al., 2008; von Sonntagg et al., 2004; Gorner, 2003
$^3Q^* + PheOH$	5.00×10^9	2.84×10^4	7.10×10^4	1.42×10^5	Assuming near diffusion-controlled
$^3Q^* + H_2O$	1.60×10^4	8.80×10^5	8.80×10^5	8.80×10^5	Gan et al., 2008
$^3Q^* + O_2$	2.00×10^9	5.16×10^5	5.16×10^5	5.16×10^5	Zepp et al., 1985, von Sonntag et al., 2004, McNeill & Canonica, 2016
k_d		5.00×10^4	5.00×10^4	5.00×10^4	Sharpless, McNeill & Canonica, 2016

[a]EAC = electron-accepting capacity
[b]EDC = electron-donating capacity

Appendix B. Supplemental Information for Chapter 4: Photochemical Degradation of Saxitoxins in Surface Waters

Table B.1 The chemicals used in this research.

Chemical	**Producer**	**CAS**
Sodium phosphate dibasic dihydrate (98%)	Fisher Chemical	10028-24-7
Sodium phosphate monobasic dihydrate (99%)	Fisher Chemical	13472-35-0
Ammonium formate (99%)	Acros Organics	540-69-2
Sodium hydroxide (98.9%)	Fisher Chemical	1310-73-2
Glacial acetic acid (99.7%, ACS grade)	VWR	64-19-7
Furfuryl alchohol (98%)	TCI America	98-00-0
Isopropyl alcohol (70%)	VWR	7731-18-5
Tert-butyl alcohol	Alfa Aesar	75-65-0
Rose bengal (95%)	MP Biomedicals	632-69-9
Hydrogen peroxide (30%)	Supelco	7722-84-1
Saxitoxin calibration solution	NRCC	35554-08-6
GTX2/3 calibration solution	NRCC	60508-89-6 & 60537-65-7
C1/2 calibration solution	NRCC	80173-30-4 & 80226-62-6
2-acetonaphthone	Acros Organics	93-08-3
4-chlorobenzoic acid	Aldrich	74-11-3
Benzoic acid	Alfa Aesar	65-85-0
Phosphoric acid	Fisher Chemical	7664-38-2
p-nitroanisole	Aldrich	100-17-4
Pyridine	Mallinckrodt	110-86-1

Table B.2 The elemental compositions and stable isotopic ratios of the DOM isolates, Suwanee River fulvic acid (SRFA) and Nordic Lake fulvic acid (NLFA) (International Humic Substances Society).

Fulvic Acid	H_2O	Ash	C	H	O	N	S	P	$\delta^{13}C$	$\delta^{15}N$
SRFA (1S101F)	8.8	0.46	52.44	4.31	42.20	0.72	0.44	<0.01	-27.6	-1.85
NLFA (1R105F)	9.2	0.45	52.31	3.98	45.12	0.68	0.46	<0.01	-27.8	-3.19

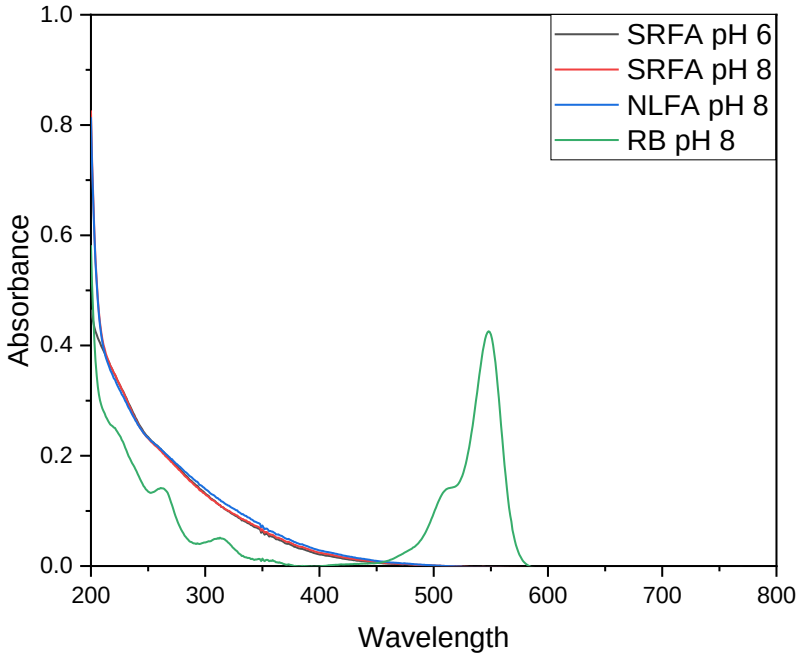

Figure B.1 The UV-visible spectra (1 cm pathlength) of the DOM isolates, Suwanee River and Nordic Lake fulvic acid (SRFA and NLFA; 5 mg_C/L) and rose bengal (RB, 5 µM). All solutions were in 10 mM sodium phosphate buffer at pH 6 or 8.

Table B.3 The HPLC analytical methods used. The injection volume was 50 µL and flowrate was 1.0 mL/min unless otherwise noted.

Compound	Eluent	Retention Time (min)	Detection Wavelength (UV) or Excitation/Detection Wavelength (Fluorescence) (nm)	Limit of Detection (nM)[3]	Limit of Quantitation (nM)[3,4]
STX	97.5% 0.1M ammonium formate 2.5% acetonitrile	3.5	340/390	1.3	3.9
GTX2/3	97.5% 0.1M ammonium formate 2.5% acetonitrile	3.7	340/390	17	52
C1/2	97.5% 0.1M ammonium formate 2.5% acetonitrile	2.7	340/390	26	78
Furfuryl alcohol[1]	68% 10 mM phosphoric acid 32% methanol	3.0	219	75	250
PNA[2]	50% 10 mM phosphoric acid 50% acetonitrile	3.2	300	66	200
p-chlorobenzoic acid	45% 10 mM phosphoric acid 55% methanol	7.6	234	65	199
Salicylic acid	70% 10 mM phosphoric acid 30% acetonitrile	6.0	300/410	34	104

[1] 70 µL injection volume

[2] 80 µL injection volume and 1.5 mL/min flow rate

[3] Determined using the standard deviation of the response and the slope method

[4] All calculations were made with data points collected above the limit of quantitation

Text B.1 LCMS method.

For LCMS analysis at the Central Analytical Mass Spectrometry Facility of the University of Colorado (Boulder, CO), a Waters Synapt G2 high-definition mass spectrometer was used in combination with a Waters Acquity nano-UPLC. The mobile phases were A: water with 0.1% formic acid, and B: acetonitrile with 0.1% formic acid. A 6-minute isocratic method of 90% mobile phase A yielded a consistent retention time of 2.25 min for STX.

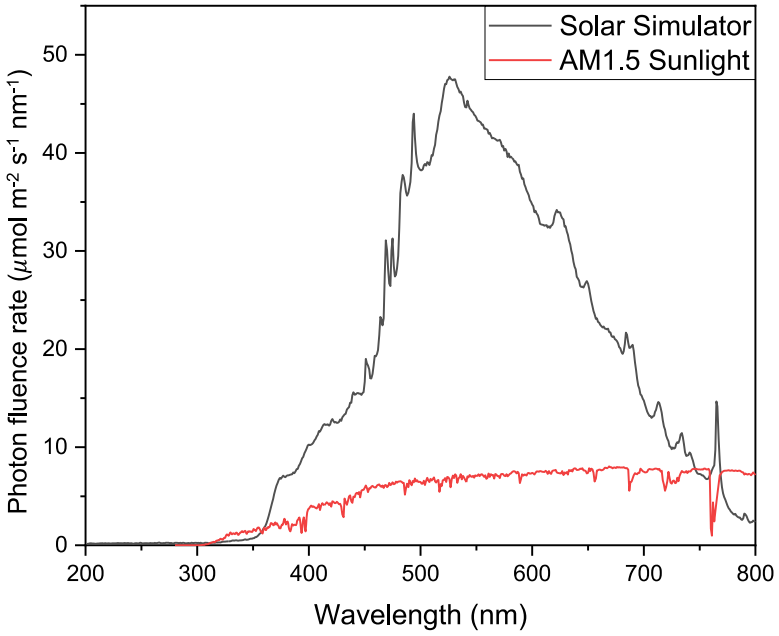

Figure B.2 The photon fluence rate of the solar simulator, measured with an Ocean Optics USB2000 spectrometer, compared with air mass (AM) 1.5 sunlight.

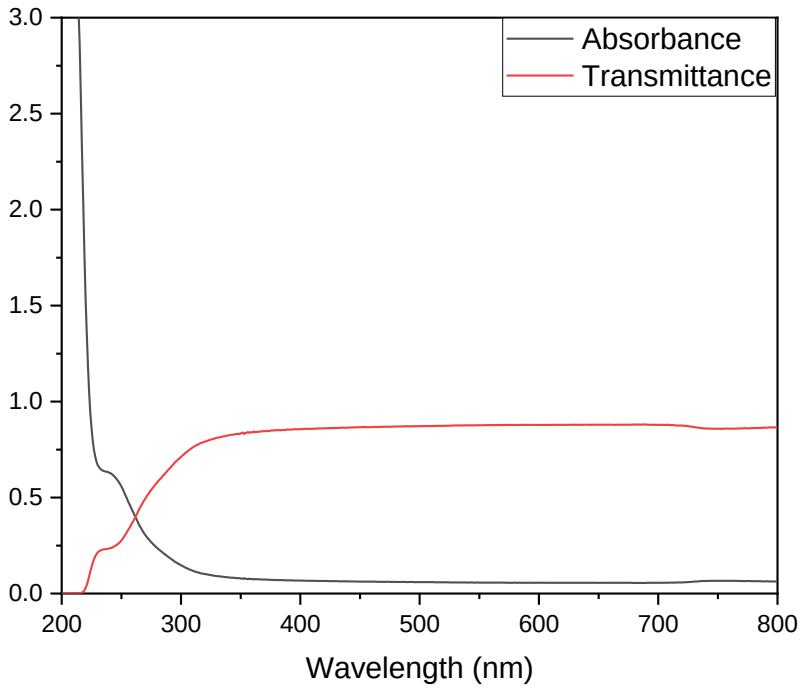

Figure B.3 The absorbance and transmittance of the plastic cuvettes used in irradiation experiments. Note that the measured absorbance in the visible range is > 0 due to reflection of light by the surface of the cuvette which was not corrected in the measurements.

Text B.2 HPLC derivatization method for the detection of saxitoxins

Existing HPLC methods for detecting saxitoxins typically employ a reversed phase column with mobile phases commonly employing a gradient method with ammonium formate and acetonitrile (Lawrence and Niedzwiadek, 2001), or isocratic methods using tetrabutylammonium phosphate, or heptanesulphonate hydrochloride and diammonium orthophosphate and a more complex HPLC (Rositano et al, 1998). Since the toxins themselves do not absorb or fluoresce light, pre- or post-column derivatization needs to be utilized if UV-vis absorbance detector or fluorescence detector is used. A reaction between the toxins and hydrogen peroxide at high pH creates fluorescent transformation products (Bates and Rapaport, 1975; Bates et al., 1978). These products are shown in Figure B.4. For this research, isocratic methods were used, with the mobile phases and detection methods described in Table B.3.

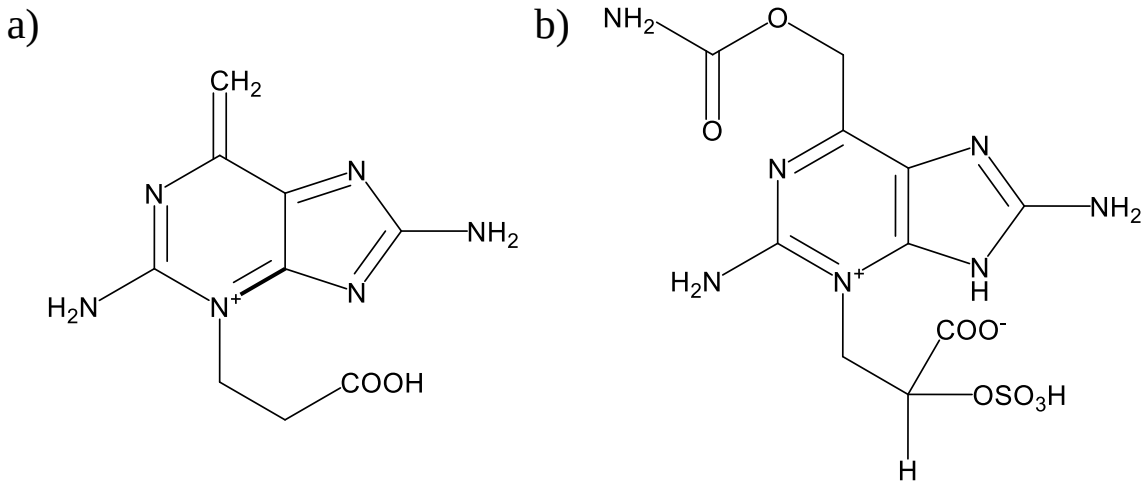

Figure B.4 The oxidation products of a) STX and b) GTX2/3 and C1/2 (Quilliam et al., 1993).

Text B.3 The PNA/pyridine actinometry method.

The photon fluence rate, E_p^0 (units of mol m^{-2} s^{-1}), for the solar simulator used in these experiments was calculated referencing equations provided by Laszakovits et al. (2017) using the PNA/pyridine actinometry described by Equations B.1 and B.2.

$$E_p^0(290-400\ nm) = \frac{k_{PNA}}{(2.303)(\Phi_{PNA}\Sigma_{\lambda=290\ nm}^{400\ nm})(f_{p,\lambda})(\varepsilon_{PNA,\lambda})} \quad \text{B.3}$$

$$\Phi_{PNA} = 0.29[Pyr] + 0.00029 \quad \text{B.4}$$

Where k_{PNA} is the measured PNA phototransformation rate constant (units of s^{-1}), Φ_{PNA} is the quantum yield for PNA phototransformation (unitless, calculated using Equation B.2), $f_{p,\lambda}$ is the normalized emission spectrum of the lamp in the 290-400 nm range (unitless), and $\varepsilon_{PNA,\lambda}$ is the molar absorption coefficient at wavelength λ (units of m^2 mol^{-1}).

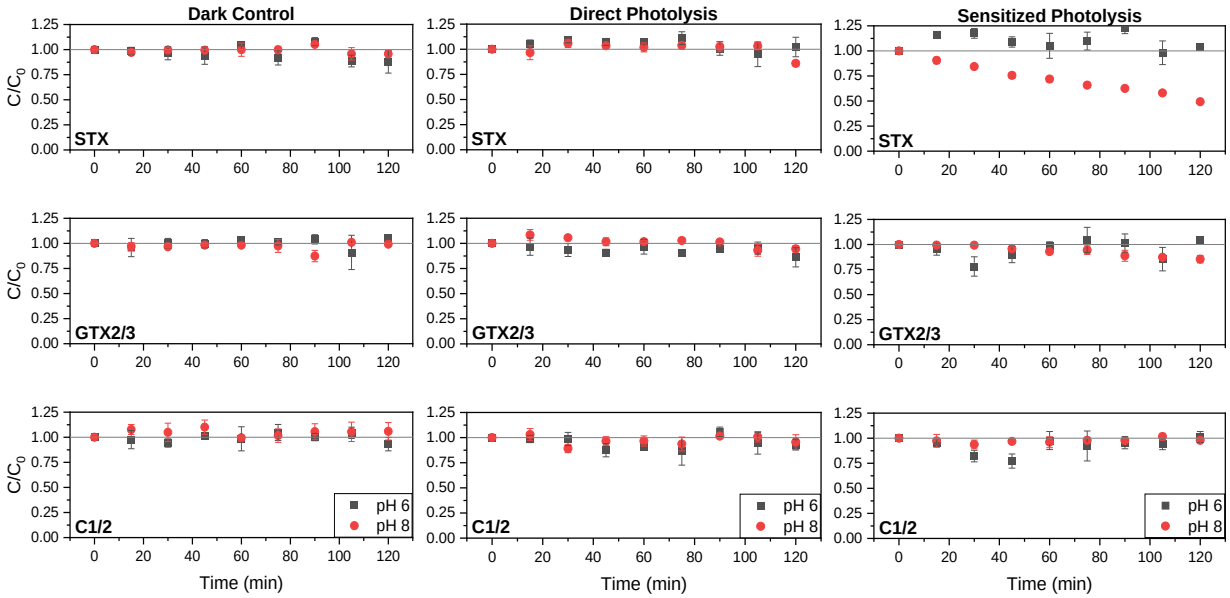

Figure B.5 Plots displaying the change in concentration of toxin vs time in foil wrapped dark control, direct photolysis, and sensitized photolysis experiments. Solutions contained either 200 nM STX or 300 nM GTX 2/3 or 300 nM C 1/2, 10 mM phosphate buffer, and DI water. Sensitized photolysis experiments included $5 mg_C L^{-1}$ Suwanee River Fulvic Acid. Black squares are pH 6 and red circles are pH 8. Points are the average of replicate experiments, with error bars representing standard error (n=3). P-values for the control experiments ranged from 0.220-0.976.

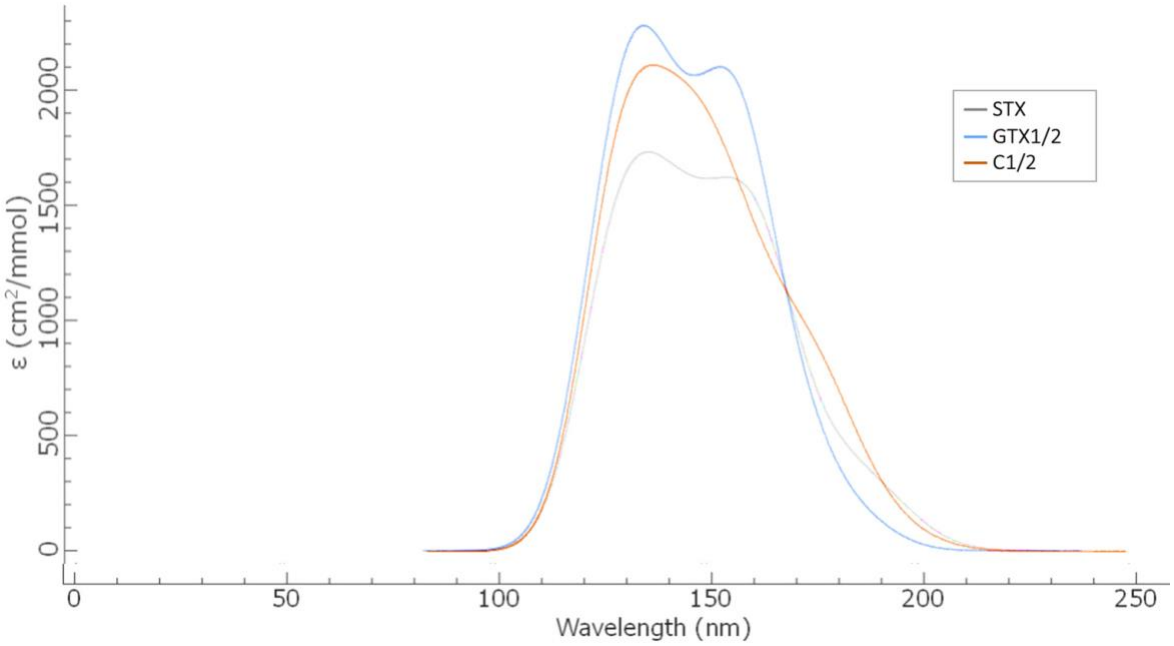

Figure B.6 Predicted UV-vis absorption spectra for STX, GTX1/2, and C1/2. Calculations were made with Avogadro software (basis set: B3L, Gaussian width: 20).

Table B.4 The sensitized photolysis reaction rate constants and associated p-values for STX and GTX2/3 in the presence of a DOM isolate and ·OH quencher. Experimental solutions contained either 200 nM STX or 300 nM GTX2/3, 10 mM phosphate buffer, 5 mg_C/L Suwanee River or Nordic Lake fulvic acid (SRFA or NLFA), 10 mM isopropanol (IPA) or 10mM *t*-butanol (TBA), and DI water. 95% confidence levels are indicated in parentheses. The two-sample t-test values were calculated in comparison to the rate constants without a quencher added, with the tailed t-critical value = 3.182 (α = 0.05, n = 3).

Toxin	·OH quencher	DOM Isolate	k_{STX}^{obs} ($\times 10^{-3}$ min^{-1})	p-value	Two-sample t-test value
STX (HPLC)	IPA	SRFA	4.88 (±1.16)	<0.0001	3.754
	TBA	SRFA	7.23 (±1.28)	<0.0001	0.583
	IPA	NLFA	9.51 (±1.26)	<0.0001	0.609
STX (LCMS)	IPA	NLFA	6.90 (±0.46)	<0.0001	0.148
GTX2/3	IPA	SRFA	4.64 (±0.66)	<0.0001	7.174
	TBA	SRFA	3.83 (±0.90)	<0.0001	2.243
	IPA	NLFA	2.23 (±0.56)	<0.0001	1.631

Text B.4 Measuring the rate constant between saxitoxins and hydroxyl radicals

The second-order rate constant between STX or GTX 2/3 and hydroxyl radicals ($k_{STX}^{\bullet OH}$) was found with a method derived from Lian et al. (2017). The rate of degradation of *p*-chlorobenzoic acid (pCBA) was determined simultaneously with the rate of degradation of STX or GTX 2/3 during irradiation at 254 nm in a Rayonet merry-go-round photoreactor. The photon fluence rate of the Rayonet reactor during the experiment was determined to be 4.92×10^{-4} mol cm^{-2} s^{-1} using a uridine actinometry method described elsewhere (Couch et al., 2021). The initial concentrations were as follows: 5 μM pCBA, 5 μM STX or GTX 2/3, 5 ppm H_2O_2 (concentration verified using absorbance at 240 nm), and 1 mM phosphate buffer at pH 7. Controls with no pCBA showed no direct photolysis of STX or GTX 2/3 at 254 nm. pCBA, STX, and GTX 2/3 were quantified using HPLC-UV, FLD. $k_{STX}^{\bullet OH}$ was calculated according to Equation B.3 by plotting $ln\frac{STX}{STX_0}$ versus $ln\frac{pCBA}{pCBA_0}$ (shown below) and multiplying the slope by the second order rate constant between $^{\bullet}$OH and pCBA (5.0×10^{9}; Neta & Dorfman, 1968). The p-values on each of the slopes were <0.001 (n=3). Error bars represent the standard deviation on $ln\frac{STX}{STX_0}$ and $ln\frac{pCBA}{pCBA_0}$ in the y and x directions, respectively.

$$ln\frac{STX}{STX_0} = \frac{k_{STX}^{\bullet OH}}{k_{pCBA}^{\bullet OH}} ln\frac{pCBA}{pCBA_0} \qquad \text{B3}$$

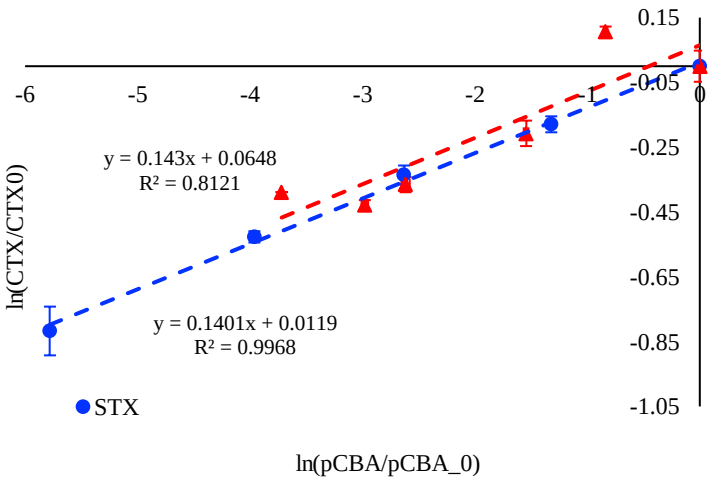

Text B.5 Measuring the rate constant between DOM and hydroxyl radicals

The second-order rate constant for the reaction between DOM and •OH ($k_{DOM}^{\bullet OH}$) have previously been determined for several DOM isolates:

DOM Isolate	**Authors**	$k_{DOM}^{\bullet OH}$ **($M_C^{-1}s^{-1}$)**
Suwanee River Fulvic acid (SRFA) I	Westerhoff et al., 2007	1.60×10^8
SRFA I	McKay et al., 2011	2.06×10^8
Pony Lake Fulvic Acid (PLFA)	McKay et al., 2011	6.90×10^8

For this research, McKay's value of $k_{DOM}^{\bullet OH}$ for SRFA I was used. $k_{DOM}^{\bullet OH}$ for Nordic Lake fulvic acid (NLFA) was determined using a method derived from Lian et al. (2017). The rate of transformation of the •OH probe, *p*-chlorobenzoic acid (pCBA, $[pCBA]_0 = 10\ \mu M$), was quantified in the presence of 0, 1, 2, 5, and 10 mg_C/L NLFA and 10 ppm H_2O_2 (concentration verified using absorbance at 240 nm). The ratio of the pseudo first-order rate constant of pCBA transformation without DOM present to the pseudo first-order rate constants of pCBA transformation in the presence of DOM ($\frac{k'_{pCBA}}{k'^{DOM}_{pCBA}}$) was plotted versus the concentration of DOM according to Equation B.4.

$$\frac{k'_{pCBA}}{k'^{DOM}_{pCBA}} = 1 + \frac{k_{DOM}^{\bullet OH}[DOM]}{k_{pCBA}^{\bullet OH}[pCBA] + k_{H_2O_2}^{\bullet OH}[H_2O_2]} \qquad \text{B.4}$$

Where $k_{pCBA}^{\bullet OH}$ is the second-order rate constant between pCBA and •OH ($5.00 \times 10^9\ M^{-1}s^{-1}$; Neta and Dorfman, 1968) and $k_{H_2O_2}^{\bullet OH}$ is the second-order rate constant between •OH and H_2O_2 ($2.70 \times 10^7\ M^{-1}s^{-1}$; Buxton et al, 1988). The corresponding data yielded a linear curve with a slope of 4704.7 $mg_C^{-1}L$, and plugging the known values into Equation B.3, $k_{NLFA}^{\bullet OH}$ was determined to be $2.98\times10^8\ M_C^{-1}s^{-1}$ ($\pm\ 1.03\times10^8$ 95% confidence interval).

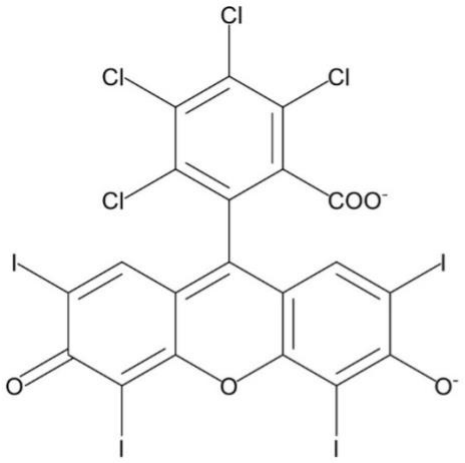

Figure B.7 Structure of rose bengal at pH 8; pK_{a1} = 1.89, pK_{a2} = 3.93 (Batistela et al, 2011).

Text B.6 The method to account for rose bengal (RB) photodegradation.

Since RB underwent photodegradation itself when exposed to simulated sunlight irradiation, a transformed time (Equation S5) was calculated to account for the transformation of RB.

$$[RB] = [RB]_0 e^{-\alpha t} \quad \text{B.5}$$

Transformation of a compound C photosensitized by RB can be described using second-order kinetics as in Equation S6:

$$-\frac{d[C]}{dt} = k_C^{sens}[RB][C] \quad \text{B.6}$$

Since $k_C^{sens}[RB]$ varies with time because of RB's photodegradation, Equation S4 is substituted into Equation S7:

$$-\frac{d[C]}{dt} = k_C^{sens}[RB]_0 e^{-\alpha t}[C] \quad \text{B.7}$$

Equation S6 can be rearranged and integrated to obtain Equation S8:

$$ln\frac{[TC]_t}{[TC]_0} = -k_C^{sens}[RB]_0 \frac{1-e^{-\alpha t}}{\alpha} \quad \text{B.8}$$

Where the latter portion of Equation S8 can be considered the transformed time (Equation S9).

$$t' = \frac{1-e^{-\alpha t}}{\alpha} \quad \text{B.9}$$

Plotting $\ln\frac{[TC]_t}{[TC]_0}$ vs t', one can acquire $k_C^{sens}[RB]_0$ as a fitting parameter in a linear regression.

Table B.5 The pseudo-first-order transformation rate constant of fufuryl alcohol (FFA; 10 μM) and $^1O_2$, and $^1O_2$ steady state concentration, in the presence of 5 μM rose Bengal (RB), 5 $mg_C L^{-1}$ Suwanee River fulvic acid (SRFA), and 5 $mg_C L^{-1}$ Nordic Lake fulvic acid (NLFA). All solutions were at pH 8.

Sample	$k'_{FFA}^{^1O_2}$ **(s^{-1})**	**$[^1O_2]_{ss}$ (M)**
RB	3.44E-02	3.44E-10
SRFA	3.58E-05	3.58E-13
NLFA	3.35E-05	3.35E-13
2-AN	1.30E-04	1.30E-12

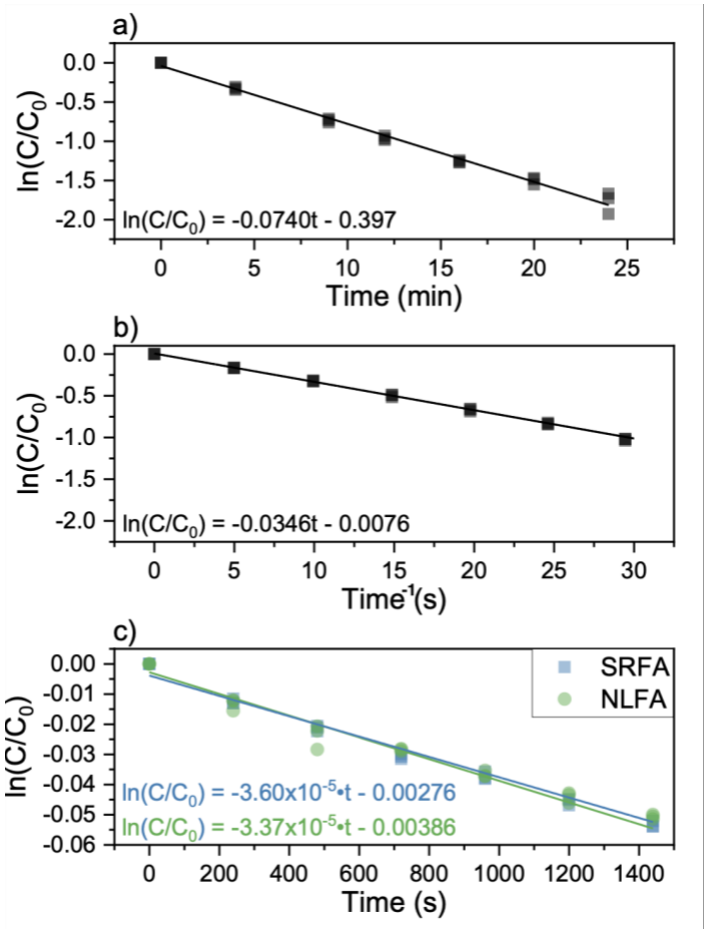

Figure B.8 Plots showcasing a) rose bengal (RB) direct photodegradation vs time b) furfuryl alcohol (FFA) loss in the presence of RB and c) FFA loss in the presence of DOM isolates. a) shows $\ln([RB]/[RB]_0)$ by measuring RB absorbance at 546 nm, with an initial [RB] of 5 μM. b) and c) show $\ln([FFA]/[FFA]_0)$ as measured on HPLC with initial concentrations of 10 μM FFA, 5 μM RB, and 5mg$_C$L^{-1} DOM.

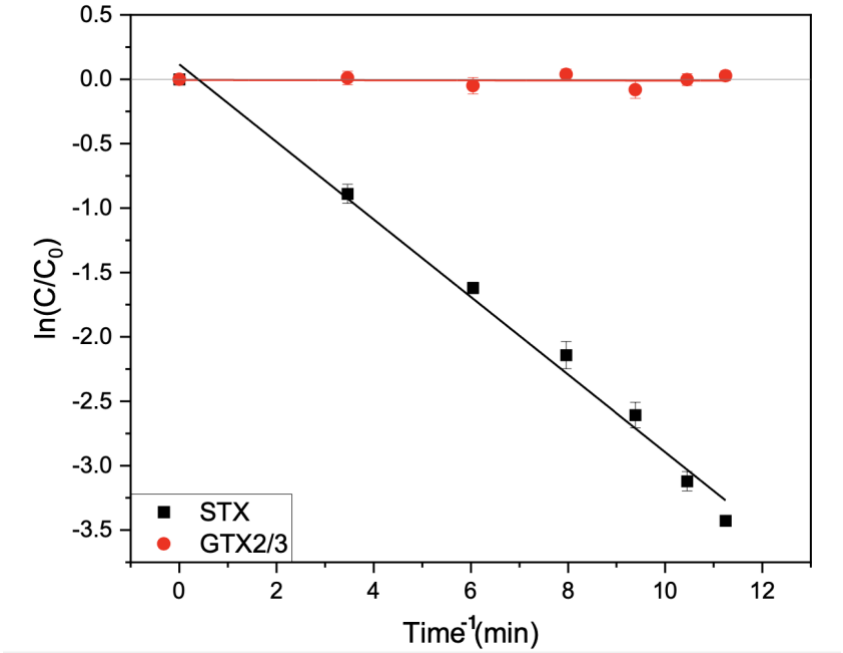

Figure B.9 Plot displaying the change in concentration of cyanotoxin vs time for sensitized photolysis experiments at pH 8 in the presence of rose bengal (RB). Solutions contained either 200 nM STX (black squares) or 300 nM GTX 2/3 (red circles), 10 mM phosphate buffer, 5 μM RB, and DI water. Points are the average of replicate experiments, with error bars representing standard error (n=3).

Text B.7 Determination of $^1O_2$ production by 2-acetonapthone

To assess the impact of $^1O_2$ on the degradation of STX in the presence of 2-AN, the steady-state concentration of $^1O_2$ was determined by measuring the degradation of 10 µM FFA under the experimental conditions (solar simulator irradiation, 50 µM 2-AN, 10 mM phosphate buffer pH 8). The first-order rate constant for FFA degradation was found to be 1.30×10^{-4} s^{-1} (Table B.5). Dividing this by the second-order rate constant between $^1O_2$ and FFA (1.00×10^{8} M^{-1} s^{-1}) yielded a $[^1O_2]_{ss}^{(2\text{-}AN)}$ of 1.30×10^{-12} M (Table B.6). Next, $[^1O_2]_{ss}^{(2\text{-}AN)}$ was multiplied by the second-order rate constant between $^1O_2$ and STX (1.27×10^{7} M^{-1} s^{-1}) and divided by the overall first-order rate constant between 2-AN and STX to find the fraction of STX reacting with $^1O_2$ ($f_{^1O_2,2-AN}$), assuming $^1O_2$ and ^{3}2-AN* are the only reactive species present (Equation B.10 & B.11). $f_{^1O_2,2-AN}$ was found to be 14.8% for STX, and 0% for GTX 2/3 since $^1O_2$ did not contribute to GTX 2/3's degradation. This implies that the contribution of ^{3}2-AN* was 85.2% and 100% for STX and GTX 2/3, respectively.

$$f_{^1O_2,2-AN} = \frac{k_{STX}^{^1O_2}[^1O_2]_{ss}^{(2-AN)}}{k_{STX}^{2-AN}} = \frac{k'^{^1O_2}_{STX}}{k_{STX}^{2-AN}} \quad \text{B.10}$$

$$k_{STX}^{2-AN} = k'^{^3 2-AN^*}_{STX} + k'^{^1O_2}_{STX} \quad \text{B.11}$$

Table B.6 The sensitized photolysis reaction rate constants and associated p-values for saxitoxin (STX) and gonyautoxin 2 and 3 (GTX 2/3) in the presence of 2-acetonaphthone (2-AN). Experimental solutions contained either 200 nM STX or 300 nM GTX2/3, 10 mM phosphate buffer (pH 8), and 50 µM 2-AN. 95% confidence levels are indicated in parentheses.

Toxin	k'^{2AN}_{STX} **($\times 10^{-3}$ min^{-1})**	**Half-life (min)**	**p-value**
STX	3.44 (±0.85)	202 (±50)	<0.0001
GTX 2/3	1.45 (±0.62)	479 (±204)	0.00082

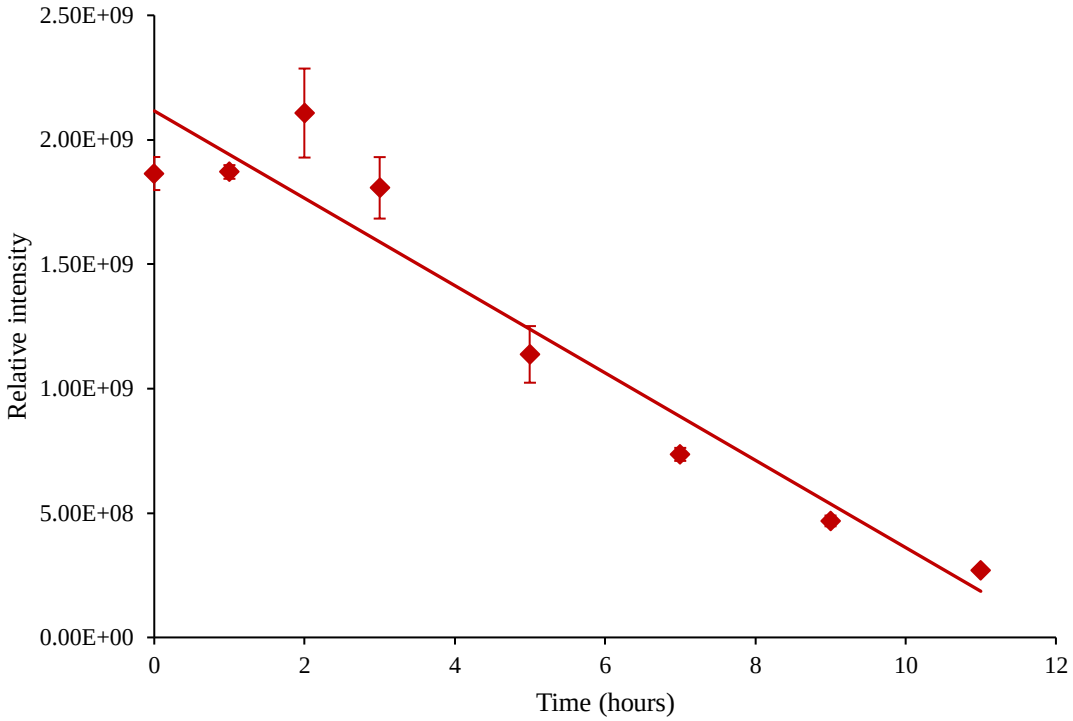

Figure B.10 Degradation of 2-acetonaphthone during the irradiation of STX detected by HRMS. Solutions contained 1µM STX, 50 µM 2-AN, and 10 mM ammonium formate (pH 8.3). Points are the average of repeated experiments, and error bars represent the standard error (n=3).

Table B.7 Rate constants for the reaction between STX or GTX and DOM in the presence of phenol. Solutions contained either 200 nM STX or 300 nM GTX2/3, 10 mM phosphate buffer, 5 mg_C/L SRFA or NLFA, and 100 µM phenol. Two-sample t-test values were calculated for comparison to the rate constants without phenol, with the tailed t-critical value = 3.182 ($\alpha = 0.05$, $n = 3$).

Toxin	**DOM Isolate**	k_{STX}^{obs} **(×10^{-3} min^{-1})**	**p-value**	**Two-sample t-test value**
STX	SRFA	6.06 (±0.33)	<0.0001	0.812
	NLFA	8.94 (±1.30)	<0.0001	0.357
GTX2/3	SRFA	1.42 (±0.59)	<0.0001	0.319
	NLFA	3.75 (±1.27)	<0.0001	0.168

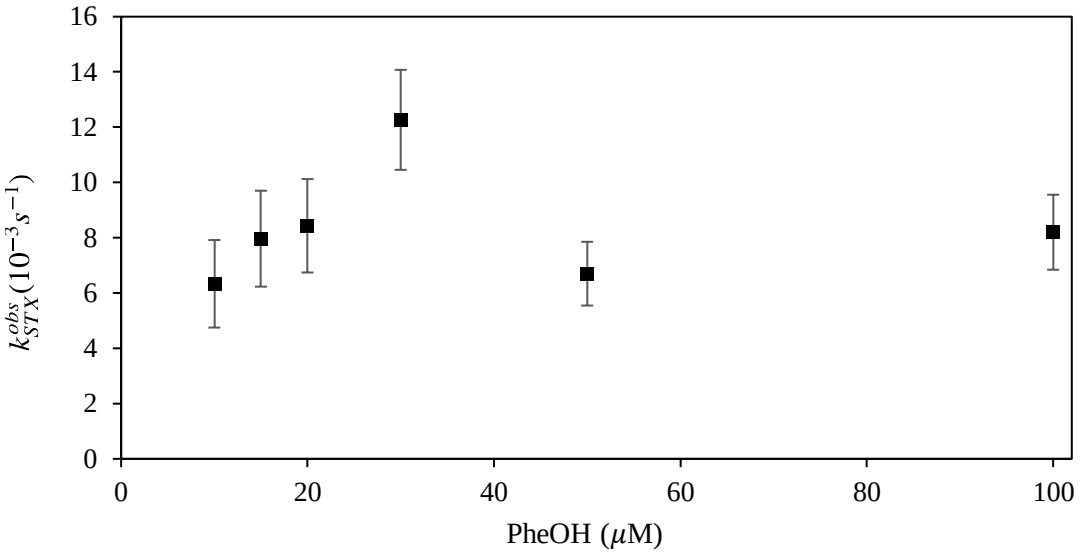

Figure B.11 Observed reaction rate constants for the reaction between STX and Nordic Lake fulvic acid (NLFA) in the presence of various concentrations of phenol. Solutions contained 200 nM STX, 10 mM phosphate buffer (pH 8), 5 mg_C/L NLFA, and phenol. Points are the average of repeated experiments, and error bars represent the standard error (n=3).

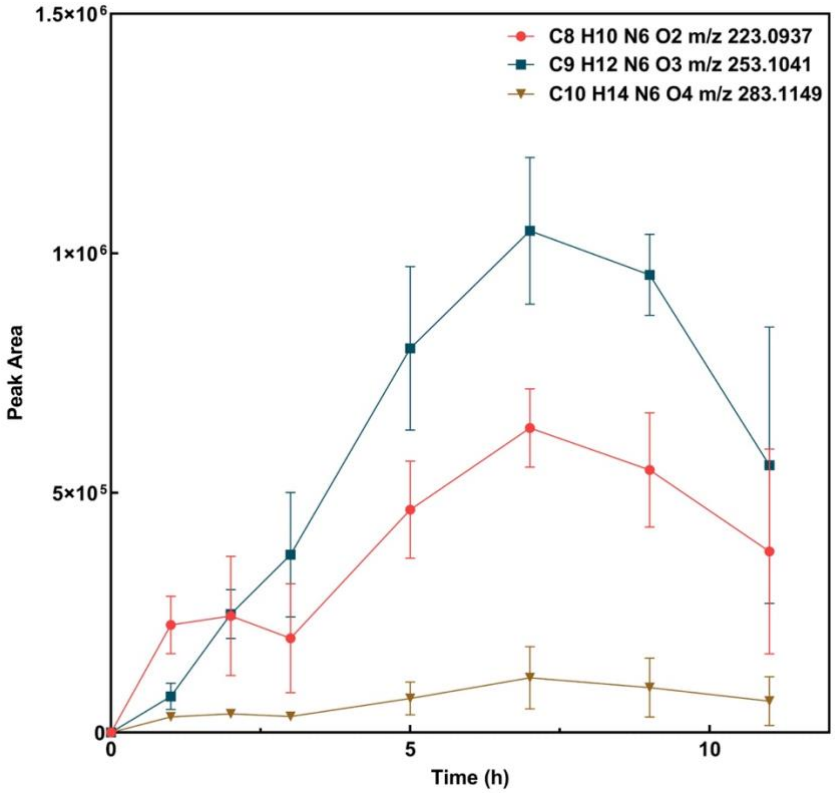

Figure B.12 HRMS detection of transformation product (TP) candidates during the sensitized photolysis of STX. Solutions contained 1 µM of STX, 50 µM 2-acetonaphthone, and 10 mM ammonium formate (pH 8.3). Error bars represent the standard deviation of the peak areas of TPs measured in duplicate samples.

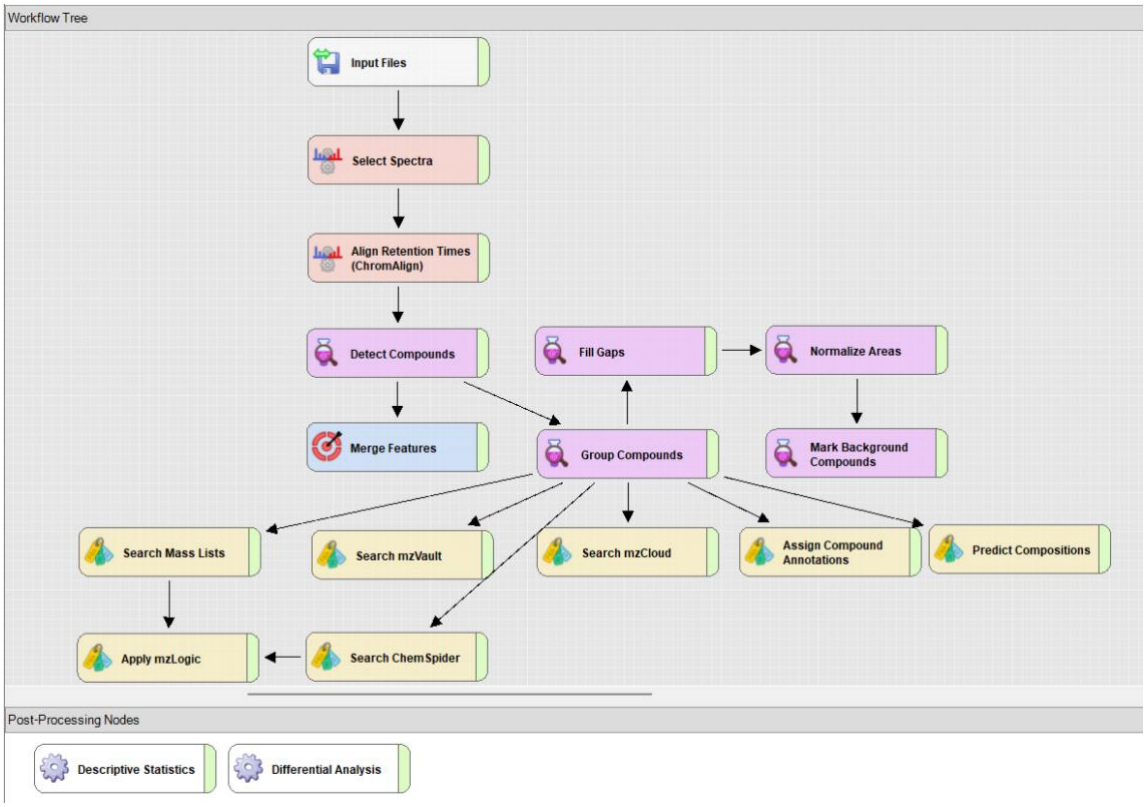

Figure B.13 Screenshot of *Compound Discoverer 3.3* transformation product screening workflow. The nodes represent the process steps in the workflow tree. The arrows represent the direction of connections between nodes.

Table B.8 Overall charges and protonation states (α_1, α_2, and α_3) of STX, GTX 2/3, and C 1/2. Figure 1 of main text shows the functional group and pK_a associated with each protonation state.

	Toxin	**STX**	**GTX 2/3**	**C 1/2**
pH 8	**charge**	+1	0	-1
	α_1	0.493	0.518	0.185
	α_2	0.036	0.071	0.806
	α_3	-	-	0.153
pH 6	**charge**	+2	+1	+1
	α_1	0.010	0.012	0.168
	α_2	0.000	0.000	0.007
	α_3	-	-	0.000

Table B.9 The average water quality parameters and photodegradation kinetics data input to the APEX code. Unknown or zero-value parameters were input as 0. The rate constant and fraction of STX reacting with $^3DOM^*$ are averages of Suwanee River and Nordic Lake fulvic acid.

Species	Concentration (M)	RI	2nd- order rate constant between RI and STX ($M^{-1}s^{-1}$)	Quantum yield of RI produced by DOM (%)[b]
NO_3^-	1×10^{-4}	$^{\bullet}OH$	6.87×10^8	-
NO_2^-	1×10^{-6}	$^1O_2$	1.27×10^7	22.97
CO_3^{2-}	1×10^{-5}	$^3DOM^*$	1.89×10^{8} [a]	76.64
HCO_3^-	1×10^{-3}			
Br^-	1×10^{-8}			

[a]The second-order rate constant between STX and $^3DOM^*$ was determined by diving the pseudo-first order rate constant ($k'^{^3DOM^*}_{STX} = k^{obs}_{STX} - k'^{^1O_2}_{STX} - k'^{^{\bullet}OH}_{STX}$) by the average $[^3DOM^*]_{ss}$ in the presence of SRFA and NLFA. $[^3DOM^*]_{ss}$ was estimated using the assumption,
$[^1O_2]_{ss}/[^3DOM^*]_{ss} \sim 2f$, where f is the fraction of O_2-dependent quenching that produces $^1O_2$ and is ~ 0.3 (Schmitt et al., 2017)

[b]The quantum yields of $^1O_2$ and $^3DOM^*$ generated by DOM were adjusted by a factor of difference between the APEX-estimated and experimental steady-state concentrations of $^1O_2$ and $^3DOM^*$ so the APEX model would match the experimental STX half-lives (Vione et al., 2018).

Appendix C. Supplemental Information for Chapter 5: Enhanced Removal of Saxitoxins by Far-UVC Advanced Oxidation Processes

Table C.1 Reagents used in this research.

Chemical	Producer	CAS
Sodium phosphate dibasic dihydrate (98%)	Fisher Chemical	10028-24-7
Sodium phosphate monobasic dihydrate (99%)	Fisher Chemical	13472-35-0
Ammonium formate (99%)	Acros Organics	540-69-2
Sodium hydroxide (98.9%)	Fisher Chemical	1310-73-2
Glacial acetic acid (99.7%, ACS grade)	VWR	64-19-7
Hydrogen peroxide (30%)	Supelco	7722-84-1
Saxitoxin calibr[4,9,11,44,45,58,69]ation solution	NRCC	35554-08-6
GTX2/3 calibration solution	NRCC	60508-89-6 & 60537-65-7
C1/2 calibration solution	NRCC	80173-30-4 & 80226-62-6
4-chlorobenzoic acid	Aldrich	74-11-3
Phosphoric acid	Fisher Chemical	7664-38-2
Potassium iodide	Sigma-Aldrich	7681-11-0
Potassium hydrogen phthalate	Sigma-Aldrich	877-24-7
Ammonium molybdate	Sigma-Aldrich	15123-80-5

Table C.2 The elemental compositions and stable isotopic ratios of the dissolved organic matter (DOM) isolates (International Humic Substances Society).

Fulvic Acid	H_2O	Ash	C	H	O	N	S	P	$\delta^{13}C$	$\delta^{15}N$
SRFA[1] (1S101F)	8.8	0.46	52.44	4.31	42.20	0.72	0.44	<0.01	-27.6	-1.85
NLFA[2] (1R105F)	9.2	0.45	52.31	3.98	45.12	0.68	0.46	<0.01	-27.8	-3.19

[1]SRFA = Suwanee River fulvic acid
[2]NLFA = Nordic Lake fulvic acid

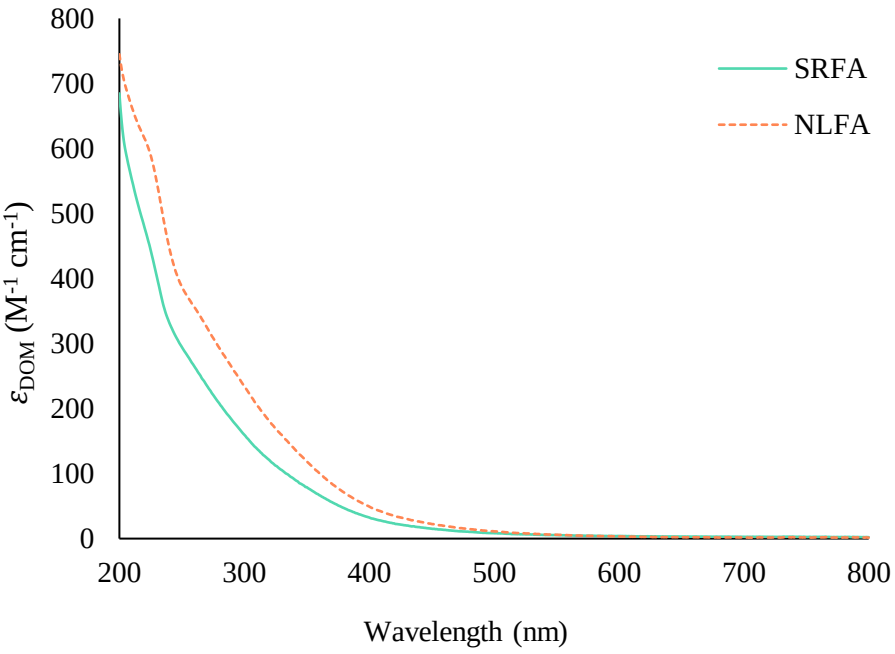

Figure C.1 UV-visible absorbance spectra of 5 mg_C L^{-1} solutions of dissolved organic matter isolates. SRFA = Suwanee River fulvic acid and NLFA = Nordic Lake fulvic acid.

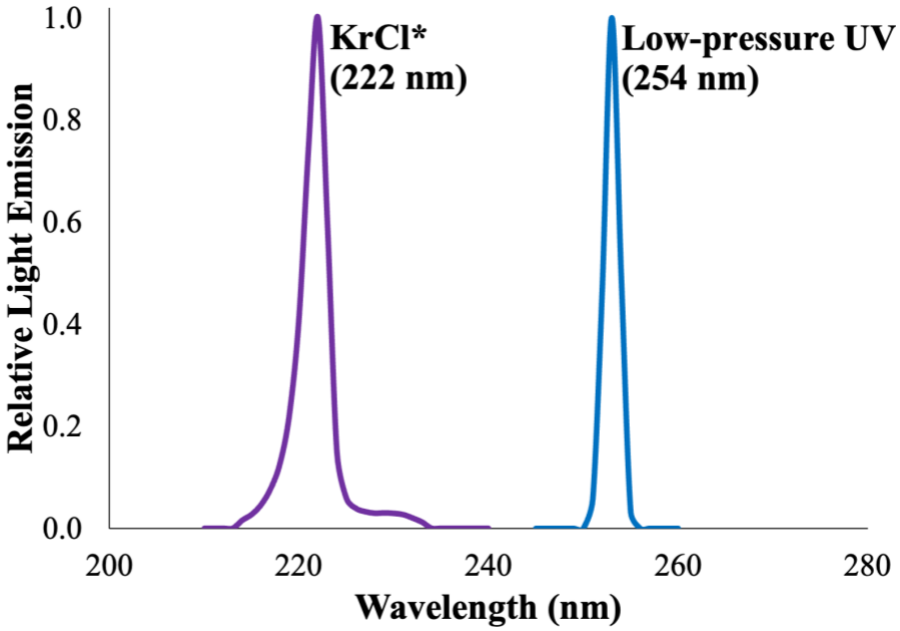

Figure C.2 Emission spectrum of both lamps used in this study, a filtered KrCl* excimer lamp and a low-pressure UV mercury lamp. The emission spectrum was measured by a calibrated Maya 2000 Pro spectrometer (Ocean Insight, Dunedin, FL).

Table C.3 Average irradiance (E_0) and "incident irradiance" (E_{inc}) for each experimental matrix. E_0 was determined based on the sample depth, absorbance, water factor, reflection factor, divergence factor, and Petri factor (Bolton & Linden, 2003). E_{inc} is an adaptation of E_0 which omits the water factor (Payne et al., 2022). Each solution contained 10 mM of pH 7 phosphate buffer and 500 nM of any of the three saxitoxin congeners. E_0 and E_{inc} did not vary between saxitoxin congeners because their absorbance in negligible.

UV source	Experimental matrix	E_0 (mJ cm^{-2} s^{-1})	E_{inc} (mJ cm^{-2} s^{-1})
222 nm KrCl* excimer	5 mg_C L^{-1} SRFA	0.3074	0.3550
	5 mg_C L^{-1} NLFA	0.3306	0.3550
	10 ppm H_2O_2	0.3507	0.3525
	10 ppm H_2O_2 + 1 mg_C L^{-1} SRFA	0.3526	0.3525
	10 ppm H_2O_2 + 1 mg_C L^{-1} NLFA	0.3489	0.3572
	10 ppm H_2O_2 + 5 mg_C L^{-1} SRFA	0.3124	0.3461
	10 ppm H_2O_2 + 5 mg_C L^{-1} NLFA	0.2896	0.3462
254 nm LPUV	5 mg_C L^{-1} SRFA	0.998	1.117
	5 mg_C L^{-1} NLFA	1.062	1.287
	10 ppm H_2O_2	1.125	1.445
	10 ppm H_2O_2 + 1 mg_C L^{-1} SRFA	1.045	0.963
	10 ppm H_2O_2 + 1 mg_C L^{-1} NLFA	1.073	1.007
	10 ppm H_2O_2 + 5 mg_C L^{-1} SRFA	1.030	1.016
	10 ppm H_2O_2 + 5 mg_C L^{-1} NLFA	1.081	1.060

Text C.1 Light screening factor calculations.

Due to the significant absorbance by dissolved organic matter (DOM) and hydrogen peroxide (H_2O_2) in experimental solutions, a light screening factor (S) was applied to adjust the estimated hydroxyl radical steady-state concentrations at the near-surface to the experimental depth of 0.60 cm. The light screening factor was calculated using Equation C.1, where $\sum \varepsilon_{Sens,\lambda}[Sens]$ is the sum of the molar absorption coefficients of each photosensitzer (DOM or H_2O_2) multiplied by their concentrations. S was calculated assuming monochromatic light at 222 nm or 254 nm.

$$S = \frac{1 - e^{-2.303 \sum \varepsilon_{Sens,\lambda}[Sens]}}{2.303 \sum \varepsilon_{Sens,\lambda}[Sens]} \quad \text{(C.1)}$$

Text C.2 Pre-column derivatization method for the detection of saxitoxins

Since saxitoxins do not absorb or fluoresce light, a pre-column derivatization method was used to quantify the toxins using HPLC with fluorescence detection. A reaction between the toxins and hydrogen peroxide at high pH creates fluorescent transformation products (Bates and Rapaport, 1975; Bates et al., 1978). These products are shown in Figure C.3. An isocratic HPLC method was used to quantify the derivatized saxitoxins with fluorescence detection at 340/390 nm (excitation/detection) and a mobile phase consisting of a 10 mM ammonium formate solution with 2.5% acetonitrile that was adjusted to pH 6 with acetic acid (Lawrence and Niedzwiadek, 2001). A standard curve of saxitoxins is shown in Figure C.4.

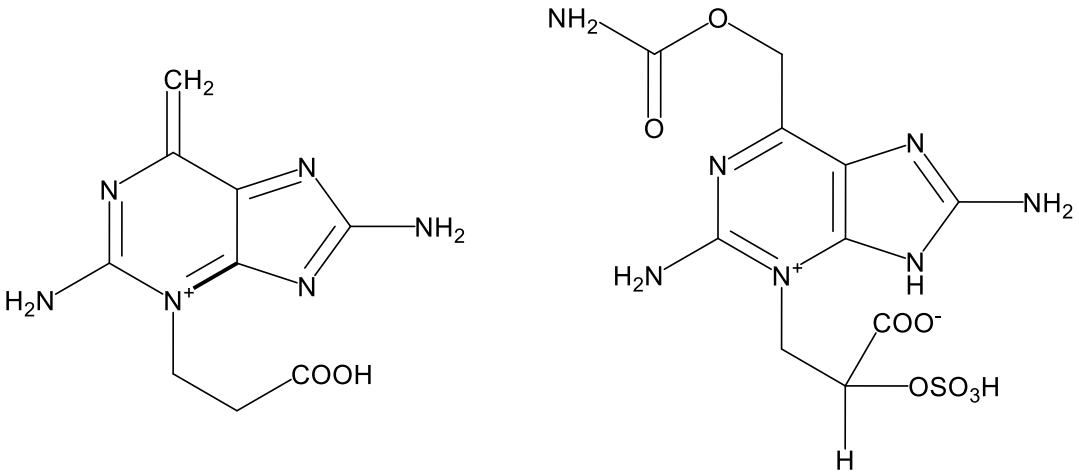

Figure C.3 The oxidation products of a) STX and b) GTX-2/3 and C-1/2 (Quilliam et al., 1993).

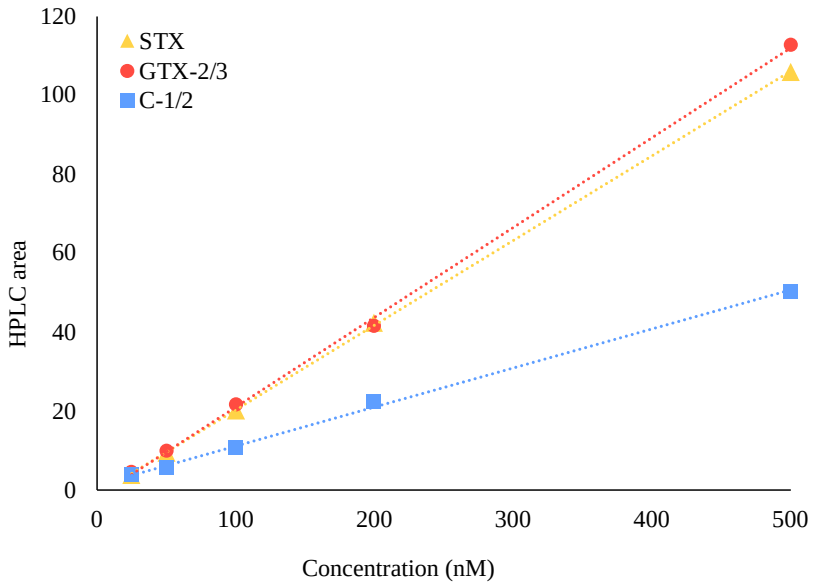

Figure C.4 Standard curve of saxitoxins detected using HPLC and the derivatization method described in Text S2. Blue squares represent STX (saxitoxin), blue squares represent GTX-2/3 (gonyautoxin-2 and -3), and yellow triangles represent C-1/2 (n-sulfocarbamoylgonyautoxin-1 and -2). The limits of detection (LOD) for STX, GTX-2/3, and C-1/2 were 4.3, 13.5, and 19.3 nM, respectively. The limits of quantitation (LOQ) for STX, GTX-2/3, and C-1/2 were 13.1, 40.9, and 58.6 nM, respectively. The LOD and LOQ were determined using the ratio of the standard error to the slope.

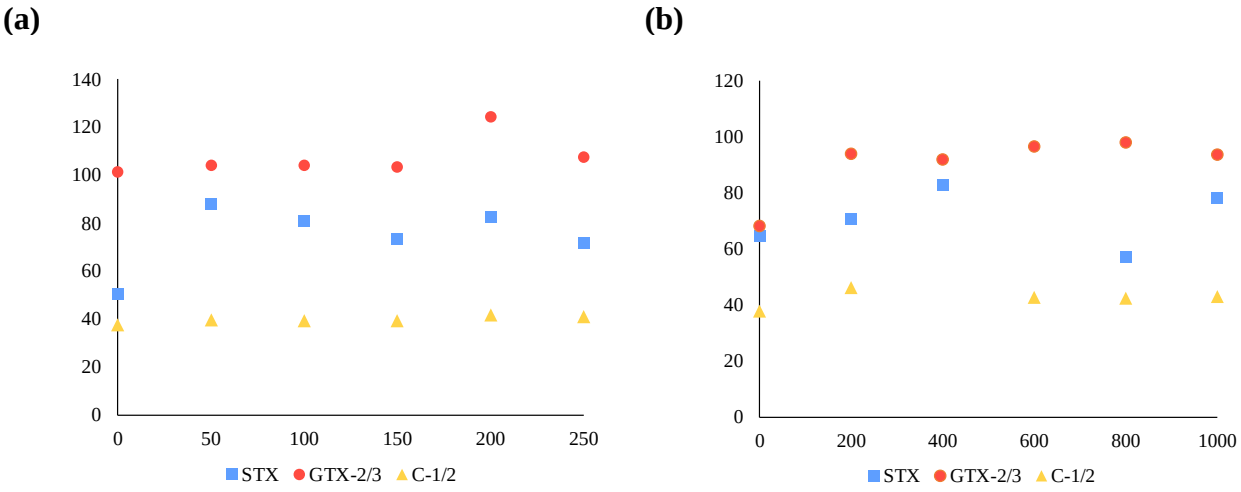

Figure C.5 HPLC area of saxitoxins in the presence of Nordic Lake fulvic acid with exposure to (a) KrCl* excimer and (b) LPUV radiation. STX = saxitoxin, GTX-2/3 = gonyautoxin-2 and -3, C-1/2 = n-sulfocarbamoylgonyautoxin-1 and -2, SRFA = Suwanee River fulvic acid, and NLFA = Nordic Lake fulvic acid.

Text C.3 Determination of $\phi_{DOM,\lambda}$ for SRFA and NLFA at 222 nm and 254 nm.

p-chlorobenzoic acid (pCBA) was applied as an •OH probe to determine the •OH quantum yield ($\phi_{DOM,\lambda}$) for the two DOM isolates, Suwanee River fulvic acid (SRFA), and Nordic Lake fulvic acid (NLFA). 10 μM pCBA was added to solutions containing 5 $mg_C\,L^{-1}$ of either SRFA or NLFA. The rate of •OH formation ($r_{\bullet OH}$) was . $\phi_{DOM,\lambda}$ was calculated according to Equation C.2 (McKay & Rosario, 2018), where $k_{DOM-\alpha}$ is the rate of light absorption by DOM at a specific wavelength. Both lamps were treated as monochromatic at either 222 nm or 254 nm (Figure C. 2). $k_{DOM-\alpha}$ (s^{-1}) was determined at each wavelength for each DOM isolate using Equation C.3, where $E_p^0(\lambda)$ (Es cm^{-2} s^{-1}) is the incident irradiance divided by the UV photon energy (J Es^{-1}), $\varepsilon_{DOM}(\lambda)$ is the molar absorptivity of SRFA or NLFA (Table C.4), and z (cm) is pathlength of each sample in the petri dish.

$$\phi_{DOM,\lambda} = \frac{r_{\bullet OH}}{k_{DOM-\alpha}[DOM]} \tag{C.2}$$

$$k_{DOM-\alpha} = \frac{E_p^0(\lambda)\varepsilon_{DOM}(\lambda)(1 - 10^{-\varepsilon_{DOM}(\lambda)[DOM]z})}{\varepsilon_{DOM}(\lambda)[DOM]z} \tag{C.3}$$

Table C.4 Rates of •OH formation ($r_{•OH}$), quantum yields of •OH formation ($\phi_{DOM,\lambda}$ or $\phi_{H_2O_2,\lambda}$), and molar absorptivities of H_2O_2 ($\varepsilon_{DOM}(\lambda)$ or $\varepsilon_{H_2O_2,\lambda}$), Suwanee River fulvic acid (SRFA), and Nordic Lake fulvic acid (NLFA) at 222 nm and 254 nm. $r_{•OH}$ was determined using pCBA kinetics. Values for $\phi_{H_2O_2,\lambda}$ and $\varepsilon_{H_2O_2,\lambda}$ were previously determined (Payne et al., 2022). $\phi_{DOM,\lambda}$ for SRFA and NLFA was determined according to Text C.3. $\varepsilon_{DOM,\lambda}$ was determined for SRFA and NLFA in this work based on the absorption spectra of each DOM isolate (Figure C.1).

	222 nm			**254 nm**		
	SRFA	NLFA	H_2O_2	SRFA	NLFA	H_2O_2
$r_{•OH}$(M s^{-1})	6.93×10^{-10}	3.71×10^{-10}	8.81×10^{-9}	5.67×10^{-10}	7.32×10^{-10}	7.51×10^{-9}
$\phi_{DOM,\lambda}$or $\phi_{H_2O_2,\lambda}$ (mol Es^{-1})	2.30×10^{-3}	1.19×10^{-3}	0.45	7.73×10^{-4}	8.90×10^{-4}	0.50
$\varepsilon_{DOM}(\lambda)$or $\varepsilon_{H_2O_2,\lambda}$ (M-1 cm-1)	465.8	606.9	99	282.8	373.7	21

Table C.5 Steady-state concentrations of •OH normalized to incident fluence rate (E_{inc}) in control experiments determined using •OH quantum yields and scavenging constants according to Equations 2 and 3 of the manuscript. $[•OH]_{ss}$ values were calculated using 5 mg_C L^{-1} Suwanee River fulvic acid (SRFA) or 5 mg_C L^{-1} Nordic Lake fulvic acid (NLFA).

$[•OH]_{ss}/E_{inc}$ **(M cm^2 mW^{-1} $\times10^{-15}$)**	**SRFA**	**NLFA**
UV_{222}	53.3 (±2.77)	70.7 (±1.37)
UV_{254}	2.67 (±0.14)	2.31 (±0.05)